The solar-cycle dependence of the heliospheric diffusion tensor

AE Nel

23526769

Dissertation submitted in partial fulfilment of the requirements for the degree *Magister Scientiae* in Space Physics (specialising in Physics) at the Potchefstroom Campus of the North-West University

Supervisor:	Prof RA Burger
Co-supervisor:	Dr NE Engelbrecht

October 2015

NORTH-WEST UNIVERSITY
YUNIBESITI YA BOKONE-BOPHIRIMA
NOORDWES-UNIVERSITEIT

It all starts here ™

The solar-cycle dependence of the heliospheric diffusion tensor

A. E. Nel, B.Sc. (Hons.)

Dissertation submitted in partial fulfillment of the requirements for the degree Master of Science at the Potchefstroom Campus of the North-West University

Supervisor:	Prof. R. A. Burger
Co-supervisor:	Dr. N. E. Engelbrecht

October 2015

We shall not cease from exploration
And the end of all our exploring
Will be to arrive where we started
And know the place for the first time.
- T.S. Eliot, Four Quartets.

Abstract

Long-term cosmic-ray modulation studies using *ab initio* numerical modulation models require an understanding of the solar-cycle dependence of the heliospheric diffusion tensor. Such an understanding requires information as to possible solar-cycle dependences of various basic turbulence quantities. In this study, 1-minute resolution data for the N-component of the heliospheric magnetic field spanning from 1974 to 2012 is analysed using second-order structure functions constructed assuming a simple three-stage power-law frequency spectrum. This spectrum is motivated observationally and theoretically, and has an inertial, an energy-containing and a cutoff-range at small frequencies to ensure a finite energy density. Of the turbulence quantities calculated from 27-day averaged second-order structure functions, only the magnetic variance and the spectral level show a significant solar-cycle dependence, much less so the spectral index in the energy range. The spectral indices in the inertial range, as well as the turnover and cutoff scales do not appear to depend on the level of solar activity. The ratio of the variance to the square of the magnetic field also appears to be solar-cycle independent. These results suggest that the dominant change in the spectrum over several solar-cycles is its level. Comparisons of the results found in this study with relevant published observations of turbulence quantities are very favourable. Furthermore, when the magnetic variances and heliospheric magnetic magnitudes calculated in this study are used as inputs for theoretically motivated expressions for the mean free paths and turbulence-reduced drift lengthscale, clear solar-cycle dependencies in these quantities are seen. Values for the diffusion and drift lengthscales during the recent unusual solar minimum are found to be significantly higher than during previous solar minima.

Keywords: `turbulence, diffusion, diffusion tensor,`
`solar-cycle, solar-cycle dependence`

Abstrak

’n Verrekening van die sonsiklusafhanklikheid van die heliosferiese diffusietensor is van groot belang vir langtermynstudies van kosmiesestraalmodulasie met numeriese modulasiemodelle. Inligting oor moontlike sonsiklusafhanklikhede van verskeie basiese turbulensiegroothede is noodsaaklik vir sodanige verrekening. Hierdie studie ontleed vervolgens 1-minuut resolusiedata vir die N-komponent van die heliosferiese magneetveld, wat strek van 1974 tot 2012, deur gebruik te maak van tweede-orde struktuurfunksies wat vanuit die aanname van ’n eenvoudige drie-fase magswetfrekwensiespektrum gekonstrueer is. Sodanige spektrum is deur sowel waarnemings as teorie begrond, en bevat ’n inertiaal-, energiebevattende- en afsnygebied by klein frekwensies ten einde ’n eindige energiedigtheid te verseker. Uit die turbulensiegroothede wat vanaf 27-dag gemiddelde tweede-orde struktuurfunksies bereken is, is dit slegs die magnetiese variansie en spektraalvlak wat ‘n beduidende sonsiklusafhanklikheid toon. Die spektraalindeks in die energiebevattende reeks toon heelwat minder afhanklikheid, terwyl die spektraalindeks in die inertiaal gebied, sowel as die omset- en afsnyskaal, onafhanklik blyk te wees van sonaktiwiteite. Die verhouding van die vierkantswortel van die variansie tot die magneetveld dui voorts ook op onafhanklik van die sonsiklus. Hierdie resultate dui daarop dat die dominante verandering oor talle sonsiklusse in die spektrum vlakspesifiek is. In vergelyking met relevante, reeds gepubliseerde waarnemings van turbulensiegroothede is hierdie resultate baie gunstig. Duidelike sonsiklusafhanklikhede kan gesien word wanneer die magnetiese variansie en die heliosferiese magneetveldgroottes wat in hierdie studie bereken is as insette gebruik word vir teoreties-begronde uitdrukkings vir die gemiddelde vryeweg lengtes en dryf lengteskaal. Waardes vir die diffusie- en dryf lengteskale tydens die mees onlangse buitengewone sonminimum blyk ook aansienlik groter te wees as dié tydens vorige sonminima.

Sleutelwoorde: `turbulensie, diffusie, diffusietensor,`
`sonsiklus, sonsiklusafhanklikheid`

Acronyms and Abbreviations

The acronyms and abbreviations used in the text are listed below. For the purposes of clarity, any such usages are written out in full when they first appear.

2D	two-dimensional
AU	astronomical unit
GSE	Geocentric solar ecliptic
HMF	heliospheric magnetic field
RTN	Radial Tangential Normal
CME	Coronal Mass Ejections

Contents

1 Introduction **1**

2 Background **3**

2.1 Introduction 3

2.2 The Sun 3

2.3 Solar Wind 5

2.4 Solar activity 6

2.5 The Heliosphere and Cosmic rays 9

2.6 The Solar and Heliospheric Magnetic Field 11

2.7 The Cosmic Ray Transport Equation and Diffusion Tensor 13

2.8 Energy cascade and the turbulence energy spectrum 13

2.9 Turbulence Models 16

2.10 Spectral Indices 17

2.11 Variances and spectral levels 22

2.12 Summary 25

3 Data Analysis **27**

3.1 Introduction 27

3.2 Data Description 27

3.3 Coordinate Transformation 29

3.4 Constructing the second order structure function 34

3.5 Motivation for choice of data resolution 35

3.6 Choice of underlying turbulence spectrum 37

3.7 Generating magnetic fields with a random fluctuating component 40

3.8 Benchmarking the fitting procedure . . . 46
3.9 Summary and conclusion . . . 51

4 Analysis of IMP and ACE data 53

4.1 Introduction . . . 53
4.2 Second-order structure functions at different levels of solar activity . . . 53
4.3 Magnetic Variance . . . 56
4.4 Inertial Range Spectral Index . . . 69
4.5 Turnover Scale . . . 70
4.6 Level of energy spectrum at 14-hours . . . 72
4.7 Energy-Containing Range Spectral index . . . 73
4.8 Cutoff Scale . . . 74
4.9 Outer Range Spectral Index . . . 75
4.10 Comparisons with other studies . . . 76
  4.10.1 Magnetic Variance . . . 77
  4.10.2 Inertial range spectral index . . . 78
  4.10.3 Turnover Scale . . . 79
  4.10.4 Level of spectrum at 14 hours . . . 80
  4.10.5 Energy Range Spectral Index . . . 80
  4.10.6 Cutoff scale . . . 80
4.11 Summary . . . 82

5 Solar cycle dependent mean free paths and drift scales at earth 83

5.1 Introduction . . . 83
5.2 Elements of the diffusion tensor . . . 83
5.3 Time-dependent mean free paths and drift scale . . . 85
5.4 Summary . . . 91

6 Summary and Conclusions 93

Chapter 1

Introduction

Several turbulence quantities are key inputs for the diffusion tensor, which in turn is a fundamental input for *ab initio* cosmic-ray modulation models. To study long-term modulation, the change of turbulence quantities over several solar-cycles needs to be investigated. In this study, the N-component of the heliospheric magnetic field is analysed over a period from 1974 to 2012. Information about basic turbulence quantities is gathered by constructing second-order structure functions using this spacecraft data. This information is then used to study the possible solar-cycle dependence of the heliospheric diffusion tensor.

Chapter 2 briefly introduces topics related to the Sun and the solar activity cycle relevant to cosmic-ray modulation. An introduction to concepts in turbulence theory applicable to this study is given, and spacecraft observations of various turbulence quantities are discussed.

The data analysis technique used in this study is the topic of Chapter 3. The choice and resolution of spacecraft data used here are discussed and motivated, and the method used to construct second-order structure functions is evaluated in detail. This method is tested using simulated turbulence observations and its sensitivity to data omissions is also investigated.

In Chapter 4 the results of the analysis of spacecraft data spanning a period from 1974 to 2012 are presented. Solar-cycle dependencies of various turbulence quantities are tested using Lomb periodograms. Furthermore, the results presented in this chapter are compared with existing observations reported in the literature. The results of Chapter 4 are then used as inputs for theoretically motivated mean free path and turbulence-reduced drift lengthscale expressions in Chapter 5. Time dependencies are again checked using Lomb periodograms.

The final chapter, Chapter 6, gives a summary of results and conclusions, with suggestions for future research. Some of the results of this study were represented at the 2014 American Geophysical Union (AGU) Fall Meeting in San Francisco (Abstract SH51A-4152).

Chapter 2

Background

2.1 Introduction

In this chapter, general background will be given on the Sun, solar activity and the heliosphere. The focus will be on turbulence at 1 AU, and to a lesser extent on the heliospheric magnetic field (HMF), cosmic rays, and the cosmic-ray transport equation. The turbulence energy cascade will be introduced, which will give more insight into turbulence quantities and their place in heliospheric modelling. Observations reported previously which are relevant to this study will also be discussed.

2.2 The Sun

The Sun is the largest and most prominent object in our solar system. It is a typical star of intermediate size and luminosity with a mass of about 2×10^{30} kg [*Meyer-Vernet*, 2007]. It is composed of mostly hydrogen and helium with traces of other heavier elements such as carbon, nitrogen and oxygen. The Sun is halfway through its main sequence evolution at an age of approximately 4×10^{9} years, and is expected to run out of hydrogen in about 5×10^{9} years, whereupon the Sun will expand and engulf the Earth [*Lang*, 1997]. The Sun is the driving force behind the dynamics of the heliosphere, which is the region around the Sun dominated by plasma of solar origin. This happens by means of interactions between the solar wind, the heliospheric magnetic field and the local interstellar plasma.

The solar interior is divided into four zones shown in Figure 2.1. These are the core region, radiative zone, convection zone and the solar atmosphere. The latter is divided into the photosphere, chromosphere and corona.

The thermonuclear reactions responsible for the release of solar energy occur in the dense, central core, and no energy is generated in this way in the outer regions. The core only accounts for about $1.6\,\%$ of the Sun's volume, but contains about half of the Sun's mass [*Lang*, 1997]. The gas pressure in the core keeps the Sun from collapsing, and is caused by the high speed motions and collisions of particles with temperatures of $\sim 1.5 \times 10^{5}$ K [*Lang*, 1997].

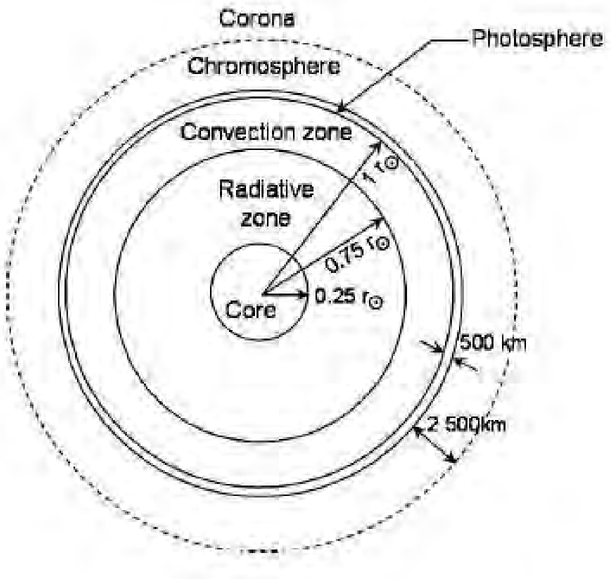

Figure 2.1: The solar interior structure, consisting of the core region, radiative zone, chromosphere and corona [*Krüger*, 2005].

Solar energy is transported from the core towards the solar surface by means of gamma-ray diffusion, through to the radiative zone. Here the high-energy radiation generated at the core interacts with the solar plasma. During these interactions the energy is continuously absorbed, re-radiated and deflected until it eventually moves to the outer regions of lower density, and takes $\sim 1.7 \times 10^5$ years to reach the inner edge of the convection zone (see Figure 2.1) [*Mitalas*, 1992]. At each encounter with the plasma in the radiative zone, the solar radiation downshifts to lower energy and increases in wavelength. By the time the radiation reaches the visible photosphere the X-rays have changed through numerous collisions to ultraviolet radiation and finally to visible sunlight [*Lang*, 1997].

In the convection zone, cool ions absorb great quantities of radiation without re-emitting it. Thus a potential problem of heat transport arises, which is solved by convection currents shifting heat outward. In this zone, the radiative temperature gradient becomes larger, causing the plasma in this region to become convectively unstable. Granules of plasma, or convection cells, convect towards the surface and gives the Sun's surface its granular appearance. Solar convection is the driver that generates the Sun's magnetic fields [*Nordlund et al.*, 2009].

Because the Sun is a gaseous body there is no physical surface, but there is a visible solar surface called the photosphere, where the temperature is ~5780 K [*Lang*, 1997]. The region above the photosphere is referred to collectively as the solar atmosphere and is comprised of two transparent layers: the chromosphere, which extends some 10000 km above the photosphere, and the corona, which expands outward beyond the chromosphere for more than 10^6 km [*Parker*, 1965]. The Sun's atmosphere takes $\sim$ 26 days to rotate at the equatorial region, and decreases towards the poles by about 30% [*Snodgrass*, 1983; *Miesch*, 2005]. This difference in ro-

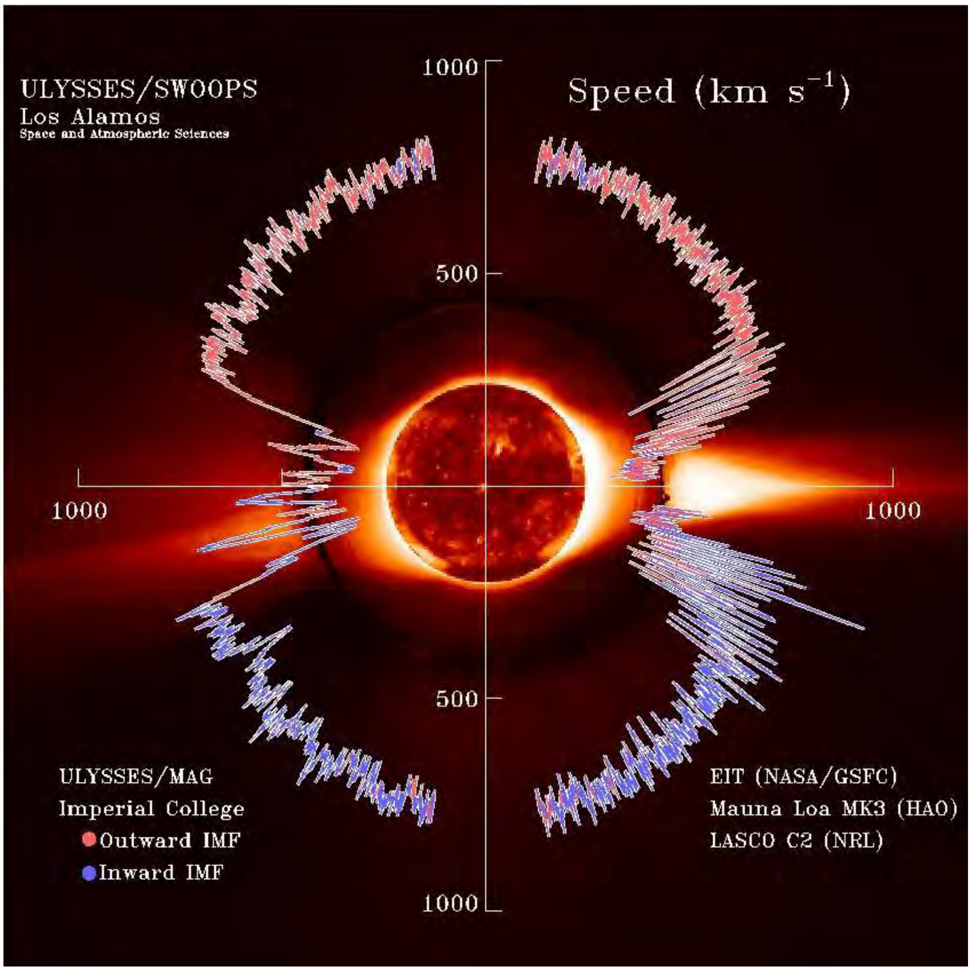

Figure 2.2: The solar wind speed during solar minimum as a function of heliocentric latitude as observed during the first orbit of the *Ulysses* spacecraft [*McComas et al.*, 1998].

tational period is possible because the Sun is not a solid body, but gaseous with no well-defined solid surface [*Sheeley et al.*, 1992].

2.3 Solar Wind

The expansion of the corona causes coronal plasma to be ejected outwards. Neither the solar gravitational attraction nor the pressure of the interstellar medium can confine this plasma, which consists mainly of hydrogen and moves outward at around 400 km/s in the solar equatorial plane. This speed is not uniform and varies depending on the solar latitude and solar cycle. Figure 2.2 shows observations taken by the *Ulysses* space probe. In the figure, bright streamers can be observed at the equator and dark coronal holes at the poles, which are regions on the corona of lower temperature and density [*Cranmer*, 2009]. The solar wind speeds are generally high at the poles ($\sim$ 800 km/s) and lower ($\sim$ 400 km/s) at the equator. During solar cycle maximum however (see Section 2.4), the solar wind speed profile does not have such a simple structure and tends to have alternating fast and slow solar wind speeds at all latitudes.

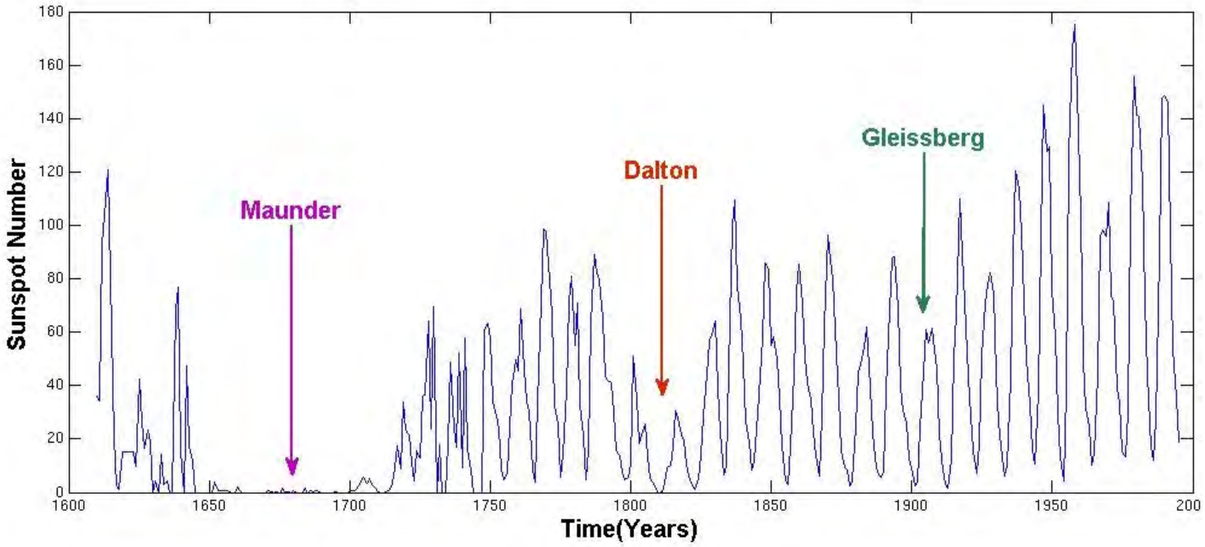

Figure 2.3: The yearly average sunspot number as observed since 1600. Also illustrated here are the 3 grand minima: Maunder, Dalton and Gleissberg. Data taken from NOAA National Geophysical data center, `ftp://ftp.ngdc.noaa.gov/STP/SOLAR_DATA/SUNSPOT_NUMBERS/`.

During all phases of the solar cycle, the fast and slow solar winds interact with each other and can cause large pertubations in the solar magnetic field [*Meyer-Vernet*, 2007].

2.4 Solar activity

The Sun is not in a static state, but rather undergoes various nonstationary active processes [*Usoskin*, 2013]. Every ∼11 years the Sun moves through a period of lower solar activity, solar minimum, and increased solar activity, a solar maximum [see, e.g., *Hathaway*, 2010]. Here a number of solar activity indicators will be discussed, which include flares and sunspots.

Solar flares are defined as a catastrophic release of magnetic energy leading to particle acceleration and electromagnetic radiation on the Sun's surface [*Miroshnichenko*, 2008]. Solar flares release a considerable portion of their energy (up to 10 %) in the form of solar cosmic rays. Through measurement, X-rays have been associated with solar flares, which are sometimes called X-flares [*Hathaway*, 2010].

From observations taken over several decades it has been noted that the solar corona is very unstable, and from time to time structures on the Sun's surface suffer global catastrophic restructuring [*Aly and Amari*, 2007]. Because of the dynamo processes in the interior of the Sun, a strong toroidal magnetic field is produced, which eventually reaches the photosphere and merges into the corona. This emerging magnetic field usually carries electric currents and therefore with it free magnetic energy [*Aly and Amari*, 2007]. This free energy causes a continuous heating of plasma by means of various processes such as magnetic reconnection, which produces big eruptive events called coronal mass ejections (CME). CMEs are characterized

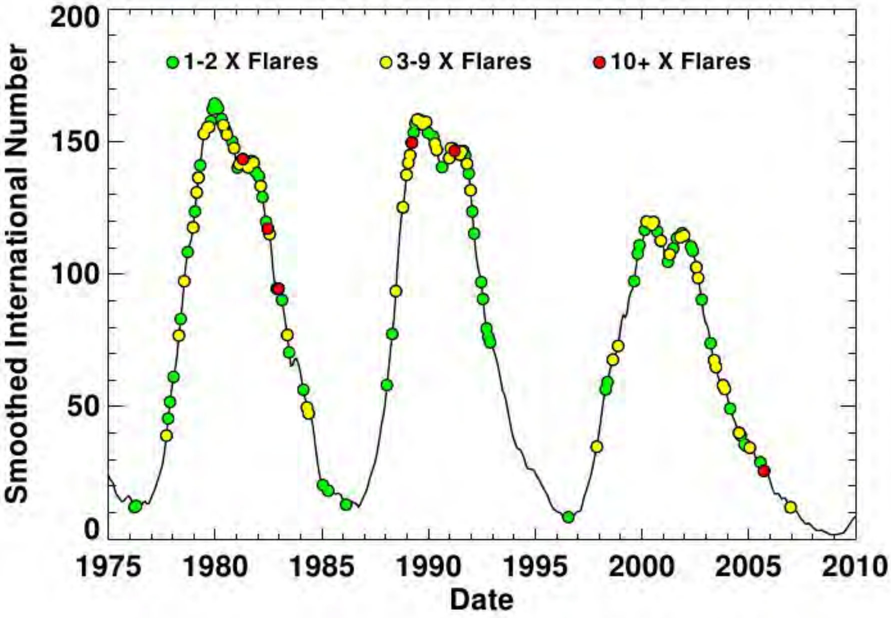

Figure 2.4: Monthly X-class flares and the International Sunspot Number for the past three solar cycles [*Hathaway*, 2010].

by a fast expansion of the field leading to an expulsion of matter. During this process, huge amounts of energy and matter are released and ejected into space. The exact process which initiates these eruptive events is still an ongoing problem in magnetohydrodynamics as discussed by *Aly and Amari* [2007]. The main difference between CMEs and solar flares is that CMEs occur at much greater scales, whereas solar flares are more local events. Although CMEs and solar flares seem to be related to one another, neither one is considered to be the cause of the other [*Webb and Howard*, 2012]. The CMEs frequency seems to be directly linked to the solar cycle, with more occurences at solar maximum, and less at solar minimum [*Webb and Howard*, 2012]. Increases in the number of solar flares and CMEs raise the likelihood that sensitive instruments in space will be damaged by solar energetic particles accelerated in these events [*Hathaway*, 2010].

Sunspots are irregular areas of intense magnetic fields on the surface of the Sun, which appear darker than the surrounding surface. These regions are cooler than the rest of the surface [*Lang*, 1997]. Detailed records of these sunspots have been kept since 1600. Figure 2.3 shows the yearly average sunspot number from 1610 up to 2000. A time when sunspot activity is greatly reduced, is referred to as a grand minimum. Three can be seen in Figure 2.3, of which the earliest was the Maunder minimum in the late 17th century [*Usoskin*, 2013]. It is followed by two more grand minima: the Dalton and Gleissberg minima. Although there was a significant decrease in the sunspot number during these periods, is evidence of an 11 year cycle, known as the Schwabe cycle, seen over the entire span of observations.

Looking over a shorter period of time, Figure 2.4 shows the sunspot counts and number of X-flares for three sunspot cycles. There are clearly three dominant peaks where sunspot counts

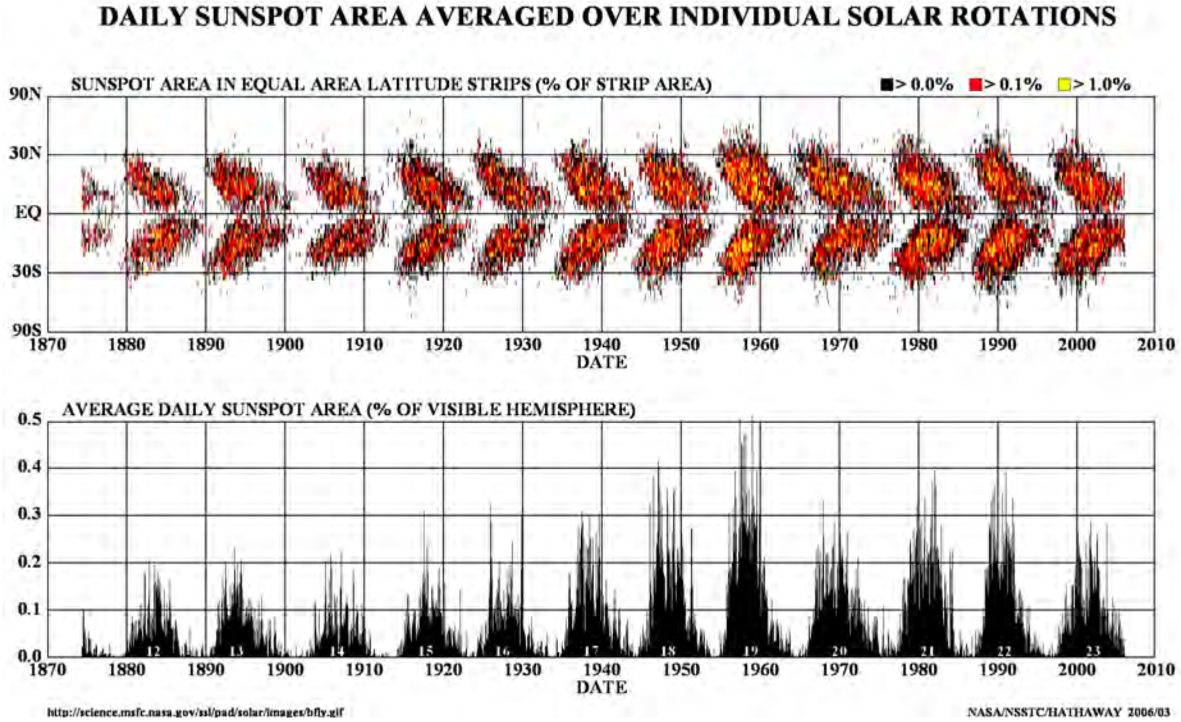
DAILY SUNSPOT AREA AVERAGED OVER INDIVIDUAL SOLAR ROTATIONS

SUNSPOT AREA IN EQUAL AREA LATITUDE STRIPS (% OF STRIP AREA)

AVERAGE DAILY SUNSPOT AREA (% OF VISIBLE HEMISPHERE)

http://science.msfc.nasa.gov/ssl/pad/solar/images/bfly.gif

NASA/NSSTC/HATHAWAY 2006/03

Figure 2.5: The top panel shows the Butterfly Diagram. Sunspots form in both hemispheres, about 25° from the equator, and tend to migrate over time towards the equator. The bottom panel is the average daily sunspot area for each solar rotation since May 1874, plotted as a function of time [*Hathaway*, 2010].

reach a maximum, but one can see that even during the lowest points sunspot activity continues. What can also be seen in Figure 2.4 is the presence of a second maximum, which appears a couple of years after the first one. Investigation of sunspots, coronal line intensity, flares and other solar geophysical data have confirmed the fact that the 11-year cycle consists of two maxima events [*Gnevyshev*, 1976]. Both maxima could be seen in the optical and radio observations to have different features: there is a simultaneous increase of activity all over the Sun during the first maximum, and then again a simultaneous decrease. Then after reaching a minimum it starts to increase again. It was also noted that numerous, small events were observed during the first maximum, and powerful, stable events during the second maximum [*Gnevyshev*, 1976].

From such behaviour it became evident that the Sun has a quasi-periodic 11-year cycle, called a solar activity cycle, which correlates with sunspot numbers and the occurence of CMEs [*Hathaway*, 2010]. Solar flares are also very closely related to the sunspot number and the solar activity cycle, but their behaviour is still very unpredictable and it hasn't yet been established what amount of flares is typical for specific times in the solar cycle.

The International Sunspot Number is the key indicator of solar activity [*Hathaway*, 2010], mainly because of the length of the available record. A more physical measure of solar activity is believed to be sunspot areas [*Hathaway*, 2010]. These sunspot areas were initially estimated by overlaying a grid and counting the number of cells that a sunspot covered. Later it was

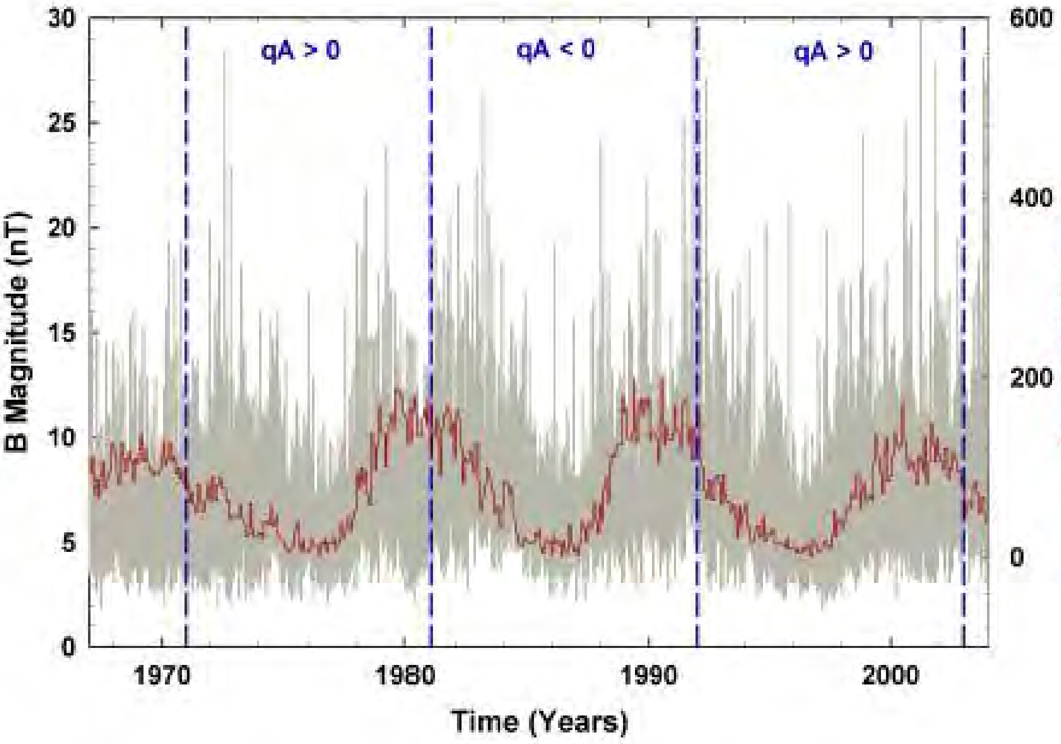

Figure 2.6: Solar cycle variation of the HMF strength at Earth. Here one can clearly see the dependence of the HMF magnitude on the solar cycle. The red line represents the yearly average sunspot number. Data from the NSSDC COHOWeb: http://cohoweb.gsfc.nasa.gov. Figure taken from *Strauss* [2010].

changed to employ an overlay with a number of circles and ellipses with different areas. It became evident that there is a latitude dependence during a solar cycle, called Spörer's law [*Maunder*, 1903], and sunspot datasets were used to show positional information. This is known as the Butterfly Diagram and shown in Figure 2.5 which indicates the sunspot area as a function of latitude and time. The relative sunspot area in equal area latitude strips are illustrated with a color code (top panel). Sunspots form in two bands, one in each hemisphere, and start at about 25° from the equator at the start of a cycle and migrate toward the equator as the cycle progresses.

2.5 The Heliosphere and Cosmic rays

The heliosphere is the region around the Sun dominated by plasma of solar origin. This region moves through the local interstellar medium (LISM). This heliosphere consists of three major boundaries, shown in Figure 2.7: The possible bow shock, termination shock and the heliopause. Within the termination shock the outward-flowing solar wind is supersonic. Between the termination shock and bow shock is the heliopause, which separates the plasma flow of the solar and interstellar wind [*Wood*, 2004]. The LISM in most models is assumed to move at supersonic speed, which is shocked to subsonic speeds at the bow shock. Based on IBEX observations, it has been suggested that the LISM flow speed is sub-fast magnetosonic

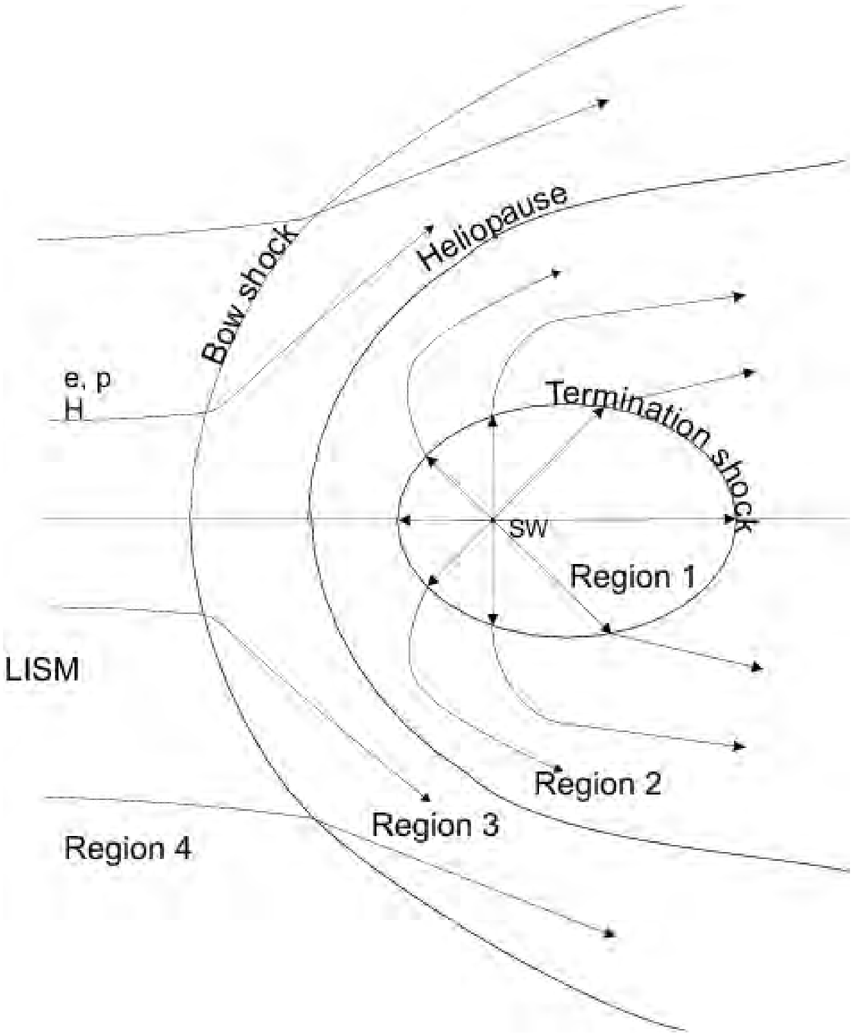

Figure 2.7: Example of the heliosphere and the three dominant interfaces: The termination shock, which is where the solar wind is shocked to subsonic speeds. The bow shock, where interstellar wind is assumed to be shocked to subsonic speeds. Lastly, the heliopause separates the plasma flow of the solar wind and interstellar wind [*Wood*, 2004]

(slower than fast magnetosonic speed), which would mean that the heliosphere does not possess a bow shock [*Zank et al.*, 2013]. This is still under debate and the existence of the bow shock is still undecided [*Scherer and Fichtner*, 2014].

Cosmic rays continuously traverse the heliosphere. These charged particles consist of protons (90 %), Helium nuclei (nearly 10 %) and other nuclei (less than 1 percent) [*Kallenrode*, 2001]. Various types of cosmic rays have been observed, and classified according to their energies and origin. *Galactic cosmic rays* originate beyond the heliosphere, produced by supernovae and active galactic nuclei [*Hathaway*, 2010], generally with energies of a few hundred keV to $\sim$3.2 $\times 10^{20}$ eV. *Anomalous cosmic rays* have a kinetic energy of between 10 to 100 MeV/nuc and start off as neutral particles. Neutrals moving through interstellar space are unaffected by electromagnetic fields until they become ionised when they enter the heliosphere. Most of neutral ionisation occurs in the heliosheath, while only photo-ionisation becomes increasingly effective near the Sun. During this phase *Anomalous cosmic rays* are referred to as pick-up ions, seeing as they are picked up by the solar wind [*Potgieter*, 2013]. *Solar energetic particles* originate, as the name suggests, close to the Sun. The exact region of origin varies, but is linked to solar activity. Their energies tend to be below several hundred MeV. Finally, there are *Jovian electrons* at the lower end of the energy spectrum with energies of around 30 MeV [*Simpson et al.*, 1974]. They originate in Jupiter's magnetosphere.

2.6 The Solar and Heliospheric Magnetic Field

Another phenomenon was observed during the measurement of sunspots: that of the magnetic nature of the solar cycle [*Hathaway*, 2010]. These observations are best described by Hale's Polarity Law for sunspots [*Hale*, 1908]:

> *The preceding and following spots of binary groups, with few exceptions, are of opposite polarity, and that* [sic] *the corresponding spots of such groups in the Northern and Southern hemispheres are also of opposite sign. Furthermore, the spots of the present cycle are opposite in polarity to those of the last cycle.*

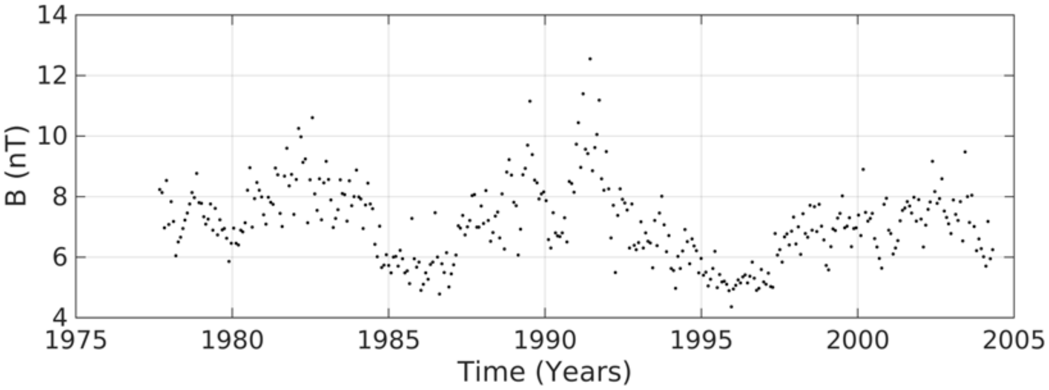

Figure 2.8: Example of magnetic field data taken at 1AU. Data are from the *ACE* spacecraft and spans over two decades. A clear solar cycle dependence can be seen.

Thus with each new cycle the sunspots in both hemispheres change polarity. What was also noticed during observations is that the Sun's polar fields reverse. The polar fields are out of phase with the sunspot cycle, and are at their peak during sunspot minimum [*Hathaway*, 2010]. The other variation, other than that of sunspot numbers, which was noticed with regards to solar activity was found in the magnitude of the measured heliospheric magnetic field (HMF) at Earth. The HMF magnitude at Earth is shown in Figure 2.6. This shows the clear dependence of the HMF magnitude on the solar cycle with higher magnitudes at solar maximum, and lower values at solar minimum. The field strength correlates with the sunspot numbers in an 11-year cycle [*Owens*, 2013]. An example of the *ACE* spacecraft magnetic field data which is used in this study is shown in Figure 2.8, which spans over two decades. Note again the presence of an 11-year periodicity related to the solar activity cycle.

The solar wind carries out the embedded solar magnetic field into the heliosphere forming the HMF [see, e.g., *Parker*, 1958; *Burger*, 2005; *Owens*, 2013]. Magnetic field lines originating from the northern and southern polar coronal holes of the Sun move outward with the solar wind. Different models for the HMF exist. The Parker Field model was the first and simplest to be derived. The components of this magnetic field in spherical coordinates are given as [e.g. *Krüger*, 2005; *Engelbrecht*, 2008]

$$\begin{aligned} B_r &= A\left(\frac{r_e}{r}\right)^2 \\ B_\theta &= 0 \\ B_\phi &= -B\frac{\Omega(r - r_{SS})}{V_{SW}}\sin\theta \end{aligned} \tag{2.1}$$

where r_e is 1 AU, $|A|$ the field magnitude at Earth, V_{SW} is the solar wind speed, r_{SS} is the radial distance where the source surface is located and Ω is the rate at which the Sun rotates. The sign of A denotes the polarity of the field and can be either positive or negative, the former when the solar magnetic field points outward from the North Pole of the Sun and inward at the South Pole, and the latter when the solar magnetic field points inward at the North Pole, and outward at the South Pole. The structure of the Parker field is shown on the left panel of Figure 2.9. The field lines form spirals along cones of constant latitude due to the fact that this field does not have a meridional component. The heliospheric current sheet is the surface dividing the two opposite polarities of the interplanetary magnetic field. It extends from the Sun‘s equatorial plane outward into the heliosphere [*Smith*, 2001].

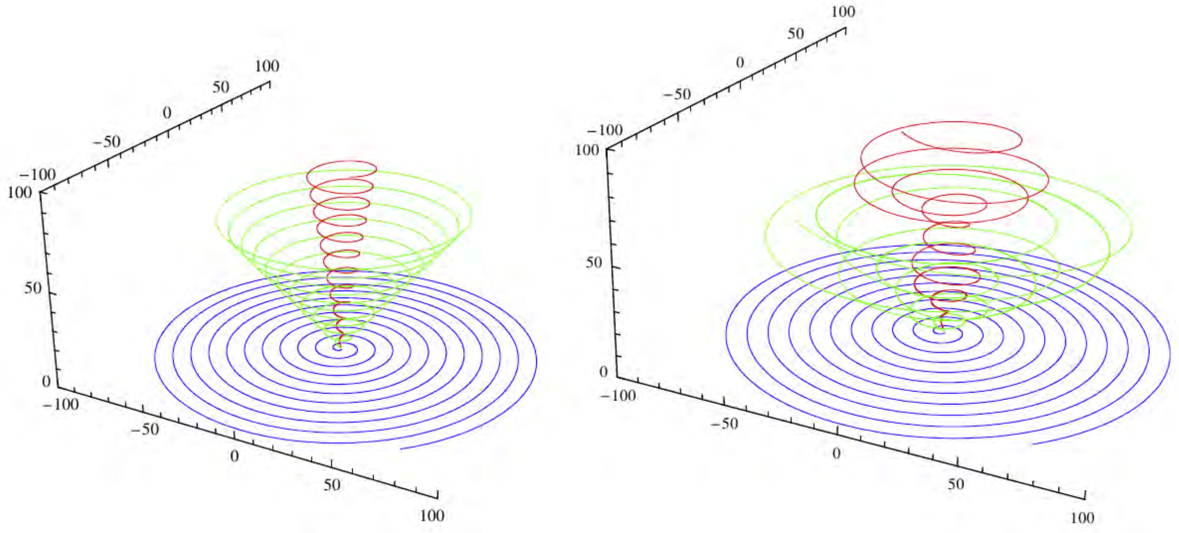

Figure 2.9: An example of an ideal Parker spiral field is shown on the left, where a spiral moving outward can be seen on the equator, and two cones moving outward at the pole. A Parker-Fisk hybrid is shown on the right, which consists of Parker-type regions, Fisk-type regions and Hybrid-type regions. (*Engelbrecht and Burger* [2010]). The latter model has a finite meridional component, in contrast to the Parker Field.

Several alternative models for the HMF have been proposed, most notably the Fisk-type models *Fisk* [1996], and variations such as the Fisk-Parker Hybrid field proposed by *Burger et al.* [2008], and shown in Figure 2.9 on the right. These Fisk-type fields do not have zero meridional components, as can be seen from the fact that field lines wander in latitude.

2.7 The Cosmic Ray Transport Equation and Diffusion Tensor

The modulation of cosmic rays by various mechanisms as they enter the heliosphere is described by the Parker transport equation [*Parker*, 1965]

$$\frac{\partial f_0}{\partial t} = \nabla \cdot \left(\overset{\leftrightarrow}{K} \cdot \nabla f_0 \right) - \mathbf{V}_{sw} \cdot \nabla f_0 + \frac{1}{3} \left(\nabla \cdot \mathbf{V}_{sw} \right) \frac{\partial f_0}{\partial \ln p} + Q \left(\mathbf{r}, p, t \right), \tag{2.2}$$

which is written in terms of an omnidirectional distribution function f_0, $\mathbf{V}_{sw}$ is the solar wind velocity, $\overset{\leftrightarrow}{K}$ the cosmic ray diffusion tensor and Q represents cosmic ray sources within the heliosphere, like the Jovian magnetosphere. The term $\mathbf{V}_{sw} \cdot \nabla f_0$ represents the outward convection of cosmic rays by the solar wind. The term $1/3 \left(\nabla \cdot \mathbf{V}_{sw} \right) \frac{\partial f_0}{\partial \ln p}$ is the change in adiabatic energy of cosmic rays within the heliosphere. Lastly, the term $\nabla \cdot \left(\overset{\leftrightarrow}{K} \cdot \nabla f_0 \right)$ describes cosmic ray drift and diffusion.

If a right-handed coordinate system with one axis parallel and two perpendicular to the magnetic field is assumed, then the diffusion tensor $\overset{\leftrightarrow}{K}$ in Equation 2.2 in field-aligned coordinates is given by [e.g. *Burger et al.*, 2008]

$$\overset{\leftrightarrow}{K} = \begin{bmatrix} \kappa_{\|} & 0 & 0 \\ 0 & \kappa_{\perp,2} & \kappa_A \\ 0 & -\kappa_A & \kappa_{\perp,3} \end{bmatrix}.$$

where $\kappa_{\perp,2}$ and $\kappa_{\perp,3}$ are the diffusion coefficients in directions perpendicular to the mean magnetic field, $\kappa_{\|}$ is the diffusion coefficient parallel to the mean field, and κ_A is the drift coefficient [*Burger et al.*, 2008]. The diffusion coefficients can be calculated from various scattering theories, which in turn require as key inputs basic turbulence quantities [*Shalchi et al.*, 2009]. It is the primary aim of this study to determine such turbulence quantities from spacecraft data. From here an energy spectrum can then be constructed, some basic properties of which are described next.

2.8 Energy cascade and the turbulence energy spectrum

Before the turbulence energy spectrum can be described, a better understanding of turbulence and the energy cascade is required. From early observations, it was concluded that the solar wind flow is turbulent [see, e.g., *Coleman*, 1968]. A fluid system in an unstable state can be referred to as being turbulent [*Choudhuri*, 1998]. This system of turbulent flow consists of a steady, smooth flow component of motion, and a random, fluctuating component of motion [see, e.g., *Davidson*, 2004], such that the total velocity $\mathbf{u}$ can be written as

$$\mathbf{u}(\mathbf{x}, t) = \bar{\mathbf{u}}(\mathbf{x}) + \mathbf{u}'(\mathbf{x}, t) \tag{2.3}$$

where the velocity $\bar{\mathbf{u}}(\mathbf{x})$ is smooth and ordered, and the velocity $\mathbf{u}'(\mathbf{x}, t)$ is highly disordered in space and time. The fluctuating component consists of eddies (or vortices) of different sizes. The largest of these are created by instabilities in the turbulent system. Examples of these include the Kelvin-Helmholtz instability, where two streams flow past each other at different velocities, and create eddies through shear [*Breech*, 2008]. Eddies, illustrated in Figure 2.10, tend to break into smaller and smaller structures, due to internal instabilities. As this happens, energy is transferred from larger to smaller scales. Note that at any instant, there is a broad spectrum of eddy sizes of which each breaks down to smaller ones within fully developed turbulence. The breakdown of eddies continues until some minimum eddy size is reached, and the energy dissipates. At this point energy is converted mainly to thermal energy. This transference of energy from bigger to smaller structures is called the energy cascade [*Davidson*, 2004].

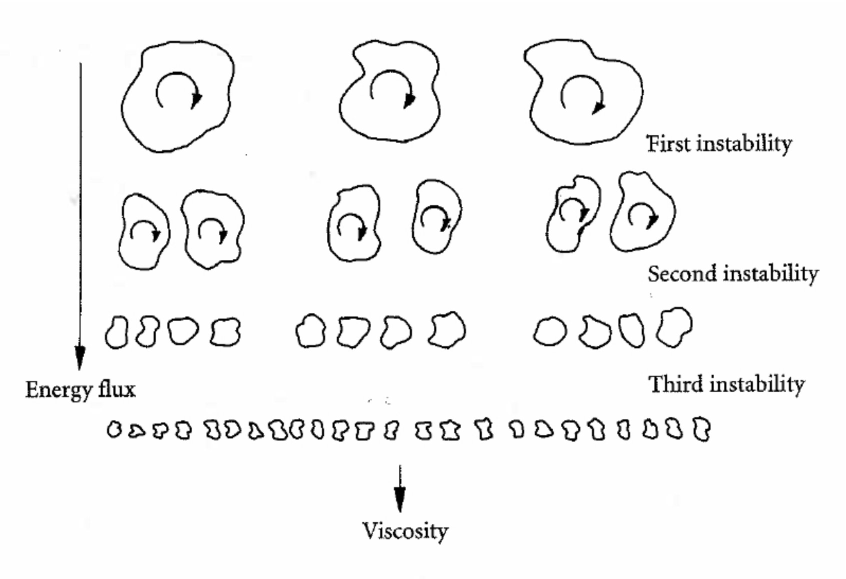

Figure 2.10: Schematic representation of an energy cascade, where a breakdown of eddies from larger to smaller scales occur. This is caused by various types of instabilities, and energy is transferred in the process [*Davidson*, 2004].

The above was a very general discussion of turbulent flow. The next example is specifically of the turbulent heliospheric magnetic field. Gas pressure from the solar corona drives the flow outward, and this drive generates pertubations in the magnetic field, which in turn becomes turbulent [*Breech*, 2008]. Further turbulent structures are created by, e.g., shear instabilities.

The field is assumed to consist of a uniform magnetic field background component $\mathbf{B_0}$ and a fluctuating component $\mathbf{b}$ [*Breech*, 2008]

$$\mathbf{B} = \mathbf{B_0} + \mathbf{b}. \tag{2.4}$$

where $\langle \mathbf{b} \rangle = 0$ over long periods [*Choudhuri*, 1998]. It then follows that $\mathbf{B}$ would, over a long enough period of time, average to $\mathbf{B_0}$. This component is well described by the Parker HMF model [see, e.g., *Klein et al.*, 1987].

In order to investigate the properties of turbulence, one should look at statistical quantities which give insight into the state of turbulence. Two of these are the velocity correlation function, and the energy spectrum [*Davidson*, 2004]. The velocity correlation tensor is given by *Batchelor* [1970], as

$$R_{ij}(\mathbf{r}) = \overline{u_i(\mathbf{x})u_j(\mathbf{x}+\mathbf{r})} \tag{2.5}$$

where the distance between the two points is given by a separation vector $\mathbf{r}$. The correlation function (2.5) has substantial non-zero values only if r lies within a certain range. This is called the correlation length of turbulence λ_{CS}. This quantity is a measure of the correlation between fluctuations separated in space. For example if a sinusoid wave with single frequency is assumed for the fluctuation, there will be an infinite correlation length ($\lambda_{CS} \approx \infty$), as there is no turbulence to cause decorrelation. Add then an infinite amount of frequencies of random values, and a very small correlation scale is the result ($\lambda_{CS} \rightarrow 0$), seeing as u_i and u_j are only correlated over short distances [*Choudhuri*, 1998]. When $\mathbf{r} = 0$ it is also a measure of the kinetic energy (strength) of turbulence (referred to as variance).

An expression for the energy spectrum can be obtained from the corresponding Fourier transform of Equation 2.5. A typical energy spectrum is shown in Figure 2.11. This energy spectrum is divided into different ranges. The energy-containing range is where, as the name implies, energy is injected into the system by various processes [*Davidson*, 2004; *Matthaeus et al.*, 1994]. At 1 AU this range is observed below 10^{-7} Hz (116 days) and through various spacecraft observations a spectral index has been detected ranging from 0 to -1 [*Goldstein and Roberts*, 1999].

At scales where energy is no longer added to the system, the large energy-containing eddies start to break down into smaller eddies [*Davidson*, 2004], forming the inertial range, observed from 10^{-5} s^{-1} and 0.1 s^{-1} [*Goldstein and Roberts*, 1999], where inertial forces between the fluctuations are the lead cause for energy transfer in this range [*Batchelor*, 1970]. The rate of decay behaves as a power law that will be discussed in Section 2.10.

At the highest wavenumber, the small-scale dissipation range can be found, with a steeper spectral index than the inertial range [*Smith et al.*, 1990]. Here the fluctuations are converted to thermal energy, which leads to heating of the background plasma [*Goldstein et al.*, 1995].

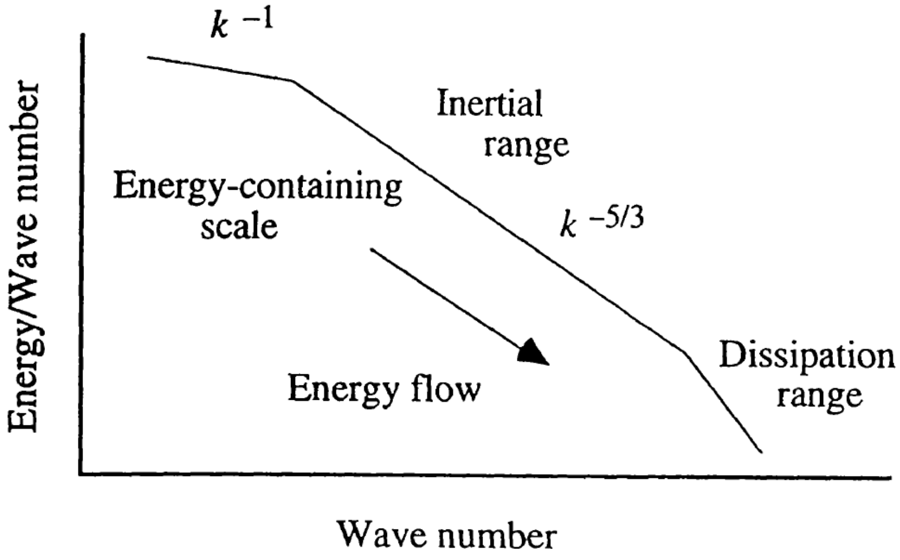

Figure 2.11: A schematic representation of the logarithm of the energy spectrum, in terms of the logarithm of the wavenumber. At low wavenumber the energy-containing range can be seen with a typical k^{-1} wavenumber dependency. The inertial range, at intermediate wavenumbers, shows a *Kolmogorov* [1941] inertial range wavenumber dependency, which is followed by a steeper dissipation range at the highest wavenumbers.

2.9 Turbulence Models

As shown in Equation 2.4, the turbulent magnetic field can be decomposed into the uniform background magnetic field B_o and the transverse fluctuating component $\mathbf{b}$. Defining a right-handed Cartesian coordinate system, with the z-component along $\mathbf{B_o}$, the total field $\mathbf{B}$ can then be written as [*Bieber et al.*, 2004]

$$\mathbf{B}(x, y, z) = B_o \mathbf{e}_z + \mathbf{b}(x, y, z). \tag{2.6}$$

By taking the average of the square of the fluctuating component we get the variance δB^2. In the case of slab turbulence the fluctuating component is only a function of z, and the total field is given by

$$\mathbf{B}(x, y, z) = B_o \mathbf{e}_z + b_{slab,x}(z)\mathbf{e}_x + b_{slab,y}(z)\mathbf{e}_y. \tag{2.7}$$

Here the fluctuating component is uniform in the xy-plane and only changes in the z-direction.

For 2D turbulence, $\mathbf{b}$ is xy-dependent, and independent of z, and the total field is given by

$$\mathbf{B} = B_o \mathbf{e}_z + b_{x,2D}(x, y)\mathbf{e}_x + b_{y,2D}(x, y)\mathbf{e}_y. \tag{2.8}$$

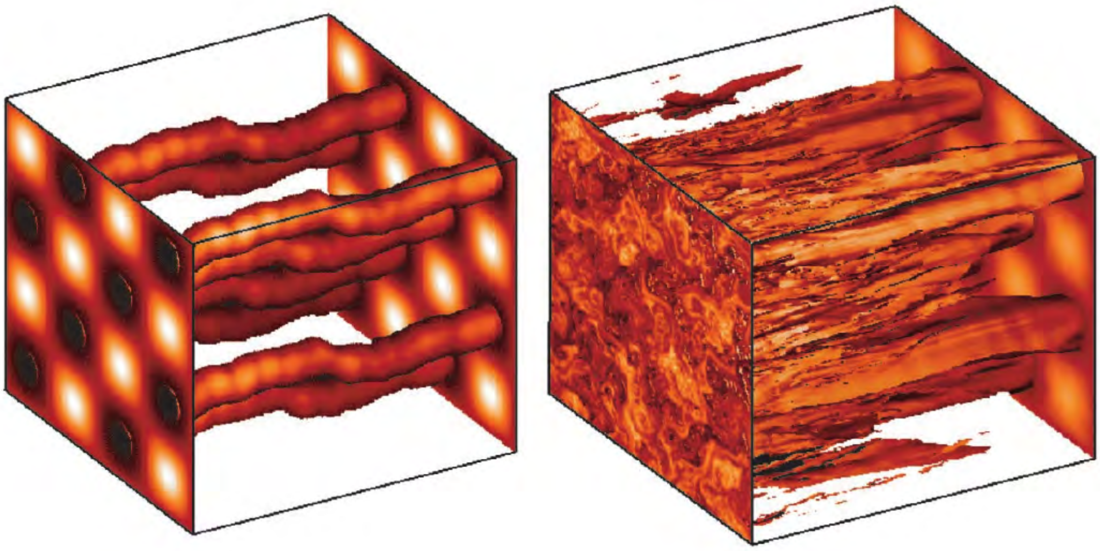

Figure 2.12: The left diagram shows magnetic flux tubes in the presence of pure slab turbulence. The right diagram shows the same flux tubes in the presence of an 80/20 mixture of slab and 2D turbulence, known as composite turbulence [*Matthaeus et al.*, 2003].

The very different behaviour of field lines in the presence of slab turbulence and in the presence of 2D turbulence is shown in Figure 2.12. In the case of slab turbulence (left panel), two field lines originating at different positions in the (x,y) plane will have exactly the same trajectory as they are traced in the z-directions, the displacement between them remaining the same as the initial displacement. In contrast, when 2D turbulence is present, (right panel) the displacement between two field lines changes rapidly as function of distance alows the field. This is because the fluctuations at one position in the (x,y) plane can be very different from the fluctuations at even a nearby position. This will cause the field lines to move in different directions.

By combining the Slab and 2D turbulence models, a so-called composite turbulence model, denoted by

$$\delta \mathbf{B}_{comp} = \mathbf{b}_{slab}(z) + \mathbf{b}_{2D}(x, y), \tag{2.9}$$

is obtained. The right panel of Figure 2.12 shows flux tubes experiencing composite turbulence with 80 % 2D and 20 % slab components. From spacecraft observations, this model has been found to reasonably describe solar wind turbulence [*Matthaeus et al.*, 1995; *Bieber et al.*, 1996].

2.10 Spectral Indices

A power spectrum, with a time series spanning more than a year, was constructed by *Goldstein and Roberts* [1999] from solar wind magnetic field data taken at 1 AU and is shown in Figure 2.13. The energy-containing range can be seen here, extending from roughly 4×10^{-5} Hz

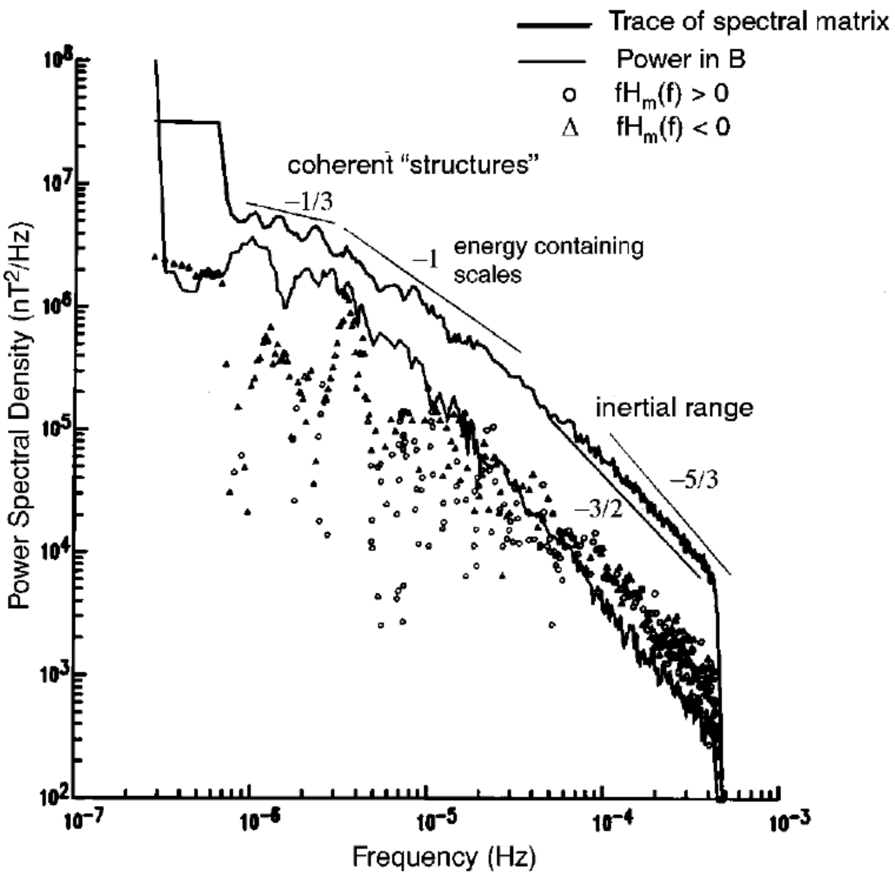

Figure 2.13: A power spectrum of heliospheric magnetic field data at 1 AU, at time scales from a month to a year. Here several ranges can be discerned: the energy-containing range and the inertial range, as well as coherent structures at the lowest frequencies [*Goldstein and Roberts*, 1999].

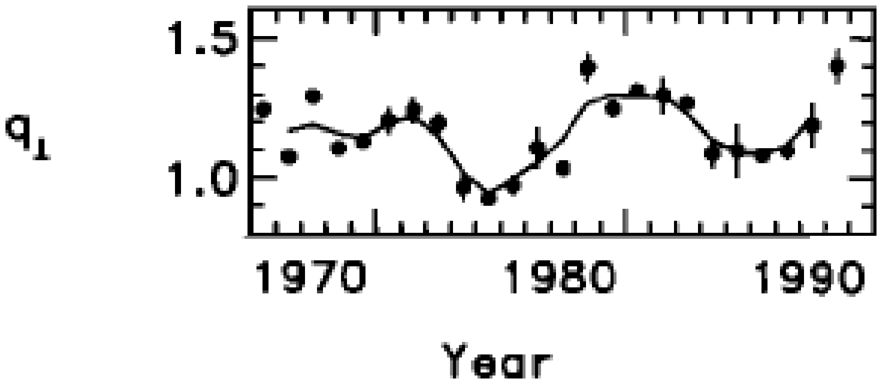

Figure 2.14: Energy range spectral indices reported by *Bieber et al.* [1993].

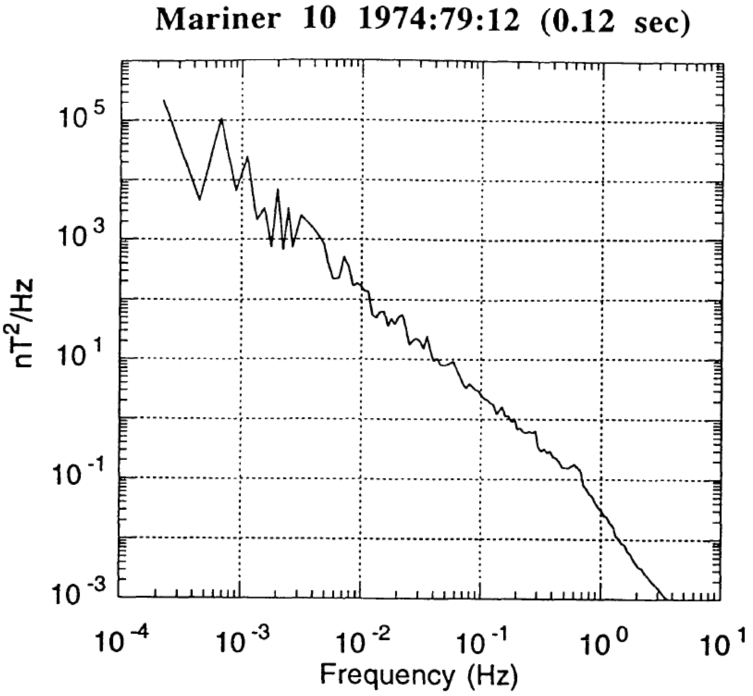

Figure 2.15: A power spectrum constructed from Mariner 10 magnetometer data. The inertial range spectral index is reported as $-5/3$ [*Goldstein et al.*, 1995].

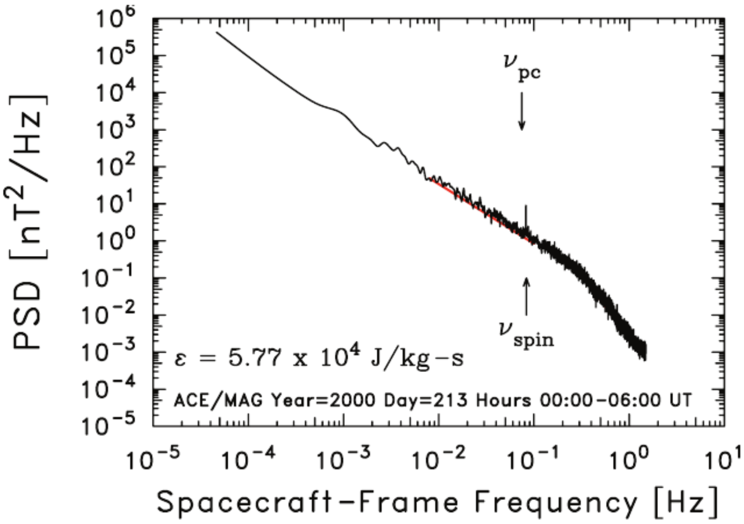

Figure 2.16: Example of a power spectrum, constructed from a database of interplanetary magnetic field measurements, taken at 1 AU with *ACE* spacecraft [*Smith et al.*, 2006a].

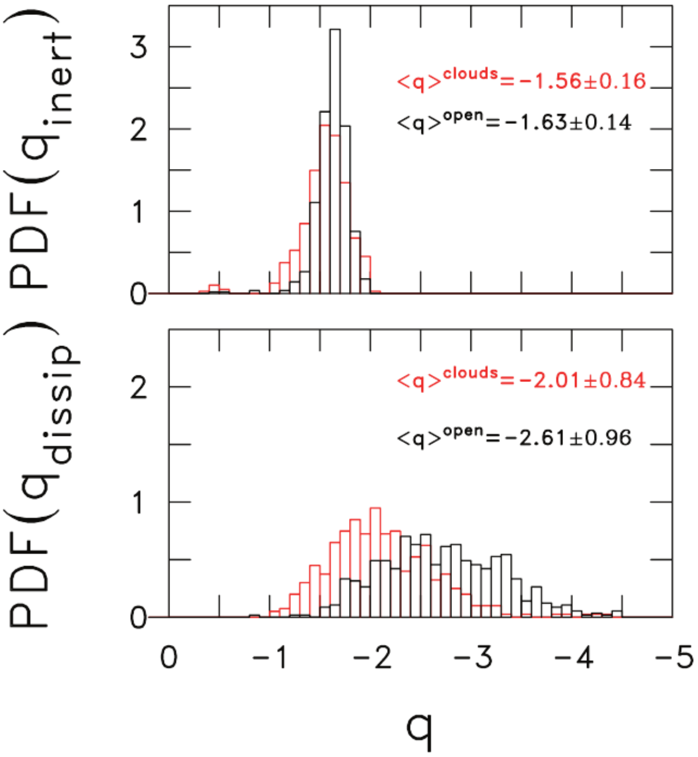

Figure 2.17: The top panel shows a histogram of the inertial range spectral indices and the bottom panel the dissipation range spectral indices. Note the narrow distribution of the inertial range spectral indices compared to the dissipation range spectral indices [*Smith et al.*, 2006a].

(~7 hours) to 4×10^{-6} Hz (~3 days). It was observed to have a spectral index of around -1 [*Goldstein and Roberts*, 1999]. Earlier observations also found the spectral index of this range to be ~ -1 [*Russell*, 1972]. A range at the very lowest frequencies further outward from the energy-containing range can be seen at time scales of a few to tens of days. The spectral index here is roughly -1/3 but is highly variable. This is due to coherent motions [*Goldstein and Roberts*, 1999].

In *Bieber et al.* [1993] yearly averaged power spectra were calculated from interplanetary magnetic field data at 1AU, taken from 1965 to 1988. The perpendicular spectra defined by these authors are not identical to the spectra that will be used in this study, but are comparable (see *Bieber et al.* [1993]). By using the Blackman Tukey analysis, annual means of the magnetic spectra spectral index were calculated by fitting a power law over the energy-containing range. They chose this range from 2.7×10^{-6} to 8.0×10^{-5} Hz, and their findings are shown in Figure 2.14. These authors report a minimum value of -1.4 and a maximum of -0.93, with an average value of -1.1671. The IMF spectra reported by *Bieber et al.* [1993] also tend to be steeper and have larger amplitudes during periods of high solar activity.

As the frequency increases, there is a break and the energy range gives way to the inertial range. This break where the energy range ends and the inertial range commences is called in this study the turnover scale. The turnover scale can in theory be calculated from the correlation length [*Matthaeus et al.*, 2007]. In this study however, the turnover scale will be derived directly from the turbulence energy spectrum.

The energy transfer rate in the inertial range for ideal isotropic incompressible Navier-Stokes fluid turbulence has been generally predicted and observed to be the *Kolmogorov* [1941] value [e.g., *Coleman*, 1968; *Bruno and Carbone*, 2005], such that

$$E(k) \sim k^{-5/3}. \tag{2.10}$$

Early solar wind observations could not distinguish between this $f^{-5/3}$ slope, and a $f^{-3/2}$ slope, which was predicted by *Kraichnan* [1965] for ideal isotropic incompressible magnetohydrodynamic turbulence, and is known as the Iroshnikov-Kraichnan spectrum [*Bruno and Carbone*, 2005], such that

$$E(k) \sim k^{-3/2} \tag{2.11}$$

The difficulty of distinguishing between the $f^{3/2}$ and $f^{-5/3}$ dependencies is clearly shown in Figure 2.13, where *Goldstein and Roberts* [1999] include lines in the figure with both frequency dependencies, which both follow the trend of the data reasonably well. A spectrum constructed from Mariner 10 data (Figure 2.15) also shows an inertial range spectral index of $-5/3$ (see *Goldstein et al.* [1995]), with a break to a clearly defined steeper dissipation range at around 0.8 Hz. *Podesta et al.* [2007] also found a dependency of $f^{-5/3}$ for magnetic field fluctuations in the inertial range.

From other observations (see Figure 2.16, top panel) the inertial range can be seen spanning from 10^{-4} Hz to 0.3 Hz, with a spectral index of -1.57 ± 0.01 [*Smith et al.*, 2006a]. *Smith et al.* [2006a] report the observed distribution of the inertial and dissipation range spectral indices, as shown in Figure 2.17. Note that for the distribution of both spectral indices there are two average values: one for magnetic clouds, and one for open field lines. Magnetic clouds are believed to be closed magnetic field loops with both ends anchored to the Sun, whereas the term $< q >^{open}$ refers to open field lines, which are only connected to the Sun at one end. The inertial range spectral index reported by these authors is between -1 and -2 . The spectral index distribution for the dissipation range spectral index however, spans a broader range from -1 to -4. One can also see here that the dissipation range tends to be steeper than the inertial range. Note however that measurements taken to construct Figure 2.13 were not made at a high-enough resolution to resolve the dissipation range in *Goldstein and Roberts* [1999].

2.11 Variances and spectral levels

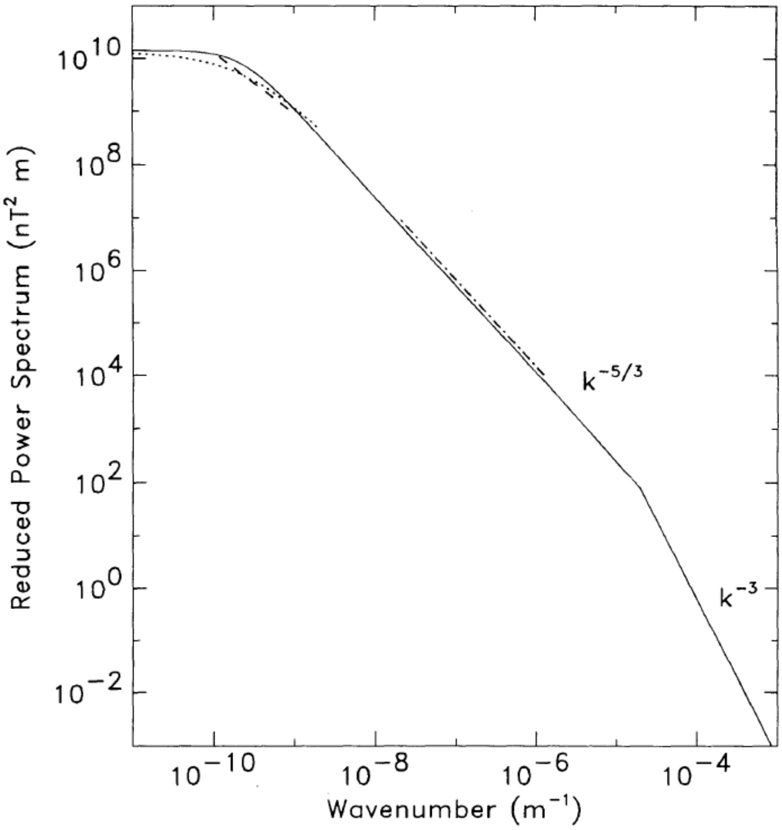

Figure 2.18: Power spectrum constructed by *Bieber et al.* [1994]

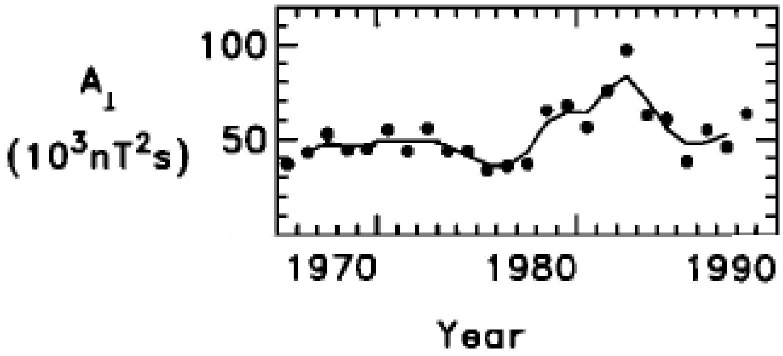

Figure 2.19: Amplitude of the perpendicular magnetic frequency spectra [*Bieber et al.*, 1993].

A model spectrum was constructed by *Bieber et al.* [1994], based on observed interplanetary magnetic spectra (see Figure 2.18). This was derived from survey results over multiyear periods. Model spectrum parameters were adjusted by *Bieber et al.* [1994] so that the model spectrum's level corresponded to those of the observed spectra. The variance value thus calculated was reported by *Bieber et al.* [1994] to be 13.2 nT^2, a value consistent with observations reported by *Matthaeus et al.* [1986]. When assuming axisymmetry, the total variance would then be 26.4 nT^2.

This can be compared with spacecraft observations reported by *Smith et al.* [2006b], shown in Figure 2.20 (top panel). Here a clear solar cycle dependence can be seen, spanning over three decades. Magnetic data used was $\langle B_N^2 \rangle$, which is the N-component of the RTN coordinate system. The N-component of the RTN coordinate system corresponds most closely to the θ-component in spherical coordinates as discussed in Section 2.6. This means that over long enough time periods, B_N would primarily contain the fluctuating component of the turbulent magnetic field. See Section 3.2 for a more detailed discussion of this.

For solar maximum a value of $\sim$ 18 nT^2 can be inferred from the *Smith et al.* [2006b], and for solar minimum $\sim$ 5 nT^2. Again assuming axisymmetric fluctuations, a maximum value of 36 nT^2 is found and a minimum of $\sim$ 10nT^2. Comparing these values with that of *Bieber et al.* [1994], one can see that it falls between the maximum and minimum value. Taking into account that data employed by *Bieber et al.* [1996] were taken over various periods, mostly those of ascending solar activity, their variance value does then appear to agree with values inferred from results reported by *Smith et al.* [2006b]. A diffusion coefficient will therefore change by a factor of about four between solar minimum and solar maximum if its dependence on only the variance is taken into account.

[*Bieber et al.*, 1993] also report spectral levels, taken at a level of 14 hours. These are shown in Figure 2.19. These authors report that the spectral level shows a possible solar cycle depen-

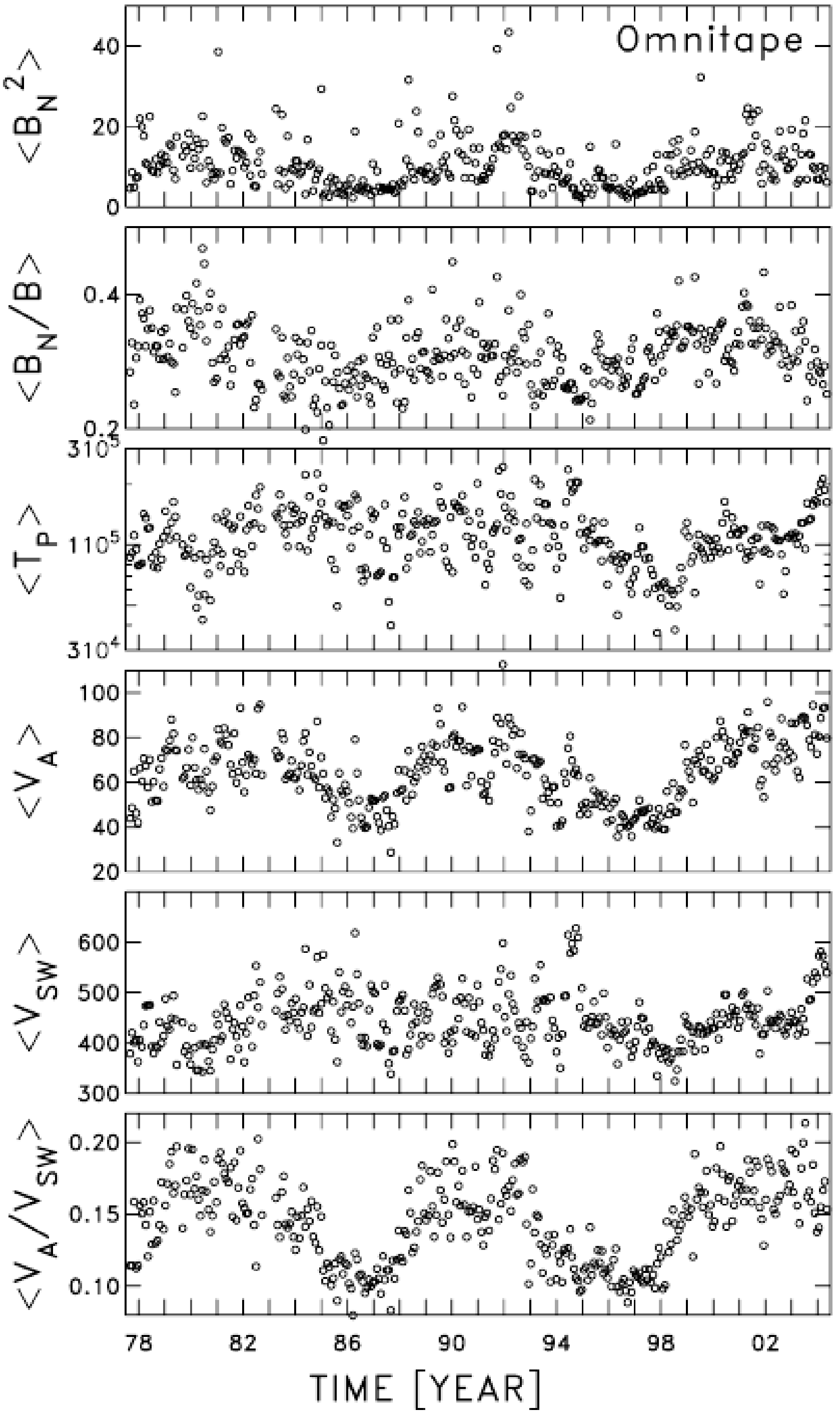

Figure 2.20: Averages of Omnitape data at 1AU [*Smith et al.*, 2006b].

dence, with larger values corresponding to periods of increasing solar activity.

2.12 Summary

A general background of heliospheric physics relevant to this study was given, and the turbulent energy spectrum‘s place in it. The magnetic field was discussed, pointing out the difference between the background and fluctuating components. Turbulence models and certain turbulence quantities relevant to this study (for example the magnetic variance) which have been observed in previous studies, were discussed. The following chapter concerns itself with the introduction of a novel method by which these turbulence quantities can be calculated from spacecraft data spanning the last three solar cycles.

Chapter 3

Data Analysis

3.1 Introduction

The purpose of this study is to determine the solar-cycle dependence of the heliospheric diffusion tensor. This tensor depends on turbulence quantities and, e.g., the heliospheric magnetic field magnitude. A quantity like the magnetic field magnitude is easily determined from spacecraft observation without requiring much analysis. The properties of the underlying turbulence spectrum are, on the other hand, not that simple to determine. Usually a Fourier analysis is performed which seems to almost always require some sort of filtering to yield good results [see, e.g., *Bieber et al.*, 1993]. In this study we use a second-order structure function [see, e.g., *Matthaeus et al.*, 2012] rather than Fourier analysis. Usually the emphasis when using second-order structure functions is on the inertial range of fluctuations [see, e.g., *Ni and Xia*, 2013; *Miranda et al.*, 2012]. In contrast, in this study the attempt is made to infer information about the whole of the turbulence spectrum. We are not aware of any such previous study.

3.2 Data Description

For the analysis, data taken by spacecraft at 1AU were required. About 40 years of heliospheric magnetic field data are needed for the analysis of the behaviour of turbulence quantities over three solar activity cycles, and more than one satellite's data were required to achieve this.

IMP-8, which operated from 1973 to 2006, was in a near-circular, 35 Earth radii orbit. It spent around 7 to 8 days in the solar wind during each 12.5 day orbit [*Balogh*, 2011]. The heliospheric magnetic field, however, was only measured until mid-2000, when the magnetometer aboard *IMP*-8 failed permanently.

The Advanced Composition Explorer (*ACE*) mission was launched on August 25 1997, and its observations already span several solar cycles. Level 2 magnetic field data from the attached magnetometer (MAG) were used here. Raw *ACE* data undergo several phases of processing, which include time ordering, removal of duplicate data and the conversion of magnetic field data to useful coordinate systems. This processing is done by the *ACE* Science Centre, and the final result is level 2 data suitable for scientific study. MAG measures the local interplanetary magnetic field (IMF) direction and magnitude and is establishing the large scale structure and fluctuation characteristics of the IMF at 1 AU, in the direction of the Sun, as function of time. The instruments feature a very wide dynamic range of measurement capability, from 0.004 nT up to 65536 nT per axis in eight discrete ranges ([*Stone et al.*, 1998] and http://helios.gsfc.nasa.gov/ace/mag.html).

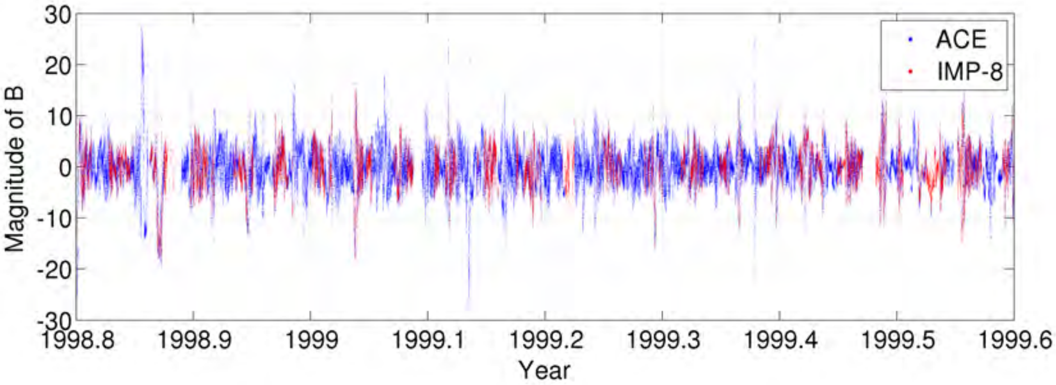

Figure 3.1: Excerpt of *IMP*-8 and *ACE* magnetic field data taken over roughly a year. The blue points are *ACE* data, and red *IMP*-8 data. Note that *ACE* data is nearly continuous, with scattered, random omissions, whereas *IMP*-8 has periodic gaps. These gaps are time spent within the magnetosphere, when no solar wind data could be collected.

Combining data from *IMP*-8 and *ACE* provides heliospheric magnetic field data from 1973 - 2013, which spans three solar activity cycles. An excerpt is shown in Figure 3.1 which spans roughly a year from mid 1998 to mid 1999. The *ACE* dataset has very few bad data points, and these are scattered throughout that particular period. Bad data in this instance refers to times where data were omitted for whatever reason. *IMP*-8 data, apart from scattered omissions, also has significant gaps. These are times spent within the magnetosphere when no solar wind data could be collected. It is obviously important to check that when using observations from two different satellites, the data are indeed comparable. *IMP*-8 and *ACE* do not follow the same orbit, and therefore the magnetic field data are taken at different locations. A solution for the people responsible for these data was to time shift *ACE* and *IMP*-8 to the Earth's bow shock nose. In this time-shift method, field and plasma parameters are determined at a certain time, using the bow shock model of *Farris and Russell* [1994], while the magnetopause model of *Shue et al.* [1997] was used to determine where the bow shock would be when the phase front reaches it.

IMP-8 and *ACE* data at the resolution required for the present study are given in the geocentric solar ecliptic (GSE) coordinate system. These data must therefore be transformed to our system of choice, as is described in the next Section.

To extract turbulence quantities from the data, preferably only the fluctuating component of

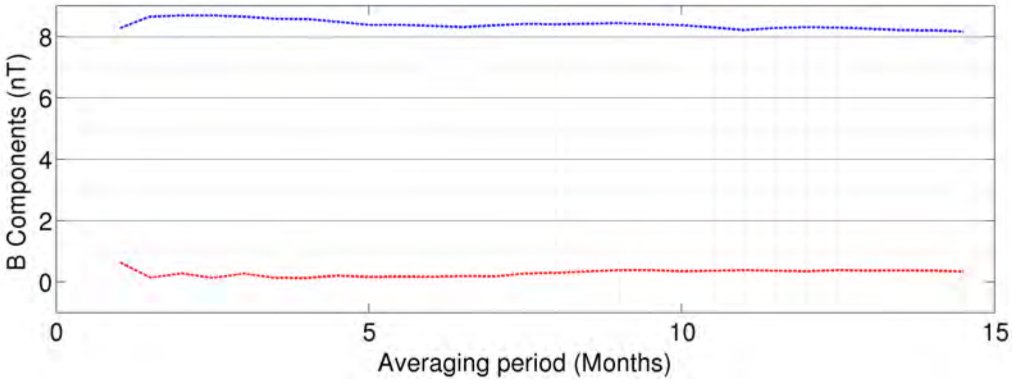

Figure 3.2: Solar magnetic field data from *ACE* spacecraft, showing both the B_N-component (red line) and $\sqrt{B_R^2 + B_T^2}$ (blue line) staring on day 262 of 1999, averaged over periods up to 14.5 months.

the magnetic field should be considered. The background field in the ecliptic plane is usually assumed to be a Parker spiral [*Parker*, 1958]. This is discussed in Section 2.6. This is a reasonable assumption, given observations reported *Klein et al.* [1987]. From Equation 2.1, it can be seen that the B_θ-component of $\mathbf{B_0}$ is zero if a Parker field is assumed. Therefore, over shorter time periods, a measurement of the θ-component of $\mathbf{B}$ would primarily contain the fluctuating component of the turbulent magnetic field. In Figure 3.2, the B_N-component is averaged over periods of increasing length. Also shown is the magnitude of the two other components, $\sqrt{B_R^2 + B_T^2}$ which according to the Parker model contain the uniform background magnetic field. It can readily be seen that $\langle B_N \rangle \approx 0$ over long periods. More specifically, we find that $\langle B_N \rangle = 0.34$ nT during this period, while $\langle \sqrt{B_R^2 + B_T^2} \rangle = 8.2$ nT. Since typical values of the variance are around 10 nT^2 [see, e.g., *Smith et al.*, 2006b], the magnitude of the fluctuations is about ten times larger than the mean field value. One could therefore use the N-component as if it were the fluctuating component without subtracting a mean value, without making too big an error.

3.3 Coordinate Transformation

The geocentric solar ecliptic (GSE) coordinate system is shown in Figure 3.3. It is Earth-centered and consists of an x-axis pointing towards the Sun, a z-axis that points in the direction of the ecliptic North Pole, and the y-axis that completes the right-handed triad. In this study the N-component from the radial tangential normal (RTN) coordinate system of the solar magnetic field is required. This partly because we want to compare with another study which presents data for this component, and partly because in modulation studies heliographic spherical coordinates are usually used, which are comparable with RTN coordinates. The RTN system is, shown in Figure 3.4. Here the $\mathbf{R}$-direction points away from the Sun to the point of observation, $\boldsymbol{\Omega}$ is the rotation vector of the Sun, and $\boldsymbol{\Omega} \times \mathbf{R}$ defines the $\mathbf{T}$-direction. The $\mathbf{N}$-direction completes the right-handed triad and is defined by $\mathbf{R} \times \mathbf{T}$.

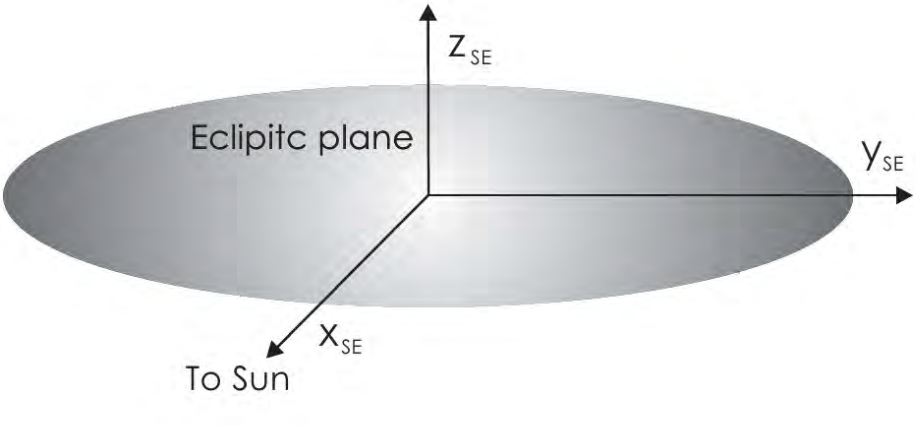

Figure 3.3: The GSE coordinate system, which is Earth-centered. Its x-axis points towards the Sun, the y-axis points towards dusk, and the z-axis is parallel to the Ecliptic North pole.

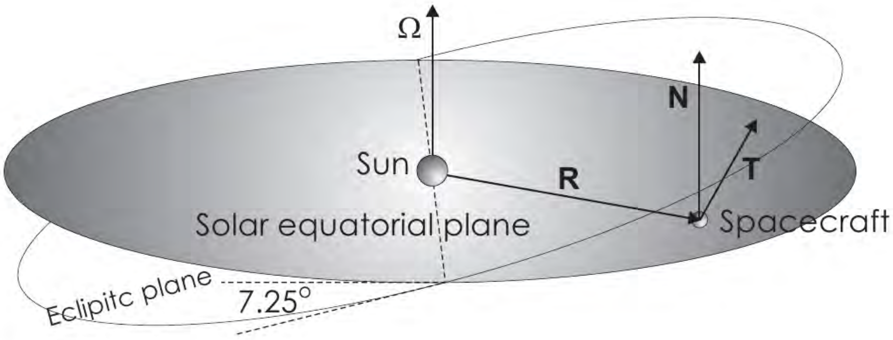

Figure 3.4: The RTN coordinate system, which is Sun-centered. The vector **R** is directed from the Sun to the point of observation, **T** is in the direction of $\mathbf{\Omega} \times \mathbf{R}$, and **N** in the direction of $\mathbf{R} \times \mathbf{T}$.

Consider a spacecraft remaining in the ecliptic plane: from its perspective, the Sun's rotation vector $\mathbf{\Omega}$, when projected onto the GSE system's yz-plane, will change its orientation with respect to the z-axis. It will change over a period of a year, the time it takes for the Earth to move around the Sun, between an angle of -7.25° and 7.25°. Programs are available to calculate the orientation of $\mathbf{\Omega}$, for example `http://users.telenet.be/j.janssens/Engobserveren.html#Solcoord`. In Figure 3.5 several angles are shown that are used to calculate the orientation of the solar rotation vector with respect to the GSE coordinate system. The time-dependent angle β follows from the rotation vector projected onto the xy-plane, and varies from 0° to 360°. The angle between the rotation vector and the z-axis is δ, and is fixed at 7.25°. The third angle, γ, is the projection of the rotation vector onto the xz-plane and changes between $-7.25°$ and 7.25°. The change of the solar rotation vector over a period of a solar year as seen from Earth is shown in Figure 3.6.

The angles γ and β are related by

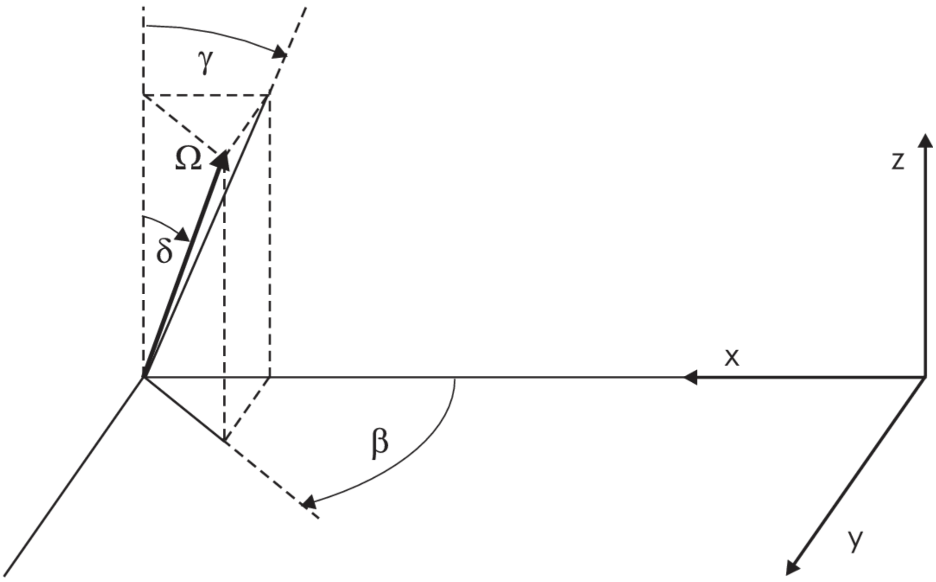

Figure 3.5: Angles used to calculate the orientation of the solar rotation vector with respect to the GSE coordinate system. The angle δ is a constant at 7.25° (not shown to scale). The angle γ is between the z-direction and the projection of the vector on the xz-plane and changes from -7.25°to +7.25°. When it is negative the Earth is below the solar equatorial plane and positive when it is above the plane.

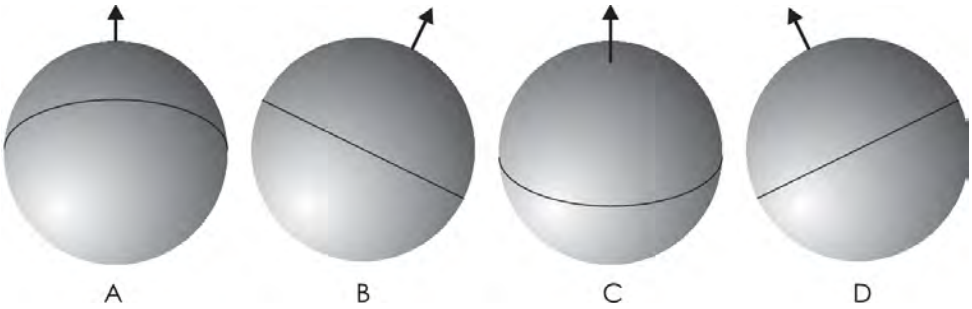

Figure 3.6: Orientation of the Sun's rotation vector as seen from Earth in terms of the angles defined in Figure 3.5. In A, $\gamma = -\delta$ and β=180°; in B, γ=0° and β=270°; in C, γ=+δ and β=0°; and in D, γ=0° and β=90°.

$$\cos\beta = \cot\delta\tan\gamma \tag{3.1}$$

As mentioned in the previous paragraph, a standard program was used to calculate γ and a simple approximation that is accurate to within a few tenths of a degree, requiring the date as a decimal year to calculate, may also be used (Burger 2014, personal communication)

$$\gamma = \delta \sin\left(2\pi \cdot \mathbf{decimalyear} + 3.58\right), \tag{3.2}$$

where the argument of the sine function is in radians. The output from the program (given in `http://users.telenet.be/j.janssens/Engobserveren.html#Solcoord`) was com-

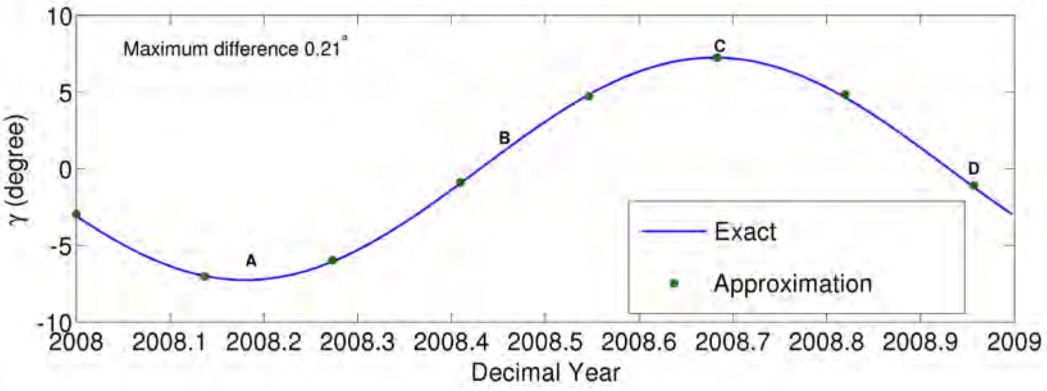

Figure 3.7: Comparison between exact and approximate value of γ. The maximum difference between the two values is 0.21°. The legends A to D (see Figure 3.6) indicate where the value of γ is maximum negative, zero, maximum positive and again zero, respectively.

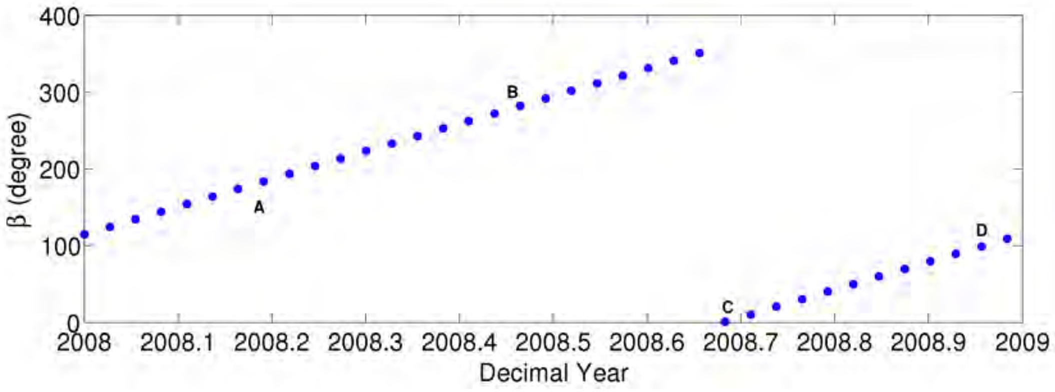

Figure 3.8: Angle β describes the rotation of the solar rotation vector as viewed from Earth. The legends A to D correspond to those in the previous two figures.

pared with the approximation and shown in Figure 3.7. This behaviour is close to sinusoidal and very similar over tens of years. The angle β's change over a period of a year is shown in Figure 3.8 and clearly changes linearly over time and the observer sees the vector rotation as clockwise. Note that this is just from the viewpoint of the observer: in reality the course of the rotation vector is fixed, and the observer moves around it in an anti-clockwise direction.

The rotation vector $\mathbf{\Omega}$ and unit vector $\mathbf{R}$ are expressed in GSE coordinates with unit vectors $\mathbf{e}_x, \mathbf{e}_y$ and $\mathbf{e}_z$, as respectively, shown in Figure 3.9

$$\mathbf{\Omega} = \Omega \sin\delta \cos\beta \mathbf{e}_x + \Omega \sin\delta \sin\beta \mathbf{e}_y + \Omega \cos\delta \mathbf{e}_z \tag{3.3}$$

and

$$\mathbf{R} = -\cos\theta \cos\phi \mathbf{e}_x + \cos\theta \sin\phi \mathbf{e}_y + \sin\theta \mathbf{e}_z. \tag{3.4}$$

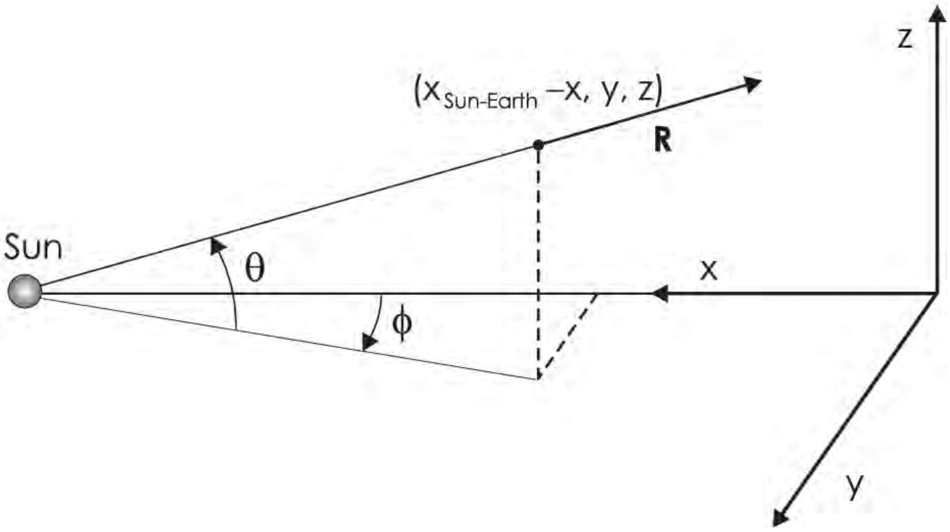

Figure 3.9: Definition of angles θ and ϕ in terms of GSE coordinates

To find the unit vector **T**, the normalised cross product of **Ω** and **R** is calculated, yielding

$$\mathbf{T} = \frac{\mathbf{\Omega} \times \mathbf{R}}{|\mathbf{\Omega} \times \mathbf{R}|} \tag{3.5}$$

which gives

$$\begin{aligned}\mathbf{T} = \frac{1}{M} & (\sin\delta \sin\beta \sin\theta - \cos\delta \cos\theta \sin\phi)\, \vec{e}_x \\ & + (\sin\delta \cos\beta \sin\theta - \cos\delta \cos\theta \cos\phi)\, \vec{e}_y \\ & + (\cos\theta \sin\delta \sin(\beta - \phi))\, \vec{e}_z\end{aligned} \tag{3.6}$$

where

$$M = \sqrt{\cos\delta^2 \cos^2\theta - \frac{1}{2}\cos(\beta - \phi)\sin 2\delta \sin 2\theta + \sin^2\delta \left[\sin^2\theta + \cos^2\theta \sin^2(\beta - \phi)\right]}. \tag{3.7}$$

The unit vector **N** that then completes the right-handed system is given by

$$\mathbf{N} = \mathbf{R} \times \mathbf{T} \tag{3.8}$$

which gives

$$\begin{aligned}
\mathbf{N} = \frac{1}{M} & \left(\cos\delta\cos\theta\cos\phi\sin\theta \right. \\
& - \cos\beta\sin\delta\sin^2\theta \\
& \left. \cos^2\theta\sin\delta\sin(\beta-\phi)\sin\phi\right)\vec{e}_x \\
& + \left(\sin\delta\sin\beta\sin^2\theta \right. \\
& \cos^2\theta\cos\phi\sin\delta\sin(\beta-\phi) \\
& \left. - \cos\delta\cos\theta\sin\theta\sin\phi\right)\vec{e}_y \\
& + \left(\cos\delta\cos^2\theta\cos^2\phi - \cos\beta\cos\theta\cos\phi\sin\delta\sin\theta \right. \\
& \left. - \cos\theta\sin\delta\ \ \sin\beta\sin\theta\sin\phi - \cos\delta\cos^2\theta\sin^2\phi\right)\vec{e}_z
\end{aligned} \tag{3.9}$$

For completeness, note that the angles θ and ϕ are related to GSE spatial coordinates x, y and z by

$$\begin{aligned}
\sin\theta &= \frac{z}{\sqrt{(x_{SE}-x)^2+y^2+z^2}},\ \cos\theta\frac{\sqrt{(x_{SE}-x)^2+y^2}}{\sqrt{(x_{SE}-x)^2+y^2+z^2}} \\
\sin\phi &= \frac{y}{\sqrt{(x_{SE}-x)^2+y^2}},\ \cos\phi\frac{x_{SE}-x}{\sqrt{(x_{SE}-x)^2+y^2}}
\end{aligned}$$

where x_{SE} is the Sun-Earth distance.

To find the R-component of the magnetic field, for example, in terms of given x, y and z components, one can use Expression 3.4 to find $B_R = -cos\theta\cos\phi B_x + \cos\theta\sin\phi B_y + \sin\theta B_z$

3.4 Constructing the second order structure function

The variance used in the current study is defined as [see, e.g., *Forsyth et al.*, 1996]

$$\sigma_N^2 = \frac{1}{n}\sum_{i=1}^{n}\left(B_{N_i} - \overline{B}_N\right)^2 \tag{3.10}$$

where B_N is the N-component of the magnetic field vector in the RTN coordinate system and n is the number of data points in the interval over which the variance is calculated. If the time resolution of the data used is say 1 minute, the number of data points therefore represent the lag in minutes over which the variance is calculated. The minimum lag used in this study is five minutes, that is n=5. The maximum lag was scaled with the length of the period over which an averaged second-order function is constructed. These periods, with the maximum lag in hours given in brackets, are: 27 days (80 hours), 54 days (160 hours), 189 days (320 hours), and 378 days (640 hours). For a lag corresponding to n data points, variances are calculated for data strings of length n, until the whole of the data set (27 days to 378 days) is covered. The strings are chosen to overlap such that the following string starts in the middle of the preceding string, to increase accuracy. The average value of the variances for all of these strings then yield the value of the second-order structure function for a lag of n minutes. The process is then repeated for lags n+1, n+2, n+3, ..., until the maximum lag chosen is reached. Turbulence quantities are then extracted from the resulting second-order structure functions, discussed in Section 3.5.

3.5 Motivation for choice of data resolution

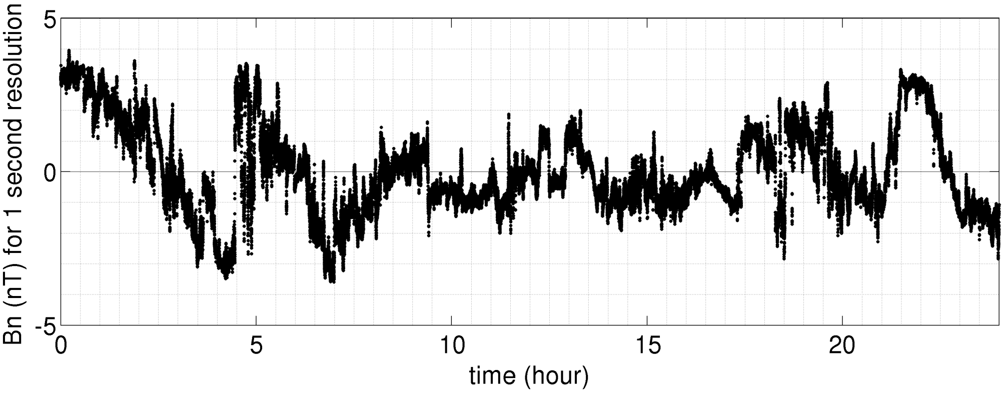

Figure 3.10: B_N component from *ACE* data, taken during day 71 in 2006, at 1 second resolution.

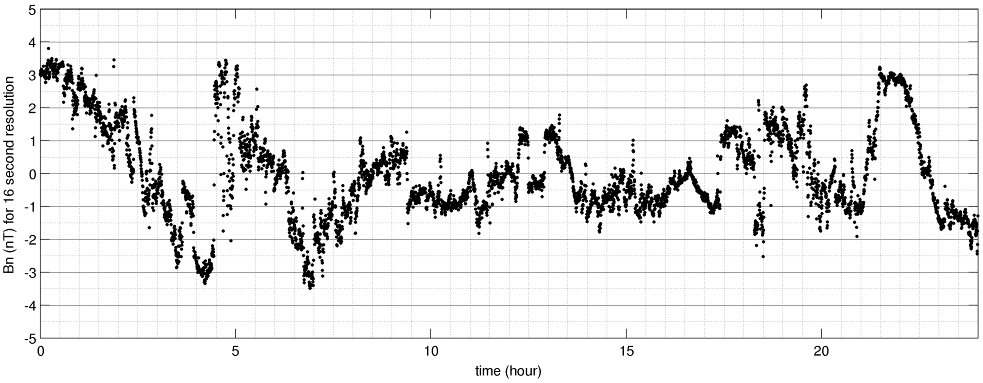

Figure 3.11: B_N component from *ACE* data, at 16 second resolution.

Matthaeus et al. [2012] show that the second-order structure function can be written as the difference between the total variance and a correlation function, the latter vanishing for sufficiently large lags. An accurate second-order structure function therefore requires an accurate value for the total variance. Level 2 *ACE* magnetometer data (see Section 3.2) ranges from 1 second to 1 hour resolution. The choice of the resolution of data to use would involve weighing the data processing speed against the loss of accuracy for lower resolution data. Evaluating one second data may take too long, so the most accurate resolution, without losing too much information, needs to be determined. To ensure that there is no bias, data were used in

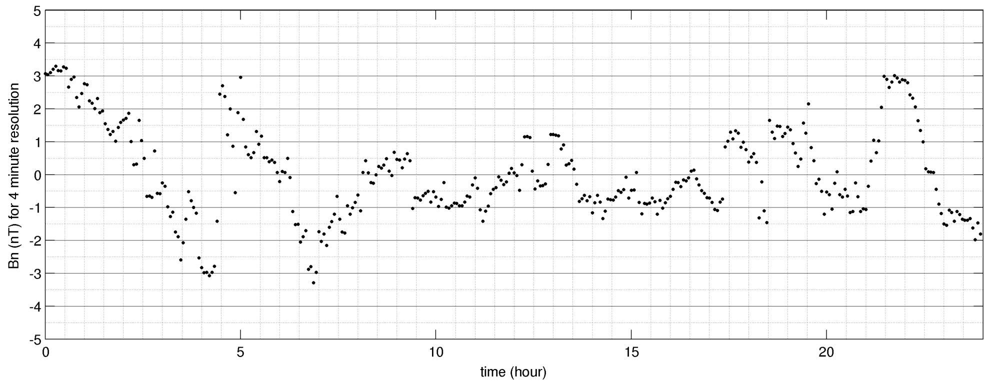

Figure 3.12: B_N component from *ACE* data, at 4 minute resolution.

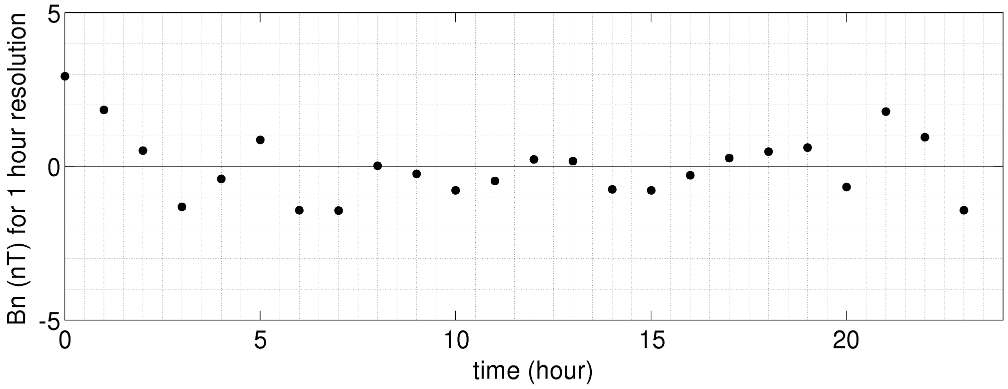

Figure 3.13: B_N component from *ACE* data, at 1 hour resolution.

the resolutions given on the website `http://www.srl.caltech.edu/ACE/ASC/level2/lvl2DATA_MAG.html` The B_N-components of resolutions at 1 second, 16 seconds, 4 minutes, and 1 hour are plotted and compared in Figures 3.10 - 3.13. It can be seen that there are significantly less fluctuations at lower resolutions. Next the variance for different lagtimes for all four resolutions was calculated and compared, as shown in Figure 3.14. From this graph, it seems that the different resolution data do follow the same trend, but the values are higher for higher resolution data. Therefore the use of hour-resolution data is not ideal, whereas the use of any of the other resolution data should not greatly affect the results reported. In particular, we expect one-minute resolution data is expected to yield variances within a few percent of 1-second resolution data. After weighing factors such as expected timescales for changes in the turbulence spectrum and processing time, it was decided to use 1-minute resolution data for this study.

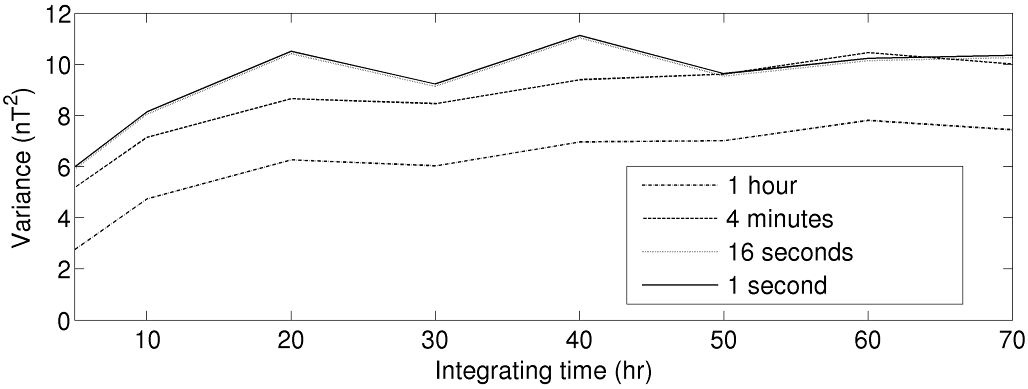

Figure 3.14: Comparing variance values for different resolution *ACE* data

3.6 Choice of underlying turbulence spectrum

The second-order structure function can be seen as an integral over an underlying spectrum for different lags (or inverse frequency). An obvious requirement is that the spectrum has to yield a finite variance; this determines its behaviour at small frequency, i.e. at large lags. It was decided to use a piecewise continuous spectrum that consists of a series of power laws and therefore is easily integrable. The spectrum consists of three ranges (excluding the dissipation range): an inertial range, energy range, and a cutoff range at small frequencies. The latter has to our knowledge not yet been observed in heliospheric turbulence. It is included based on theoretical considerations (see *Matthaeus et al.* [2007]). The spectrum is given by

$$\epsilon(f) = C \begin{cases} f_2^k(\frac{f_1}{f_2})^e(\frac{f}{f_1})^p, f < f1, \\ f_2^k\left(\frac{f}{f_2}\right)^e, f_1 \leq f < f_2 \\ f^k, f \geq f_2 \end{cases} \tag{3.11}$$

where e, p and k are the spectral indices in the cutoff-, energy-, and inertial range, respectively. Furthermore, C is a constant and f_1 denotes the break between the cutoff- and the energy range, while f_2 denotes the break between the energy- and the inertial range. The form of this spectrum is shown in Figure 3.15.

This constructed energy spectrum can be compared to the power spectrum constructed by *Bieber et al.* [1994] which is in wavenumber, shown in Figure 3.16 and given by

$$P_{xx}(k_z) = 2\pi C\lambda(1 + k_z^2\lambda^2)^{-\frac{5}{6}} \tag{3.12}$$

where spectral indices are chosen to be consistent with spacecraft observations. For the constant C a value of 0.5 nT was chosen, and for λ value of 4.55×10^9 m [*Bieber et al.*, 1994]. This latter model spectrum is consistent with observed properties of interplanetary magnetic turbulence, and C and λ were chosen by *Bieber et al.* [1994] specifically to agree with observations. A

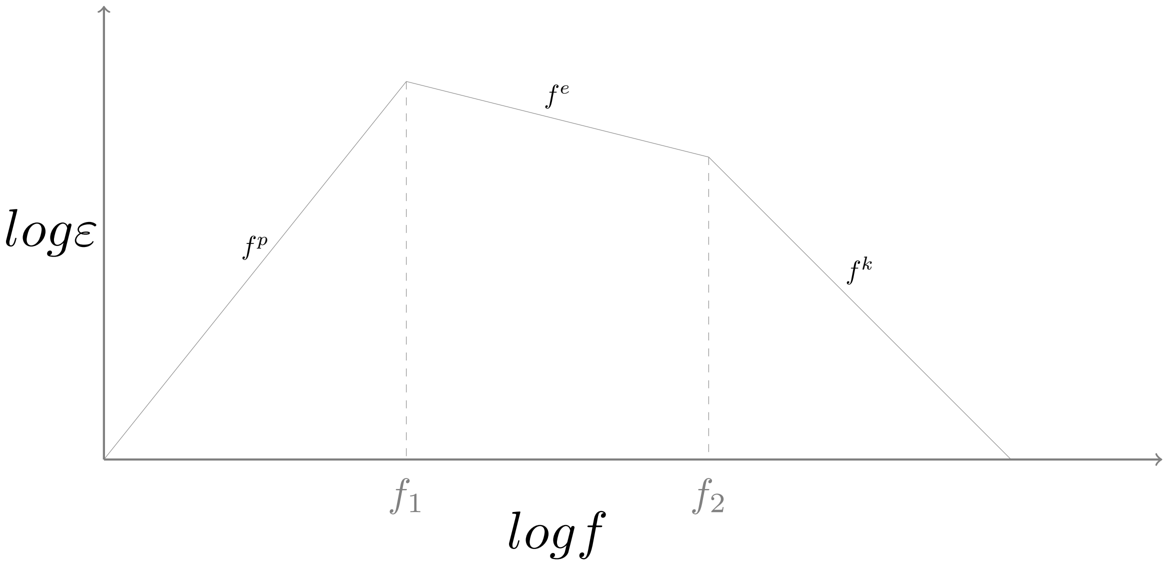

Figure 3.15: Form of the constructed energy spectrum used in this study.

dissipation range that occurs at high frequencies (typically beyond about 1 Hz at 1 AU) given by these authors is ignored. This is because the resolution of the data used in the current project is not high enough to resolve the dissipation range. This spectrum (including the dissipation range) is shown in Figure 3.16. The transition between the energy range and the inertial range is smooth, in contrast to the sharp break assumed in Equation 3.11. A spectrum that coincides with the one in Equation 3.11 at high and at low wavenumbers is easily constructed:

$$P_{xx}(k_z) = \begin{cases} 2\pi C\lambda^{-2/3}k^{-5/3}, k_z >= 1/\lambda \\ 2\pi C\lambda, k_z < 1/\lambda. \end{cases} \tag{3.13}$$

This spectrum is shown with the *Bieber et al.* [1994] spectrum in Figure 3.17. Clearly the area under the piecewise continuous function (which is related to the total variance) will be higher than that of the spectrum of these authors. In fact, the ratio of the areas can be written in terms of gamma functions as -5/6$1/\sqrt{\pi}\Gamma(-1/6)/\Gamma(1/3) = 1.189$. Note that this ratio is independent of λ and C. The question is whether observed spectra show a smooth or a sharp transition. Looking at observations such as those shown in Figure 2.13, it is certainly not clear what the case is. Given this uncertainty it is not unreasonable to assume sharp break, which has the benefits of simplifying further calculations. The second-order structure function can be constructed from the frequency spectrum (Equation 3.11) by integrating from high to low frequency:

$$\sigma(f) = C \begin{cases} \frac{{f_2}^k\left(\frac{f_1}{f_2}\right)^e\left(f_1 - f\left(\frac{f}{f_1}\right)^p\right)}{1+p} + \frac{C_2 {f_2}^k\left(f_2 - f_1\left(\frac{f_1}{f_2}\right)^e\right)}{1+e} - \frac{C_2 {f_2}^{1+k}}{1+k} & \text{for } f < f_1; \\ \frac{{f_2}^k\left(f_2 - f\left(\frac{f}{f_2}\right)^e\right)}{1+e} - \frac{C_2 {f_2}^{1+k}}{1+k} & \text{for } f_1 \le f < f_2; \\ -\frac{f^{1+k}}{1+k}, & \text{for } f \ge f_2 \end{cases}$$

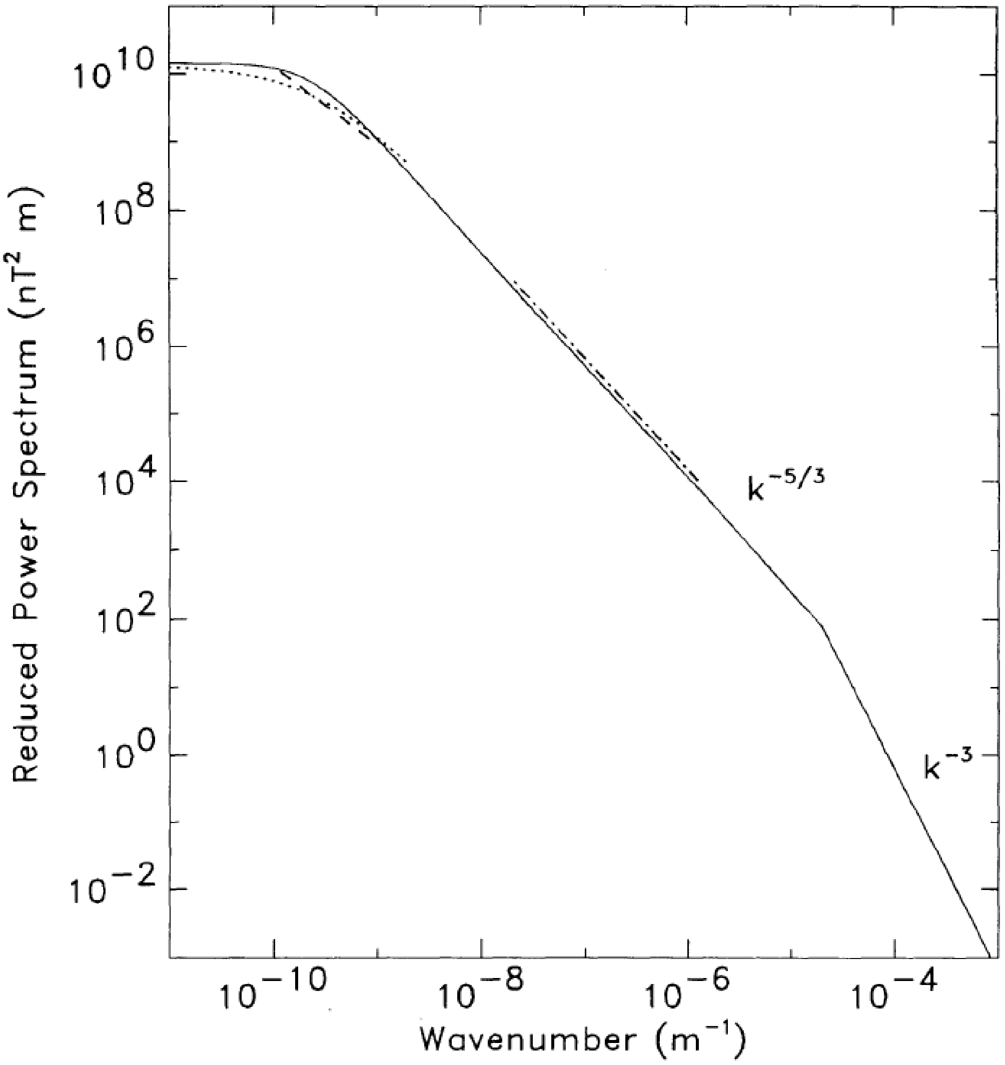

Figure 3.16: Power spectrum constructed by *Bieber et al.* [1994]. Here three ranges can be discerned. At low wavenumber the spectrum flattens out, signifying the energy-containing range. After that, at a lower spectral index of $-5/3$, the inertial range follows, and at high wavenumbers the dissipation range is seen, with a spectral index of -3.

Note that the frequency in this expression is the inverse of the lag time as defined in Section 3.5. First a single fit is done to the calculated variances from frequency f_2 to the highest frequency used in the analysis. which is considered to be the inertial range. From here, the spectral index k for the inertial range and constant C that was determined from this first fit is used in the next step, which is to do a fit, using a piecewise-continuous function. Parameters obtained for the first two fits are now used to fit the full three-range spectrum, and so to determined f_1 and the spectral index of the cutoff range. The latter was constrained to be either flat or decreasing with decreasing frequency in order to ensure a finite energy density.

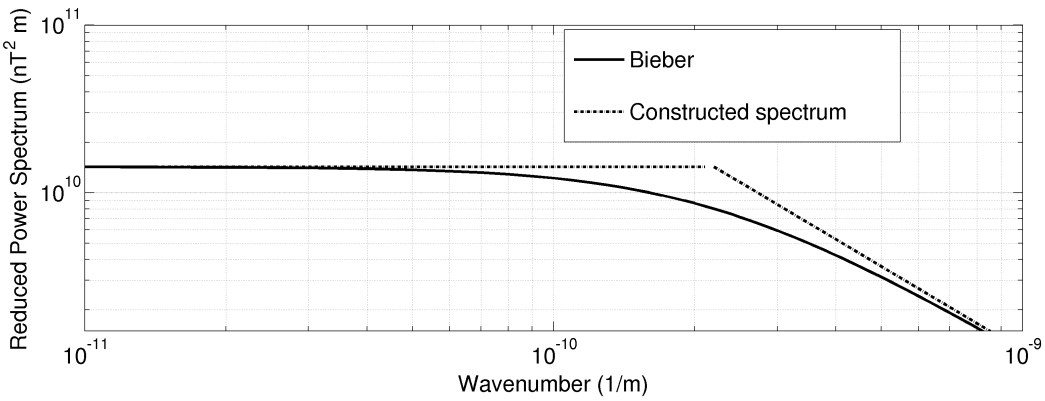

Figure 3.17: Comparing *Bieber et al.* [1994] power spectrum and the power spectrum constructed in this study. Two ranges can be discerned from the constructed spectrum, which at the highest and lowest wavenumbers shown overlaps the Bieber power spectrum.

3.7 Generating magnetic fields with a random fluctuating component

After deriving a method to fit the energy spectrum, a way of testing the turbulence quantities that followed from it was necessary. This was done by generating random data to mimic the random solar magnetic field data that would eventually be used for the purposes of this study. What follows is a generalisation of techniques described by *Decker and Vlahos* [1986] and *Decker* [1993] [R.A. Burger, private communication, 2014].

A plane polarized random fluctuating field $\delta B_x(z)$ must to be generated with a zero mean, i.e., $\langle \delta \mathbf{B}(z) \rangle = 0$. Say this field consists of N points in an interval of length L, with an even gridspacing h_b. The number of points specified as

$$N = 2^p, \; p \geq 0 \tag{3.14}$$

where p is an arbitrary value (in this study $p = 18$). At a particular point n the field is

$$\delta B_n \equiv \delta B\left(z = z_n \equiv n \cdot h_b\right), \; 0 \leq n \leq N - 1. \tag{3.15}$$

where the steps are in the z-direction. For example, the tenth point would be a distance of $z = 10\mathrm{h}_b$ from the origin. The turnover scale is the break between the energy and inertial range, and is located at

$$z_c = 2^q.h_b, 0 \leq q \leq p. \tag{3.16}$$

A typical value used for q in this study is 6. In *Decker and Vlahos* [1986] it is assumed that the correlation length z_c and the turnover scale of the turbulence spectrum are the same although this is not the case: These author‘s notation, however, will be used in what follows.

The finite Fourier transform for the random field δB consisting of N points on the interval $[0, L]$ is given by

$$a_m = \sum_{n=0}^{N-1} \delta B_n e^{-ik_m z_n},\ m = 0, 1, 2, \ldots, N-1 \tag{3.17}$$

where

$$k_m = \frac{2\pi}{\lambda_m} = \frac{2\pi m}{N h_b} \approx \frac{2\pi m}{L}, \tag{3.18}$$

which is the wavenumber corresponding to the wavelength λ_m associated with the Fourier coefficient a_m. The last part of the expression is valid if N is large, which is the case in this study.

The inverse Fourier transform of a$_m$ is given by

$$\delta B_n = \frac{1}{N} \sum_{m=0}^{N-1} a_m e^{ik_m z_n},\ n\ =\ 0, 1, 2, \ldots, N-1. \tag{3.19}$$

Note that $a_0 = 0$ because we assume that the mean of the field is zero. In the interval of length L, the largest possible wavelength (smallest wavenumber) that fits in it is defined by

$$k_1 = \frac{2\pi}{N h_b} \approx \frac{2\pi}{L} \tag{3.20}$$

where N is large enough so that $N \approx N-1$. Now as m is increased (see Equation 3.18), the wavelength becomes shorter and more waves fit into the interval of length L. The Nyquist wavenumber is defined as the largest wavenumber for a gridspacing h_b, so that

$$k_{N/2} = \frac{\pi}{n_b}. \tag{3.21}$$

From Equation 3.21 one can see that the shortest wavelength that can usefully be defined, covers two gridspacings.

The power per wavenumber interval Δk of mode m can be estimated as

$$P_m \approx \frac{2}{\Delta k} \frac{h_b}{L} \sum_{n=0}^{N-1} \delta B_n \frac{h_b}{L} \sum_{n=0}^{N-1} \delta B_n \approx \frac{2}{\Delta k} \left(\frac{h_b}{L}\right)^2 |a_m|^2 = \frac{2L}{2\pi} \left(\frac{h_b}{L}\right)^2 |a_m|^2 = \frac{{h_b}^2 \, |a_m|^2}{L\pi}. \tag{3.22}$$

Note the factor 2 in the first term on the right-hand side, which arises from the assumption of a one-sided spectrum, defined for positive wavenumbers only. The phases for the different modes m need to be random, so a new factor is introduced such that

$$a_m = |a_m|\, e^{i\phi_m}, \tag{3.23}$$

where ϕ_m is a random angle for mode m. It then follows that

$$a_m = |a_m|\, e^{i\phi} = \left(\frac{L\pi P_m}{{h_b}^2}\right)^{\frac{1}{2}} e^{i\phi_m} = \left(\frac{\pi P_m N^2}{L}\right)^{\frac{1}{2}} e^{i\phi_m} = N\left(\frac{\pi P_m}{L}\right)^{\frac{1}{2}} e^{i\phi_m}. \tag{3.24}$$

We assume that the δB_n defined in Equation 3.19 are real. Then this quantity is equal to its complex conjugate, so that

$$\delta B_n \equiv \delta B_n^* = \frac{1}{N}\sum_{m=0}^{N-1} a_m^* e^{-ik_m z_n}. \tag{3.25}$$

It follows from Equation 3.24 that

$$a_m^* = N\left(\frac{\pi P_m}{L}\right)^{\frac{1}{2}} e^{i\phi_m}. \tag{3.26}$$

Combining Equations 3.25 and 3.26 yields

$$\delta B_n = \sum_{m=0}^{N-1}\left(\frac{\pi P_m}{L}\right)^{\frac{1}{2}} e^{-i\phi_m} e^{-ik_m z_n} \equiv \sum_{m=0}^{N-1} A_m e^{-ik_m z_n} \tag{3.27}$$

where A_m is defined as

$$A_m = \left(\frac{\pi P_m}{L}\right)^{\frac{1}{2}} e^{-i\phi_m}. \tag{3.28}$$

This procedure therefore leads to a representation where δB_n can be written as the Fourier transform of A_m. Since the former is real, the latter is hermitian such that [*Bracewell*, 2000]

$$A_{N-m} = A_m^*,\ m = 1.2.3.\ldots, \frac{N}{2} - 1 \tag{3.29}$$

The latter condition follows from the hermitian property that the real part of A_m even and the imaginary part is odd with respect to the midpoint of the interval. We set $A_0 = 0$ to ensure a zero mean for the δB_n. Since only half of the A_m are independent, we can rewrite Equation 3.27 as

$$\delta B_n = 2\sum_{m=0}^{\frac{N}{2}-1} A_m e^{-ik_m z_n} \tag{3.30}$$

This expression can be written as simply a sum of cosine or sine terms, as in *Decker* [1993]. However, this procedure is computationally expensive, and a much faster option is to use a fast Fourier transform. Because the magnitude of the real and the imaginary parts of A_m are the same, we have that

$$\delta B_n = 2 \cdot Re\left[\mathbf{FFT}(A_m)\right] \; or \; 2 \cdot Im\left[\mathbf{FFT}(A_m)\right] \tag{3.31}$$

It remains to specify a suitably normalised power spectrum in order to evaluate the term $\sqrt{\frac{\pi P_m}{L}}$ in 3.28. Assume that

$$P(k_m) = P_m = \frac{C\sigma^2}{S\left(k_m \frac{z_{c,j}}{2\pi}\right)} \tag{3.32}$$

where the $z_{c,j}$ are j characteristic spatial scales. Note that the term omnidirectional energy spectrum is used by some authors [see, e.g., *Matthaeus et al.*, 2007] for the power spectrum. Here, $S\left(k_m \frac{z_{c,j}}{2\pi}\right)$ is an arbitrary function of its argument. Note that this form of the argument differs from that used by *Decker and Vlahos* [1986] and *Decker* [1993] by a factor of 2π. The current form is preferred if one deals with length scales and frequencies rather than wavenumbers. Following *Matthaeus et al.* [2007], we normalize P_m such that

$$\int_{k_1}^{k_{N-1}} P_m \mathrm{d}k \; = \; \delta B^2 \; \equiv \sigma^2 \tag{3.33}$$

To discretize the expression, note that from Equation 3.18, $\Delta k = 2\pi/L$, so that

$$\frac{2\pi}{L} \sum_{m}^{N-1} P_m = \sigma^2 \tag{3.34}$$

The factor 2π is to ensure that the correlation function at zero lag is the root mean square value of the random magnetic field [*Decker and Vlahos*, 1986]. Substituting Equation 3.34 into 3.32 we can solve for the factor C,

$$C = \frac{L}{2\pi} / \sum_{m}^{N-1} \frac{1}{S\left(k_m \frac{z_{c,i}}{2\pi}\right)} \equiv \frac{L}{2\pi C_{sum}} \tag{3.35}$$

where

$$C_{sum} = \sum_{m}^{N-1} \frac{1}{S\left(k_m \frac{z_{c,i}}{2\pi}\right)}. \tag{3.36}$$

The power spectrum can therefore be recast as

$$P(k_m) = \frac{L}{2\pi C_{sum}} \frac{\sigma^2}{S\left(k_m \frac{z_{c,i}}{2\pi}\right)} \tag{3.37}$$

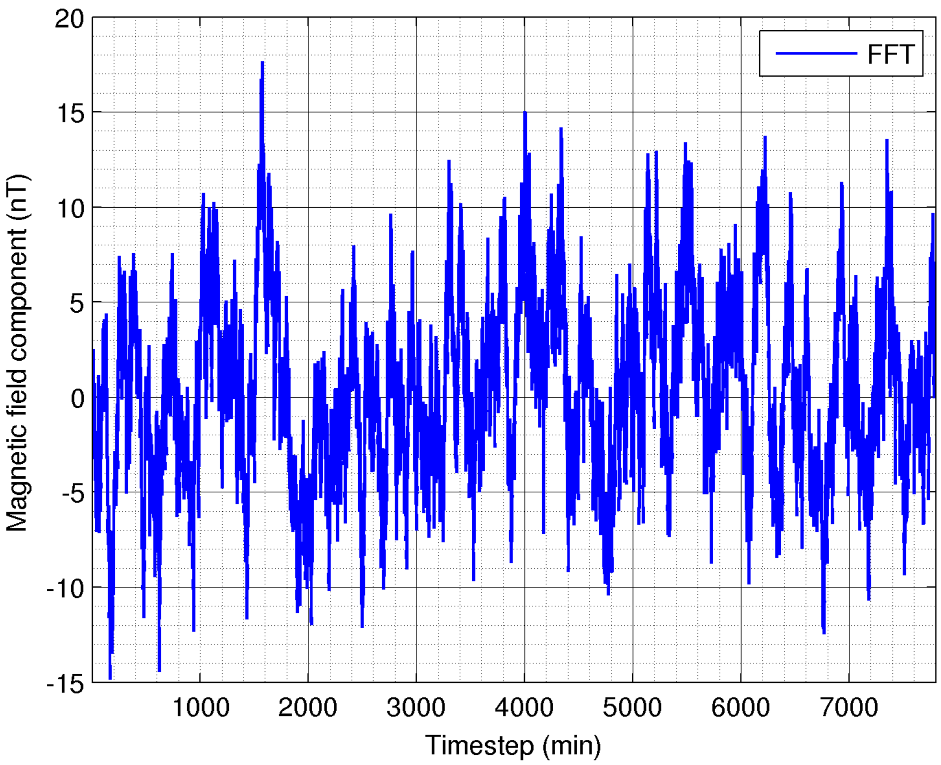

Figure 3.18: Synthetic dataset generated following the approach of *Decker* [1993]. See text for more detail.

and Equation 3.28 as

$$A_m = \frac{\sigma}{\sqrt{2C_m S\left(k_m \frac{z_m}{2\pi}\right)}} e^{-i\phi_m}. \tag{3.38}$$

Turning now to the data to be generated, we note that the spatial intervals h_b can be converted to time intervals by assuming frozen-in flow. The flow speed is simply

$$V = \frac{h_b}{t_b}, \tag{3.39}$$

with t_b the time it takes for a spatial structure with length h_b to be convected past a stationary observer, or equivalently, the time-resolution of the data. Using the relation

$$kV = \omega = 2\pi f \tag{3.40}$$

leads to

$$f = \frac{kV}{2\pi} = \frac{kh_b}{2\pi t_b}. \tag{3.41}$$

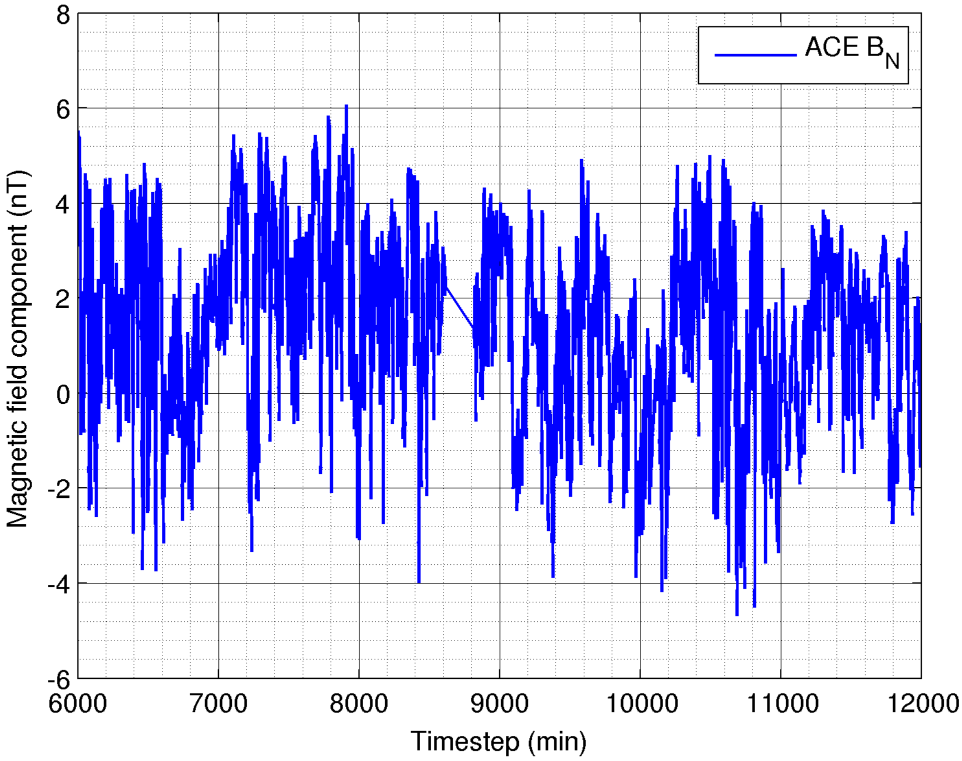

Figure 3.19: Excerpt from *ACE* B_N data. Note the similarity to generated data as in Figure 3.18.

Therefore, to convert the wavenumber spectrum to a frequency spectrum, one has to multiply Equation 3.37 by $2\pi t_b/h_b$ to convert from energy per wavenumber to energy per Hz. Moreover, a given spatial scale z_c is readily converted to a time scale t_c, using

$$z_c = V \cdot t_c = \frac{h_b}{t_b} t_c \Rightarrow t_c = 2^q \cdot t_b, 0 \leq q \leq p \tag{3.42}$$

The function $S\left(k_m \frac{z_{c,j}}{2\pi}\right)$ now becomes $S\left(f_m t_{c,j}\right)$ using Equations 3.39, 3.40, 3.41 and 3.42. Note that for mode number m we have that $k_m \frac{z_{c,j}}{2\pi} \equiv f_m t_{c,j} \equiv m \frac{z_{c,j}}{L} \equiv m \frac{t_{c,j}}{N t_b}$.

The power spectrum then becomes

$$P(f_m) = \frac{L t_b}{C_{sum} h_b} \frac{\sigma^2}{S\left(f_m t_{c,i}\right)} \tag{3.43}$$

One should also bear in mind that when using Fourier transforms, the power spectrum is given in energy per $(1/t_b)$ Hz, and the result has to be multiplied by t_b for the units to be the same as for Equation 3.43. For the purposes of comparison, an example of the resulting generated magnetic field is shown in Figure 3.18, and an excerpt from *ACE* data (B_N component) in Figure 3.19. Note the similarity of the fluctuations.

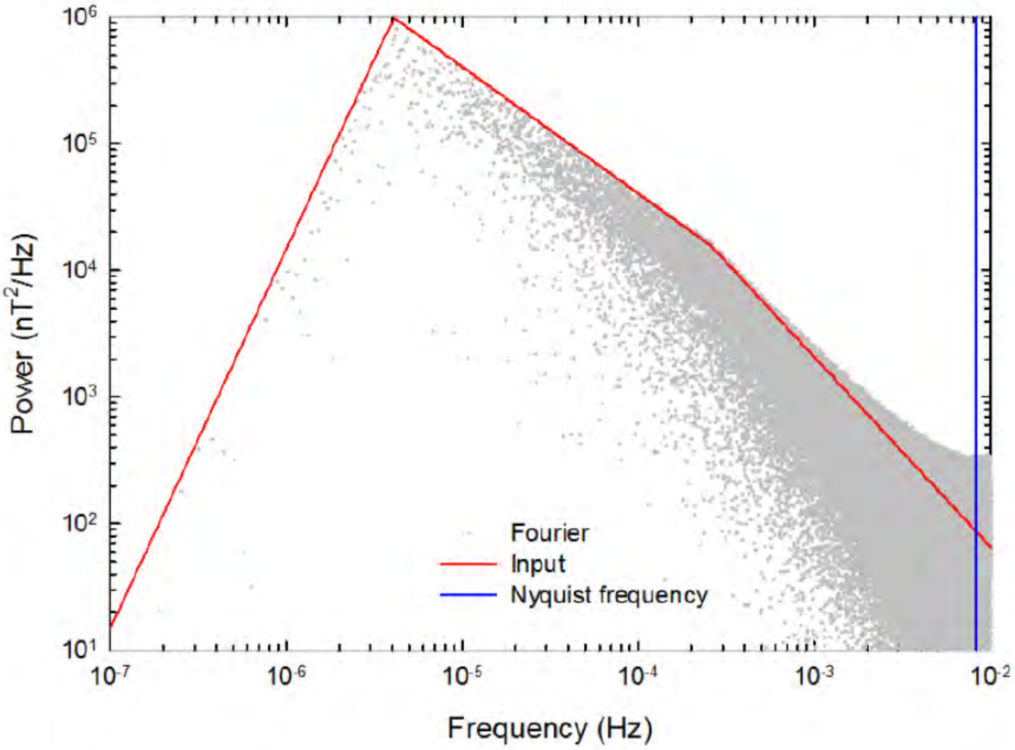

Figure 3.20: Power spectrum computed by a Fourier transform compared with input spectrum [Burger private communication 2014].

3.8 Benchmarking the fitting procedure

The standard way to calculate turbulence quantities from magnetic-field data is to do a Fourier analysis. An example of a Fourier spectrum constructed from synthetic magnetic field data (see Section 3.7) is shown in Figure 3.20. Also shown is the input spectrum used to generate the data. No filter was used, and this spectrum differs significantly from examples where techniques such as pre-whitening and post-darkening were used [see, e.g., *Bieber et al.*, 1993]. A low-pass filter would change the shape of the spectrum at high frequencies, which is clearly different from the input spectrum in the example shown in this figure. The second-order structure function on the other hand, gives a very "clean" result. This is shown in Figure 3.21, for a similar data set of synthetic data as was used for Figure 3.20. The question now is how accurate the second-order structure function technique is. To answer this, two aspects are considered: how accurately can a given input spectrum be reproduced, and what the effect is of data omissions. The references in Section 2.10 give a good idea of what typical values for the known turbulence quantities are, and these are taken into account. A standard (one-sided) frequency spectrum is chosen that has a Kolmogorov $-5/3$ inertial range spectral index, a -1 energy range spectral index, and a +3 cutoff range spectral index; turnover scale of 64 minutes and a cutoff scale 64 times larger, i.e. 68.3 hours, and a variance of 25 nT^2. The actual value of the variance proved to have negligible effect on the results. To test the accuracy, the spectral

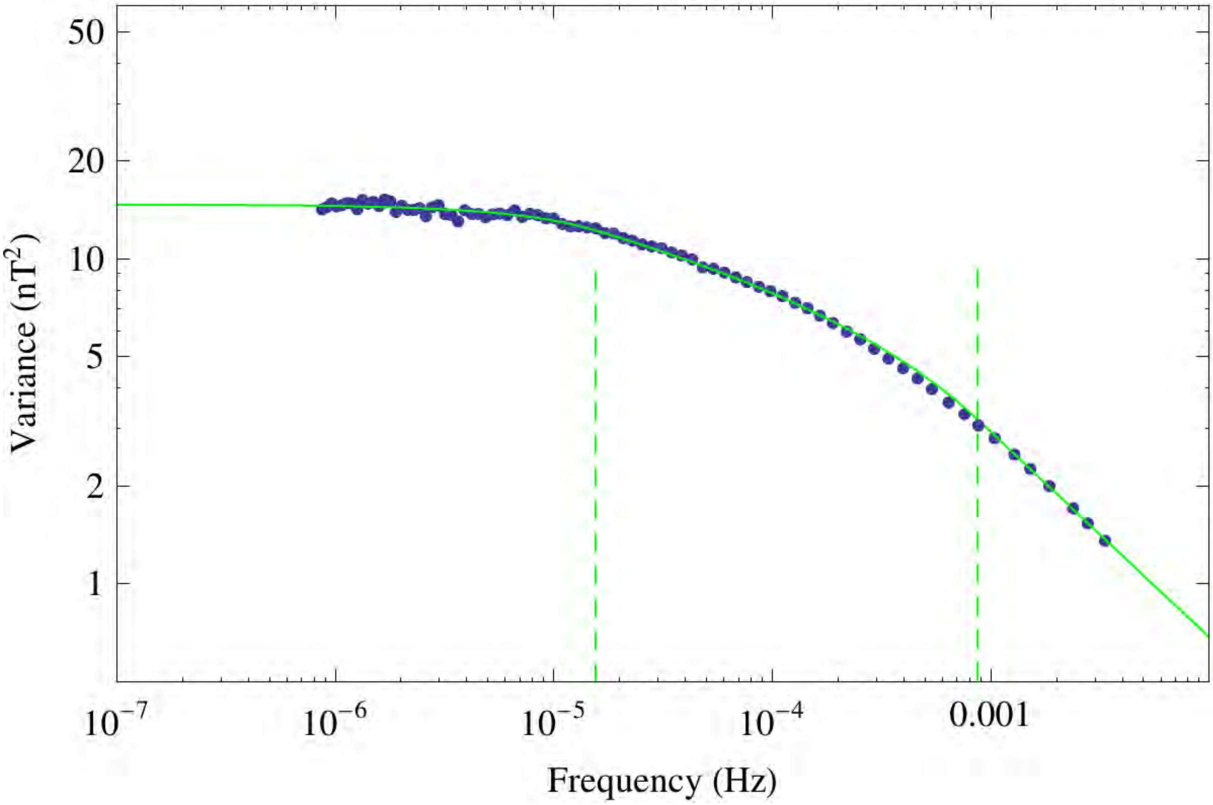

Figure 3.21: Example of a three-stage fit done over calculated variance data. The vertical dashed line at 2×10^{-5}Hz shows the transition from the energy-containing range to the outer range at lower frequencies. The vertical dashed line at $\sim9\times10^{-4}$Hz shows the transition from the inertial range to the energy-containing range at lower frequencies. Note the smooth slope of points in the inertial and energy-containing range, compared to the more disorganised points in the outer range.

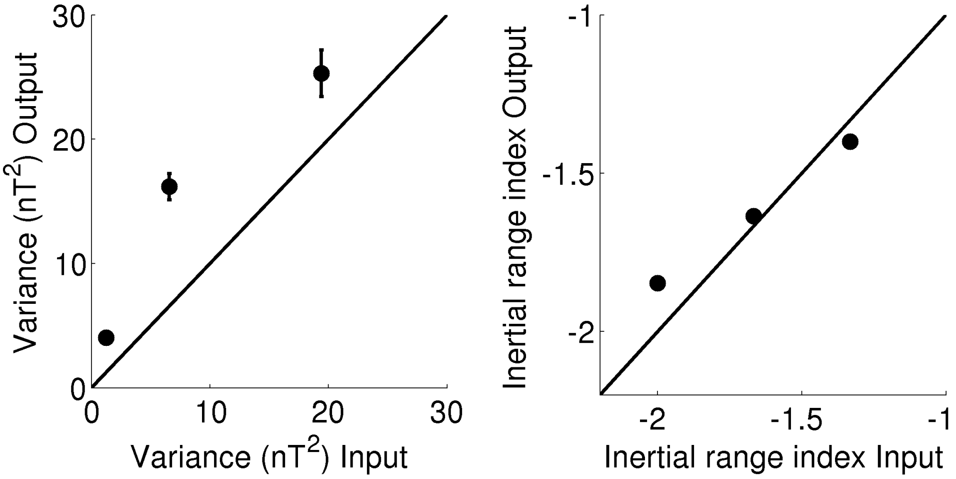

(a) Variance over range tested.

(b) Inertial range spectral index over range tested.

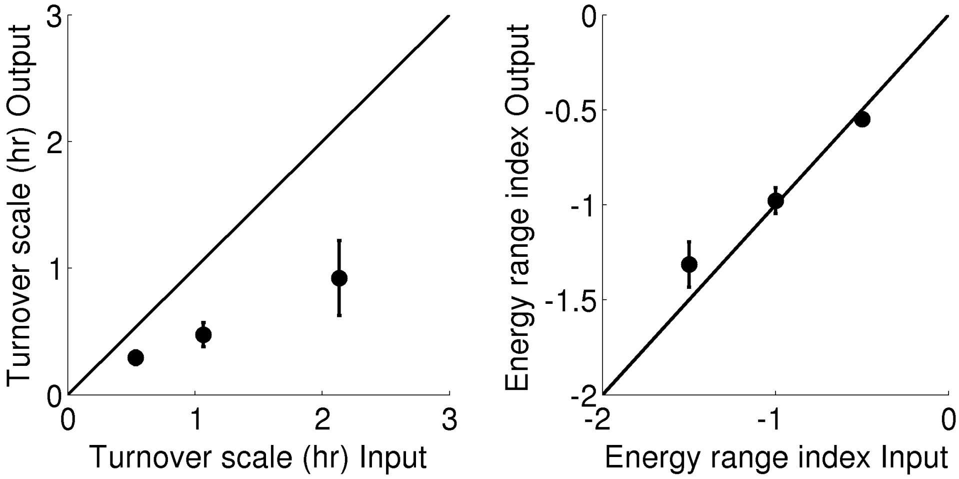

(c) Turnover scale over range tested.

(d) Energy range spectral index over range tested.

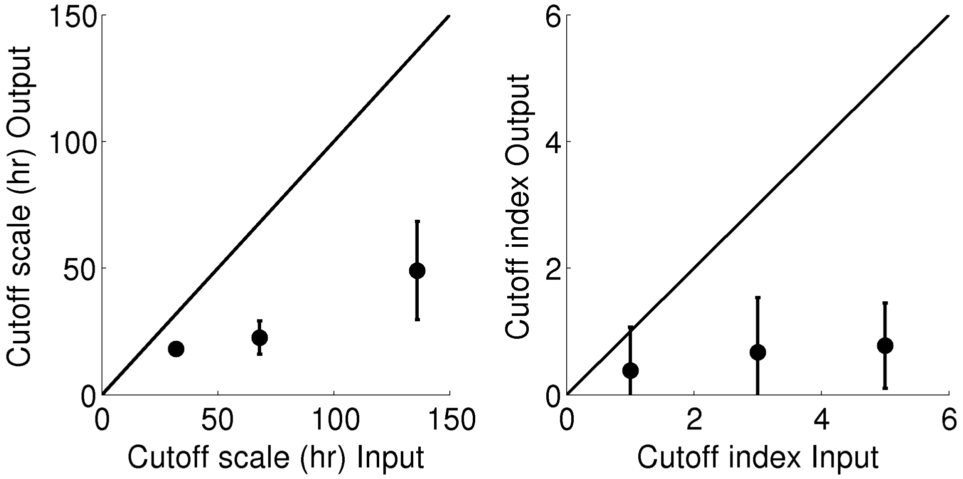

(e) Cutoff scale over range tested.

(f) Cutoff scale index over range tested.

Figure 3.22: Inputs versus outputs of various turbulence quantities.

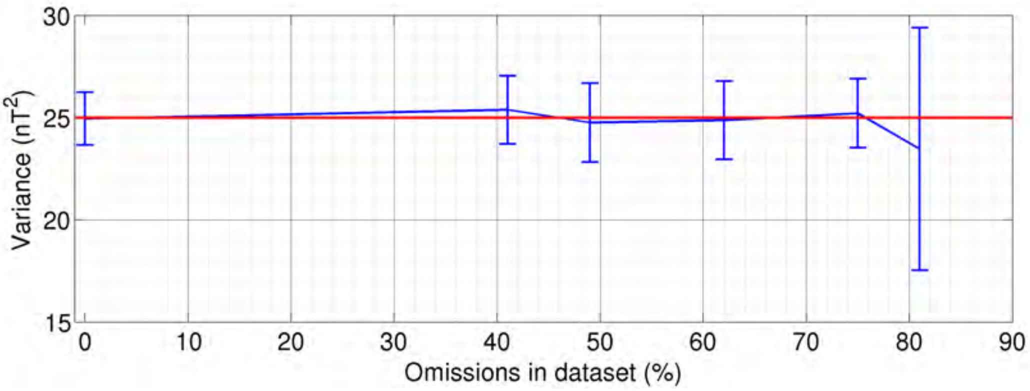

Figure 3.23: Change in variance with different percentage omissions, where the original input was 25 nT^2.

index for the inertial range was varied between $-4/3$ and -2, the energy range index between -0.5 and -1.5, the cutoff range between +1 and +5, the turnover scale between 32 minutes and 128 minutes and the variance between 4 and 25 nT^2. Twenty six runs were performed for each set of variables and the average and standard deviation determined. Figure 3.22a shows the variance over the range tested. The difference between input and output values increases from 0.2% to 2% as the input increases from 4 to 25 nT^2. These differences are smaller than the standard deviation at each point. This technique can clearly resolve the variance very well, provided that the second-order structure function approaches a constant value. The output for the inertial range spectral index in Figure 3.22b is smaller than the output by 5% for an input of -1.33, and larger by 8% for an input of -2. If the real index of the spectrum is close to the Kolomogorov $-5/3$ value, one can expect a very accurate result. Figure 3.22c shows that this technique underestimates the turnover scale by a factor of about 2 for all three input values considered. The reason for this is not clear. In Figure 3.22d, the output for the energy range spectral index is 10% smaller than the output for an input of -0.5, and larger by 12% for an input of -1.5. If the real index of the spectrum is close to -1, one can expect a very accurate result in this case as well. Similar to the turnover scale in 3.22b, the technique also underestimates the cutoff scale shown in Figure 3.22e, by somewhat more than a factor of two. It is clear that the output for the spectral index in the cutoff range is independent of the input, and one cannot get any useful information about this parameter using this method. Given the uncertainties in the parameters related to the cutoff range, they are not considered when the effects of data omissions are investigated in what follows.

To get a realistic idea of the effect of omissions on output values, omissions in simulated data first had to resemble the pattern of omissions in spacecraft datasets. Numerous sets of 27-day, 1-minute resolution *ACE* data were taken, and the omissions present in those datasets were exactly duplicated onto six previously generated datasets with specific input turbulence quantities. The percentage omissions were noted for each of the six datasets, which finally consisted of 0%, 41%, 49%, 62%, 75% and 81% omissions. After calculating the output turbulence

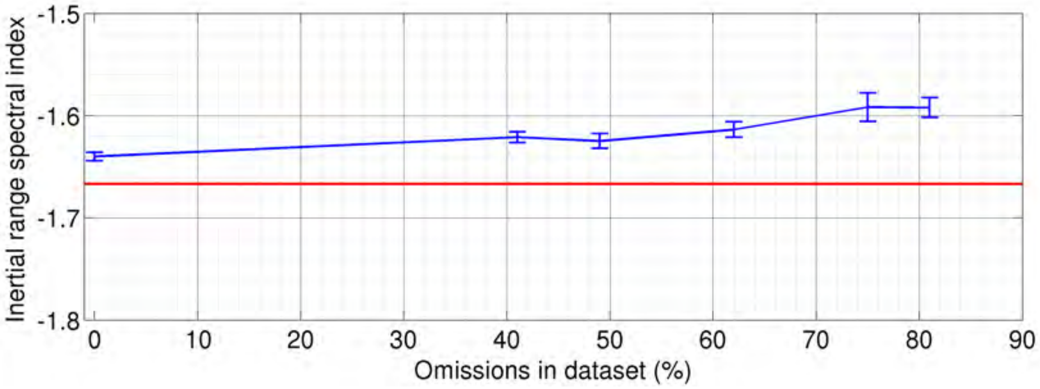

Figure 3.24: Change in inertial range spectral index with different percentage omissions, where the original input was −1.67.

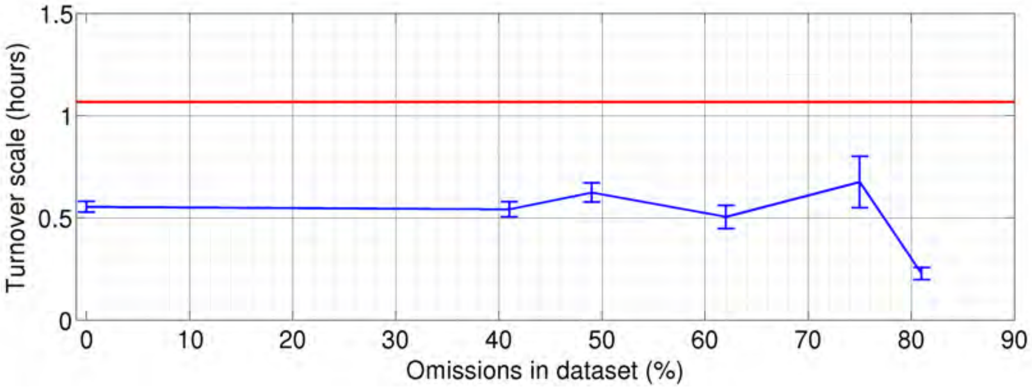

Figure 3.25: Change in turnover scale value with different percentage omissions, where the original input was 1.07 hours.

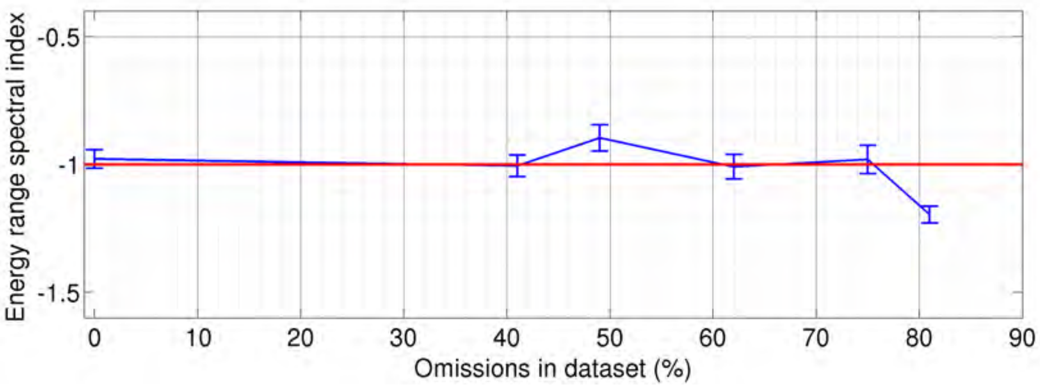

Figure 3.26: Change in energy range spectral index with different percentage omissions, where the original input was −1.

quantities, an average was taken for each omission-set. The resulting values for the turbulence quantities are shown in Figures 3.23, 3.24, 3.25 and 3.26. By taking the standard deviation for each set, error bars could be included in the figures.

Figure 3.23 shows the change in variance as the amount of omissions are increased. A value of 25 nT^2 is given as input for the *Decker* [1993] model. One can see the output, as calculated by the fit method, is just slightly above 25 nT^2. There is then a slight decrease in this value for higher percentage omissions, followed by a sharp decrease (from 23nT^2 to 20nT^2) at 81% omissions. It is clear that, when determining the variance value, datasets with omissions higher than 75% cannot be considered. Figure 3.24 shows the inertial range index for different percentage omissions. As input, a Kolomogorov inertial range was assumed (see Section 2.10) which is a wavenumber dependency of $k^{-1.67}$. The indices stay roughly between -1.65 and 1.6. The output here differs from Figure 3.23 because there is no sharp decrease in value at the higher percentage omissions. For Figure 3.25, an input value of 64 minutes (1.06 hours) was chosen. The output values at the lower percentage omission range fluctuates around 1.5 hours, then jumps to 2.5 hours before a sharp decline to 0.2 hours. Lastly, Figure 3.26 shows the energy range spectral index, with an input of -1. The output stays between -1.5 and -1 until around 60% omissions, where it first sharply increases then decreases to around -1.5 for 81% data omissions.

Because of the effect omissions can have on the results, values calculated with data omissions of over 75% are omitted in results.

3.9 Summary and conclusion

To determine the solar cycle dependence of various turbulence quantities, *ACE* and *IMP* data were chosen to be analysed as these datasets span over several solar cycles. To determine the neccessary turbulence quantities the relevant magnetic field component B_N from the RTN coordinate system was transformed from the GSE coordinate system by constructing a transformation matrix. Next a second order structure function was constructed, from observationally and theoretically motivated form for the turbulence power spectrum, the whole spectrum, which will be used to fit variances calculated from the abovementioned spacecraft data. This method was first tested by generating a random magnetic field with fluctuating components, and a good agreement was found between most input and output values. The effect of data omissions was also tested, and it was found that omissions of more than 75% tended to lead to inaccurate results. The method constructed in this chapter will applied to the analysis of spacecraft data in the next chapter.

Chapter 4

Analysis of IMP and ACE data

4.1 Introduction

The results that were acquired after the application of the data analysis technique to 38 years of *IMP* and *ACE* data are presented in this chapter. In the first section variances for different period-lengths are shown and discussed in detail, and comparisons are made with the observed behaviour of the HMF. Afterwards, other turbulence quantities will be calculated, presented and compared with observations.

4.2 Second-order structure functions at different levels of solar activity

A panel of figures which are examples of second-order structure functions for the 27-day datasets at solar minimum, maximum and at intermediate times are shown in Figures 4.1a-4.1f. Figures 4.1a and 4.1b show the second-order structure function at solar minimum, for ∼March 1986 and ∼June 1996 respectively. Figures 4.1c and 4.1d show examples at intermediate times (moving towards a solar maximum or towards a solar minimum), for ∼May 1998 and ∼June 2004 respectively. The bottom panel shows examples of spectra during solar maximum at ∼May 1980 and ∼May 1990. The maximum lag is 80 hours, corresponding to a frequency of 3.47×10^{-6} Hz. Note that there is a clear difference between solar minimum and solar maximum times: both second-order structure functions for solar minimum times are much lower than during solar maximum. Results for the intermediate times vary, and no clear conclusion can be made for them. Note too that some second-order structure functions (for example 4.1d) seem to rise indefinitely, but the method used in this study forces the fit for the integrated energy spectrum to flatten out, seeing as the underlying energy spectrum was constructed to ensure a finite value for the total magnetic variance (see the next section). At lower frequencies, data tend to be more scattered during solar maximum times.

Similar to the previous figures, Figures 4.2a-4.2f show different intergrated energy spectra for 378-day datasets. In this case the maximum lag is 640 hours, corresponding to a frequency of

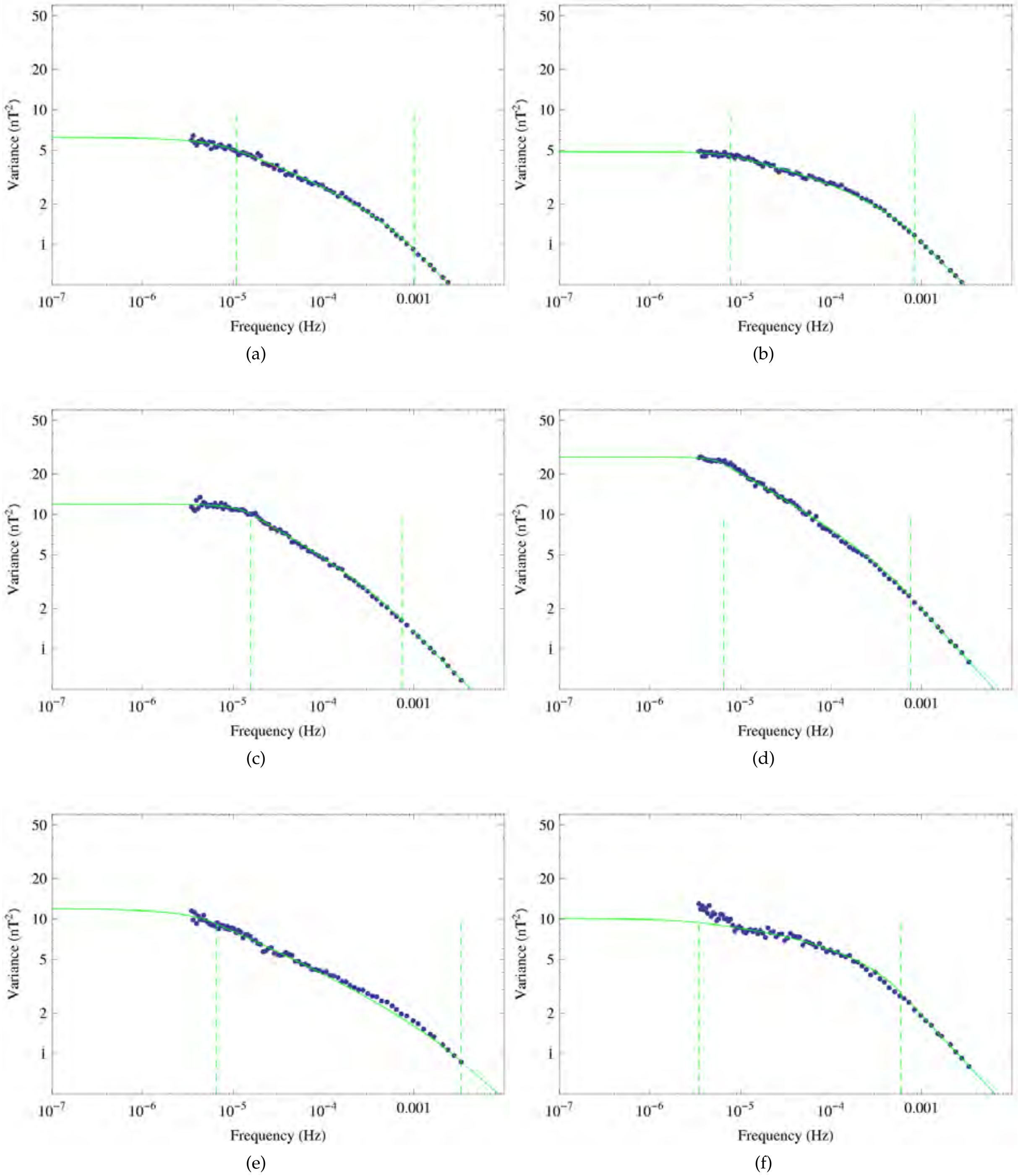

(a) (b) (c) (d) (e) (f)

Figure 4.1: Second order structure functions for 27-day datasets.

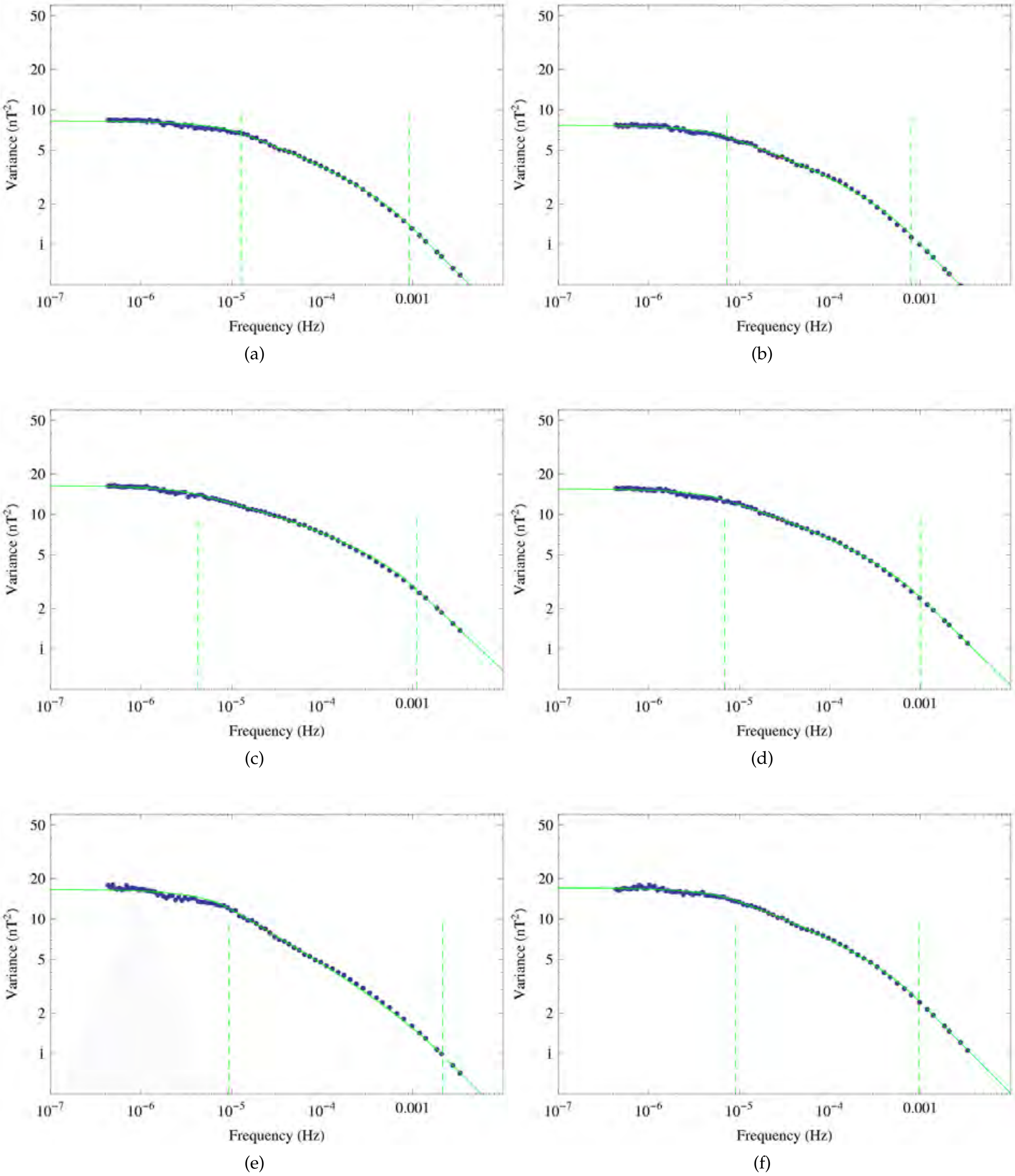

(a) (b)

(c) (d)

(e) (f)

Figure 4.2: Second order structure functions for 378-day datasets.

4.34×10^{-7} Hz. Figures 4.2a and 4.2b are examples of second-order structure functions at solar minimum for the years 1986 and 1996 respectively. Figures 4.2c and 4.2d are for intermediate times, the years 1983 and 1988. The last two Figures (4.2e and 4.2f) are for solar maximum times: 1980 and 1990. Here too a lower spectrum can be seen at minimum times, compared to maximum times.

It is clear when looking at the 27-day set and 378-day set that a smoother, more aligned spectrum is seen for the latter dataset. For the 27-day set the datapoints tend to be more scattered, with 'bumps' throughout. The reason for this is that, from month to month, various physical occurrences happen which are picked up in the spectrum. But by taking a spectrum over the whole year, these occurrences are averaged out.

4.3 Magnetic Variance

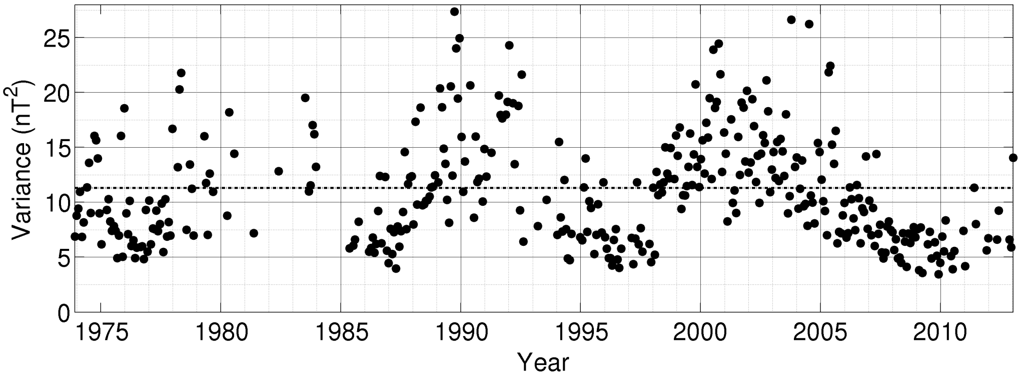

Figure 4.3: Variance calculated over 27-day periods, using data spanning over 38 years. A possible solar cycle dependency can be seen, with three peaks visible during times of high solar activity. The dashed line represents the average taken over all points, which is 11 nT^2.

One minute resolution data from *IMP* and *ACE* over a period of ~38 years are analysed, and the length in days of the data strings into which the complete data set is to be subdivided into is first chosen to be 27 days. This method was described in Section 3.4. The maximum lagtime, i.e. the longest time over which the variance is calculated, was chosen to be significantly less than the length of the dataset. In the case of 27 days, a maximum lagtime of 80 hours was chosen. If any period had a data gap that totaled more than 75% of the period, that datapoint is not shown or used in subsequent calculations (see Section 2.8). The magnetic variance obtained from the second-order structure function for each 27-day dataset, is shown in Figure 4.3 from 1973 to 2012. An average of ~11nT^2 was found over the whole period. Note the lack of data during ~1980 to ~1985, the clustering of datapoints at the lower levels, and the larger scatter of points at the higher levels. During the time of the most recent solar minimum, the variance values were at their lowest, compared to the whole period over which observations were made. Also note a clear solar cycle dependence, with two peaks (maxima) visible at

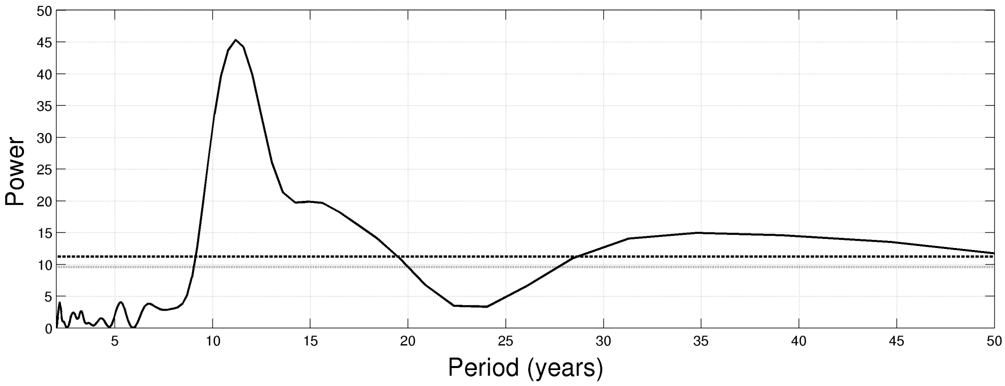

Figure 4.4: Lomb periodogram for the variance calculated over 27-day periods, taken over more than 38 years. The most significant peak is at 11.2 years. A second peak on its left shoulder is at ~15 years and a third peak is visible at ~35 years. The dashed line indicates the 99% significance level, and the dotted line indicates the 95% significance level.

~1990 and ~2001, which were times of higher solar activity. The third peak in the late 70's is less obvious, as there were more data gaps during that period. Larger values are seen during periods of increasing solar activity, and smaller values during solar minima. An obvious question that arises is whether the solar-cycle dependence that can be seen are indeed statistically significant. Therefore it is necessary to test for potential periodicities taking into account that data gaps occur and that the data are therefore not evenly spaced. PAST [*Hammer et al.*, 2001] is a freely-available program with which Lomb periodograms can be calculated. This analysis is ideal for unevenly spaced data. It calculates normalized spectral power (referred to simply as power in what follows) as function of angular frequency (although it will be plotted as function of period for ease of reference). The significance level p of a peak $P(T)$ in power at a period T is given by *Press et al.* [2007] as $p = 1-(1-e^{P(t)})^{2N}$ with N the number of data points. For the purpose of the current study it is assumed that a periodicity occurs if the significance level is at most 0.01 (i.e. larger than or equal to 99%).

In Figure 4.4 the Lomb periodogram for variances calculated over a 27-day period is shown. The most significant peak above the 0.01 (99%) significance level corresponds to a period of 11.2 years, which indicates the presence of a significant ~11-year solar cycle dependency. A broad peak is also visible on the right side of the largest peak at ~36 years. However, because the data set spans only 38 years, the latter is disregarded.

The same steps as described for the 27-day period variance were implemented to obtain the 54-day period variance, shown in Figure 4.5. For the 54-day periods, a maximum lagtime of 160 hours was chosen. The peaks and solar cycle dependency seen in Figure 4.3 can also be seen here. An average was taken over the whole span for 54-day periods, which was found to be 11.87 nT^2, similar to that of Figure 4.3. So even though there seems to be more of a scattering with the 27-day periods than with the 54-day periods, both datasets average to roughly the same value. The Lomb periodogram for this longer period was also constructed, and is shown

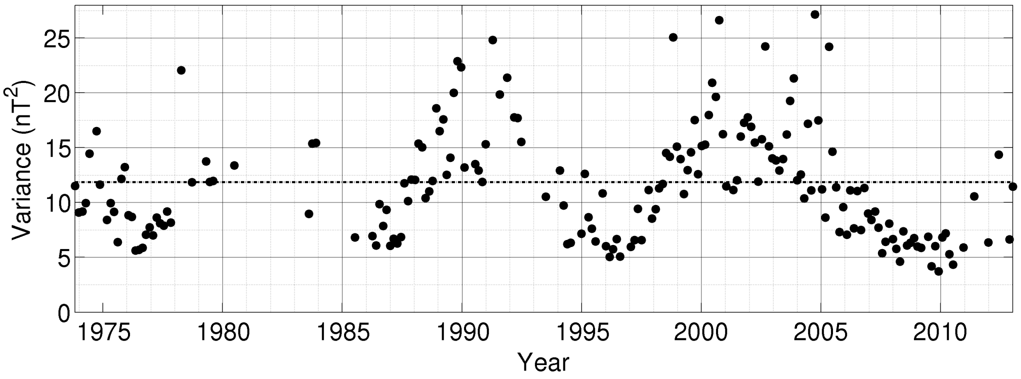

Figure 4.5: Similar to Figure 4.3. Here variance was calculated over 54-day periods. The peaks are more clear here, as well as the gap between 1980 and 1985 where very little data was available. The dashed line represents the average, which is ∼12 nT^2.

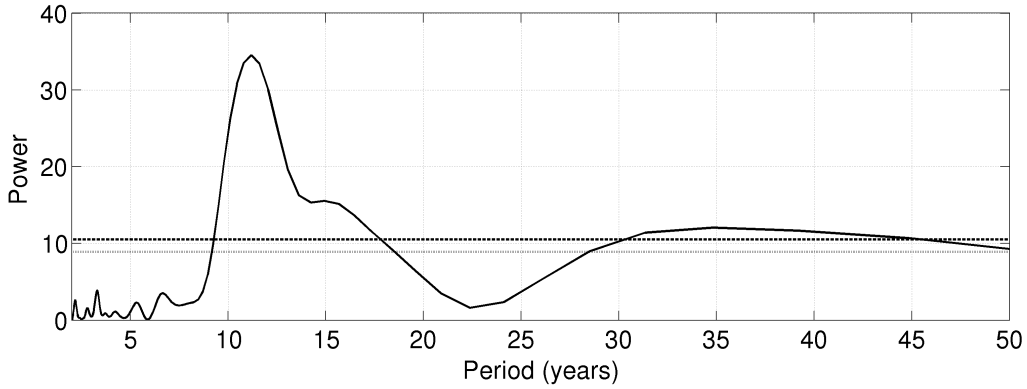

Figure 4.6: Similar to 4.4, but for variances taken over 54-day periods. Most significant peak is at 11.1 years. The dashed line indicates the 99% significance level, and the dotted line indicates the 95% significance level.

in Figure 4.6. For the 54-day period, the most significant peak is at 11.1 years.

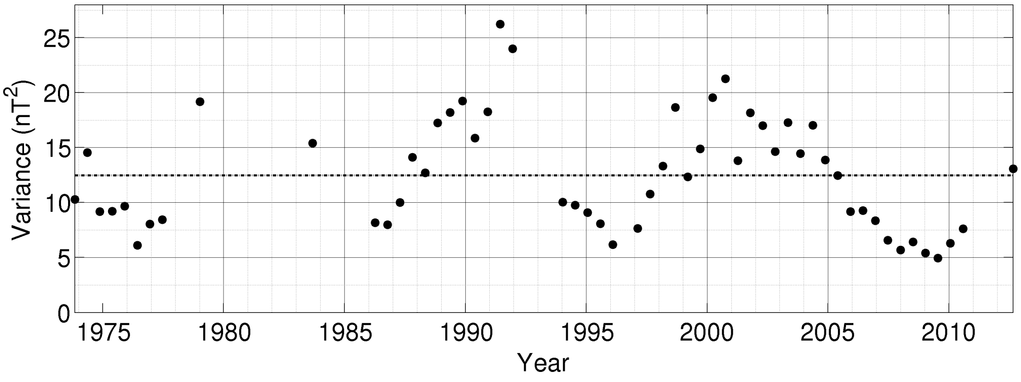

Figure 4.7: Similar to Figure 4.3. Here the variance was calculated over 189-day periods. Compared to Figure 4.3 and Figure 4.5, the cycle dependency is smoother and more clear over longer averaged data. The dashed line represents the average, of which the value is 12.5 nT^2.

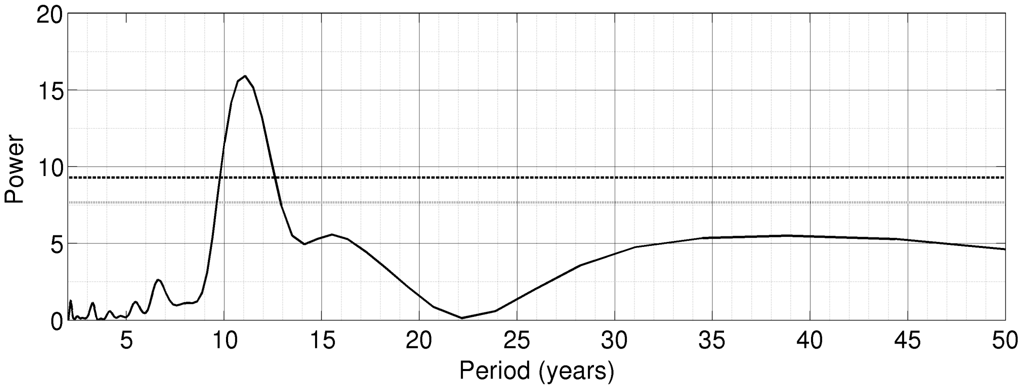

Figure 4.8: Similar to Figure 4.4, but for variances taken over 189-day periods. Most significant peak is at 11.1 years. The dashed line indicates the 99% significance level, and the dotted line indicates the 95% significance level.

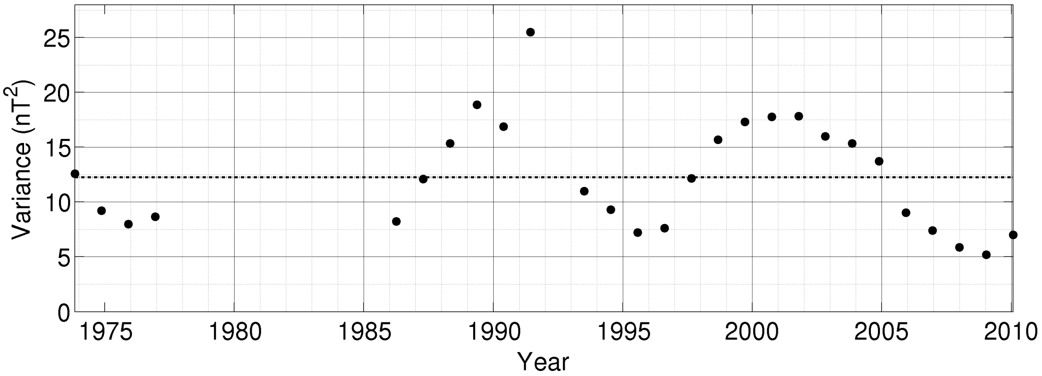

Figure 4.9: Similar to Figure 4.3. These are the longest averaged points, spanning just more than a year (378 days). Two clear peaks can be seen: a sharp peak at 1990, and a lower, more rounded peak at 2001/2002. the dashed line represents the average of 12.3 nT^2

Next variances calculated using 189-day periods (Figure 4.7) and 378-day periods (Figure 4.9) were evaluated. The averages taken over all the points for 189-day periods and 378-day periods were 12.5 nT^2 and 12.3 nT^2 respectively. Similar to Figure 4.3, in Figure 4.9 one sees that the variances for the most recent solar minimum around 2009 are lower than those during previous minima. For the 189-day and 378-day Lomb-periodograms seen in Figures 4.8 and 4.10, the most significant peaks are again seen at ~11 years, with another peak at ~40 years. Note the decrease in significance of the peaks relative to those shown for variances calculated using shorter averaging intervals; it decreases from 100% for the 27-day averages to 98.8% for 378-day averages.

The data gaps seen in the previous figures between ~1980 and ~1985 are troublesome, as information about that time is lost. To overcome this, 27-day period datasets were taken over a period of a year (14 in total) and averaged. This was done for each year. If there were less than 25% of the points available, that year was not considered, as motivated by the findings in Section 3.8. This has the advantage of allowing one to calculate the standard error, which

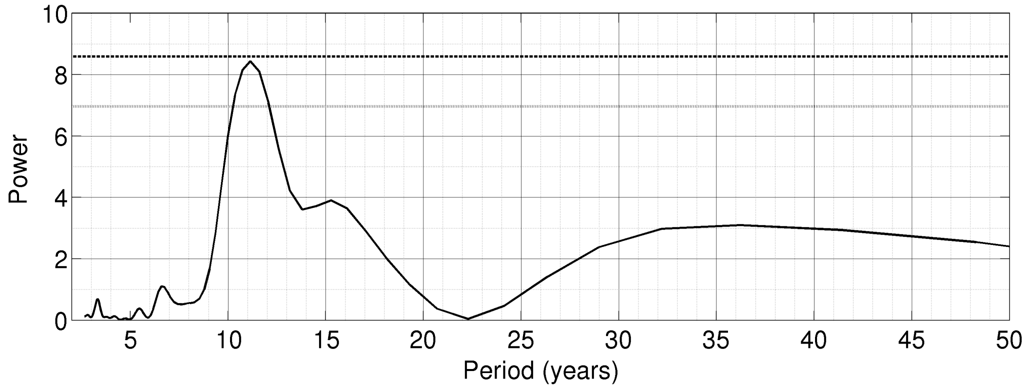

Figure 4.10: Similar to Figure 4.4, but for variances taken over 378-day periods. The most prominent peak is at 11.1 years, with a significance of 98.8%.

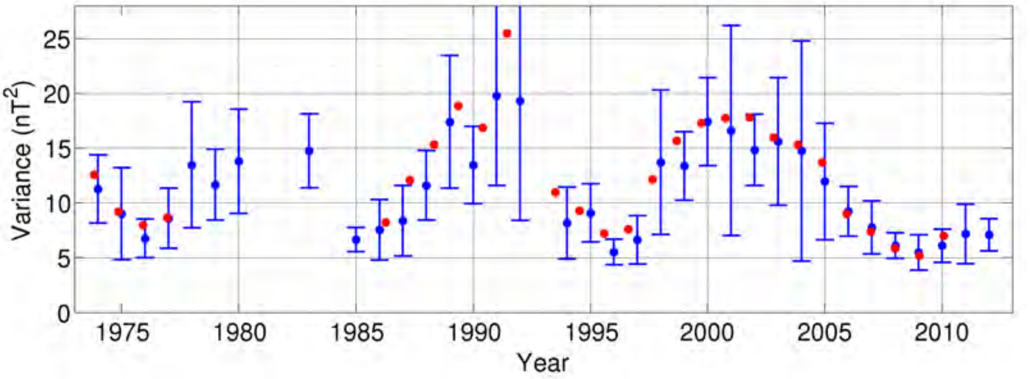

Figure 4.11: Two types of variance averages as function of time: the blue points represent variances calculated over 27-day periods averaged over a year, whereas the red points are variances calculated over 378-day periods (data from Figure 4.9). Error bars shown indicate the standard deviation.

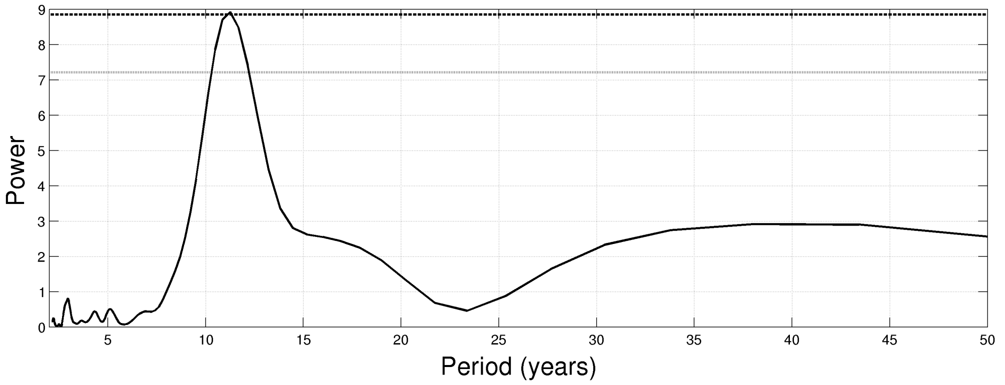

Figure 4.12: Lomb periodogram for the yearly binned variance dataset. An ∼11 year periodicity can be seen above the 99% significance level (dashed line).

is plotted as an error bar for each year. A comparison can be seen in Figure 4.11 between 27-day periods averaged over a year (blue dots with error bars) and 378-day periods (red dots)

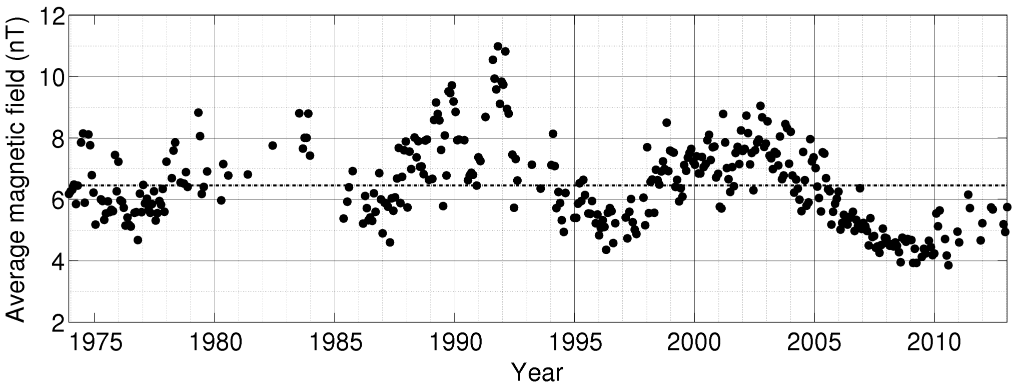

Figure 4.13: Magnetic field magnitude calculated using 27-day averages for data spanning from 1973 to 2012, with a mean of 6.5 nT indicated by a dashed line. Note the possible solar cycle dependency similar to Figures 4.3 - 4.9.

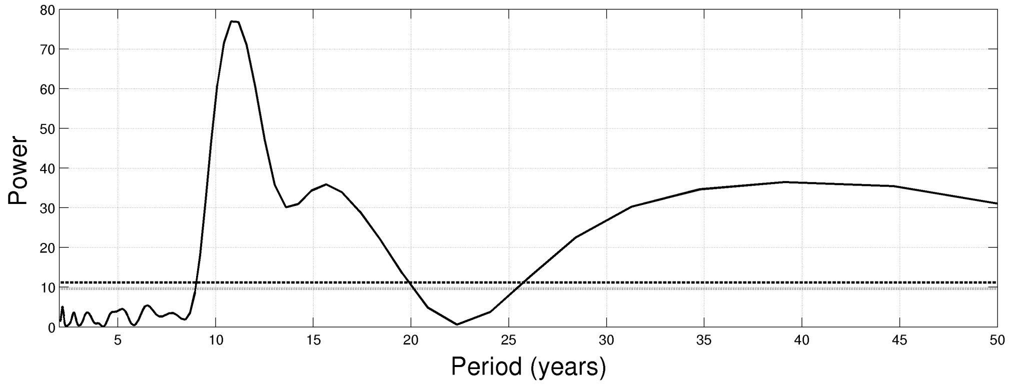

Figure 4.14: Lomb periodogram for the average magnetic field magnitude calculated over 27-day periods, taken over more than 38 years. Significant peaks (from right to left) are at ~39, ~16 and ~11 years respectively. The dashed line indicates the 99% significance level, and the dotted line indicates the 95% significance level.

as was shown in Figure 4.9. The two sets appear to follow each other well. There is however an indication in the 378-day averaged data of lower values during the 2009 solar minimum compared to the previous three; this does not show up in the binned yearly averages which shows similar values during the four solar minima. Now during the period between ~1980 and ~1985, data points are present, and a third peak is visible. The amount of binned 27-day period points (blue) outnumber the 378-day period points because it is more likely for an interval of 27-days to have less than 25% omissions, than for an interval of a year. Note that the error bars are quite large throughout the time-period, but are largest during solar maxima. By using 27-day data binned to a year rather than the 378-day data, a measure of uncertainty is available, as well as a bigger dataset. The Lomb periodogram for the yearly binned dataset is shown in Figure 4.12, and here a clear 11-year periodicity can be seen.

Average magnetic field magnitude data for the same period were taken and averaged to coincide with the variance data. As before, 27, 54, 189 and 378-day averaged sets were calculated,

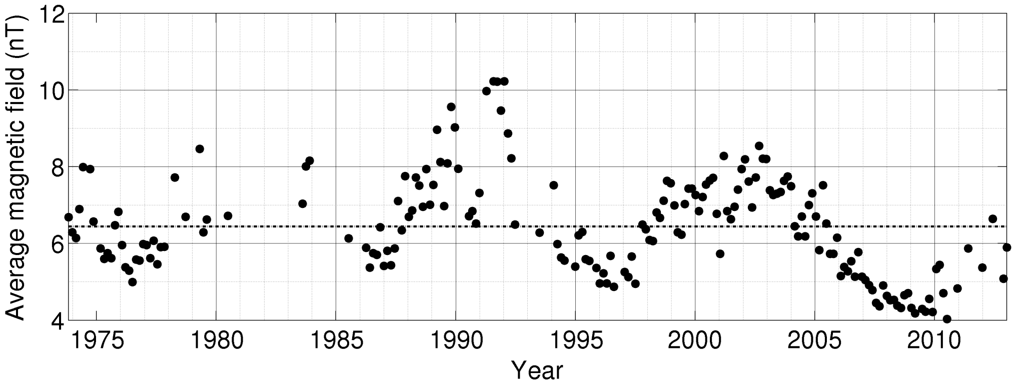

Figure 4.15: Similar to Figure 4.13, using time 54-day averages, with a mean of 6.4 nT indicated by a dashed line.

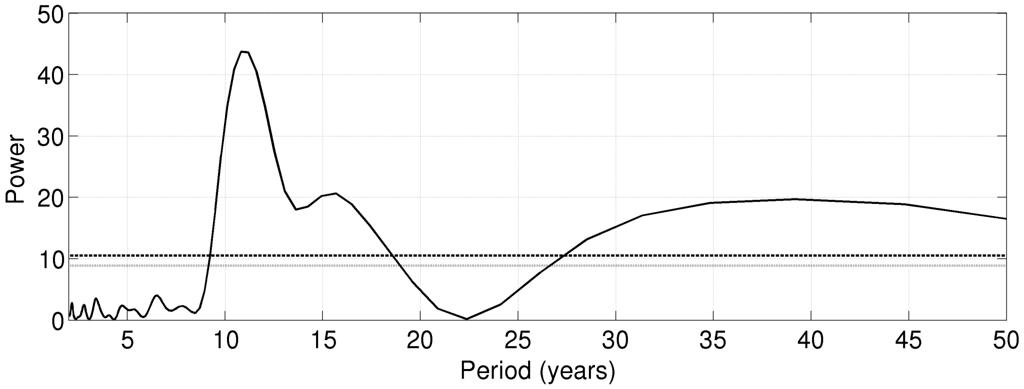

Figure 4.16: Similar to Figure 4.14, the Lomb periodogram taken over 54-day periods. Significant peaks are similar to the 27-day set. Significance levels of 99% and 95% are shown as dashed and dotted lines respectively.

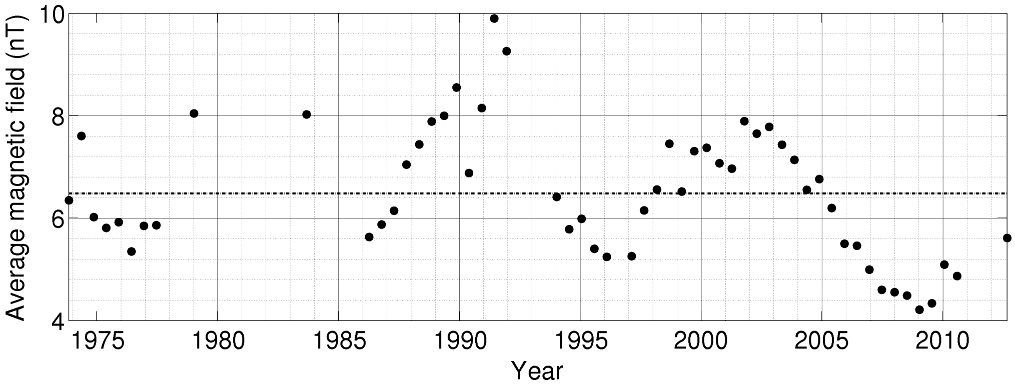

Figure 4.17: Similar to Figure 4.13, this time using 189-day averages, with a mean of 6.5 nT (dashed line).

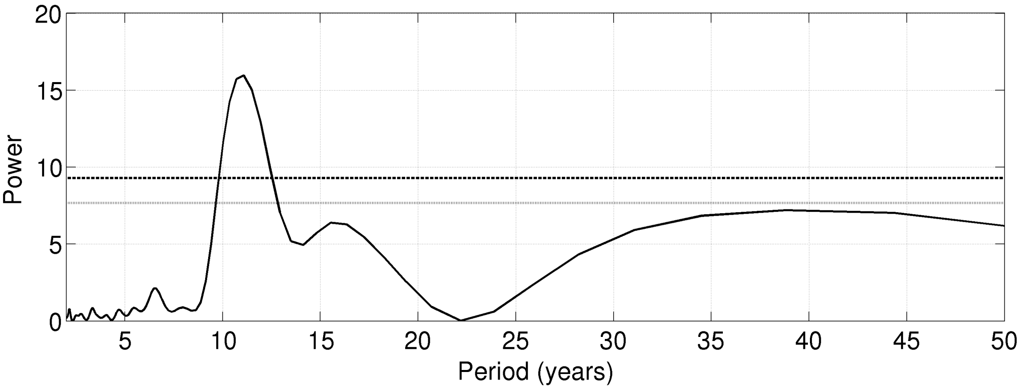

Figure 4.18: Similar to Figure 4.14, the Lomb periodogram taken over 189-day periods. Significant peak is at 11.1 years. Significance levels of 99% and 95% are shown as dashed and dotted lines respectively.

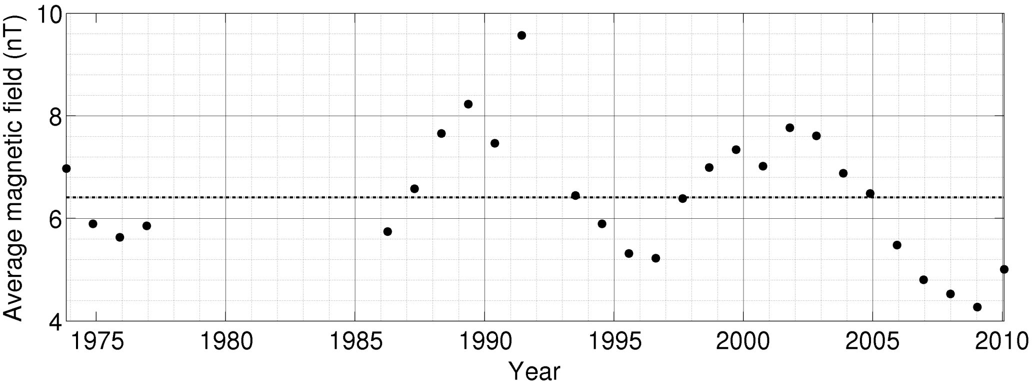

Figure 4.19: Similar to Figure 4.13, this time using 378-day averages, with a mean of 6.4 nT.

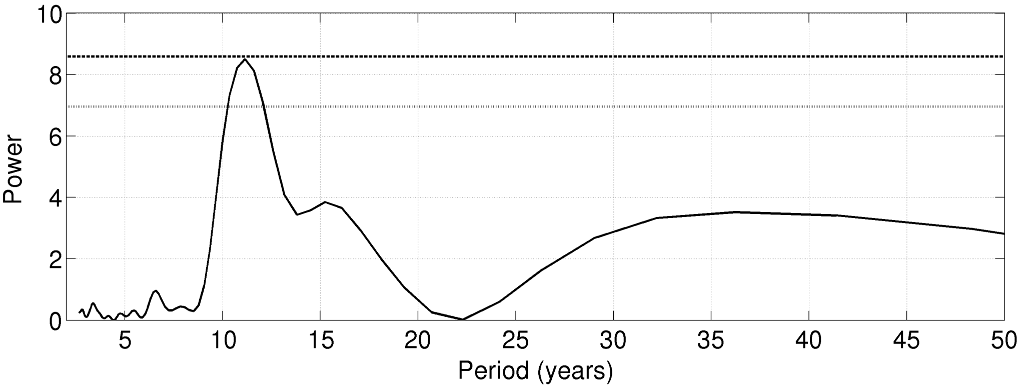

Figure 4.20: Similar to 4.14, but taken over 378-day periods. Significance levels of 99% and 95% are shown as dashed and dotted lines respectively.

and can be seen in Figures 4.13, 4.15, 4.17 and 4.19. For the 27-day set, an average of 6.5 nT was found over the whole period. For the 27-day Lomb periodogram in Figure 4.14, three clear peaks can be seen: the highest peak is at ∼10.8 years with a significance level of 100%.

Averages of 6.4 nT, 6.5 nT and 6.4 nT were found for the 54-, 189- and 378-day sets respectively. For the 54-day periodogram in Figure 4.16, the significant peak is at 10.8 years. As with the 27-day periogram, a smaller peak is visible on its right-hand side, which is also at ∼15 years, with a third peak at ∼40 years. Similar peaks are seen for the 189-day (Figure 4.18) and 378-day periodograms (Figure 4.20): a large peak at 11.1 years, a bump on the right side of the primary peak at ∼15 years, and a secondary peak at ∼40 years. Note that for all the periodograms the peaks are above the 99% significance level, except for the 378-day periodogram. This is similar to what is seen for the variance periodograms when longer intervals are employed, as the number of points that are used to construct the periodogram become less, which causes the decrease in significance of peaks on the corresponding Lomb periodograms.

The average period for the primary peak for all four periodograms is ∼11 years, which coincides with the periodicity of the primary peak for the variance data (also ∼11 years).

By comparing Figures 4.13-4.20 for magnetic field magnitude with Figures 4.3-4.10 for magnetic variance, which showed a clear solar-cycle dependence, similarities could be seen: three peaks are visible at ∼1981, ∼1991 and ∼2002, which coincides with high solar activity. Magnetic field magnitudes during the last minimum at ∼2009 appear lower than those during previous minima. Overall, the two sets appear to follow each other well.

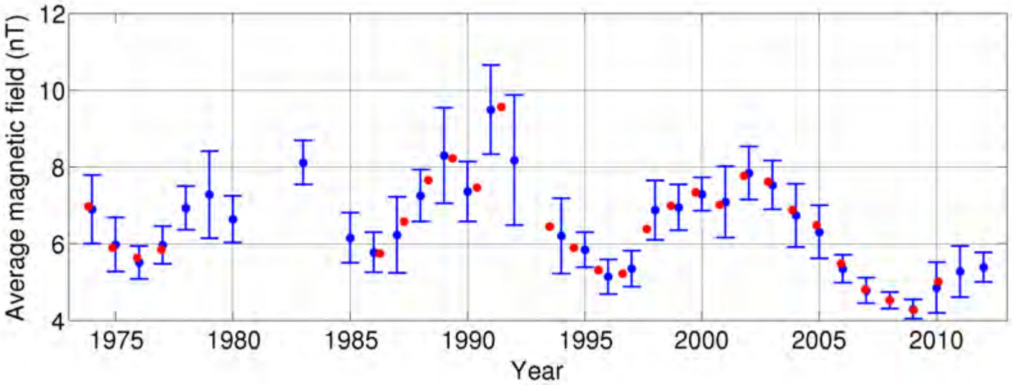

Figure 4.21: Similar to Figure 4.11: the blue points represent magnetic field data calculated over 27-day periods averaged over a year, whereas the red points are calculated over 378-day periods (data from Figure 4.9). The standard deviations determined for the blue points are shown as error bars.

In Figure 4.23, 27-day period datasets are shown for both the magnetic field magnitude and variance, binned into 14 yearly averages. Years with less than 25% of points available were neglected. The standard deviation for each year-point was calculated and plotted as an error bar. With this method, there are now datapoints between ∼1980 and ∼1985 data points, and a third peak can be seen for that period. The magnetic field and variances clearly show the same 11-year solar cycle dependency, with maximum and minimum values corresponding to

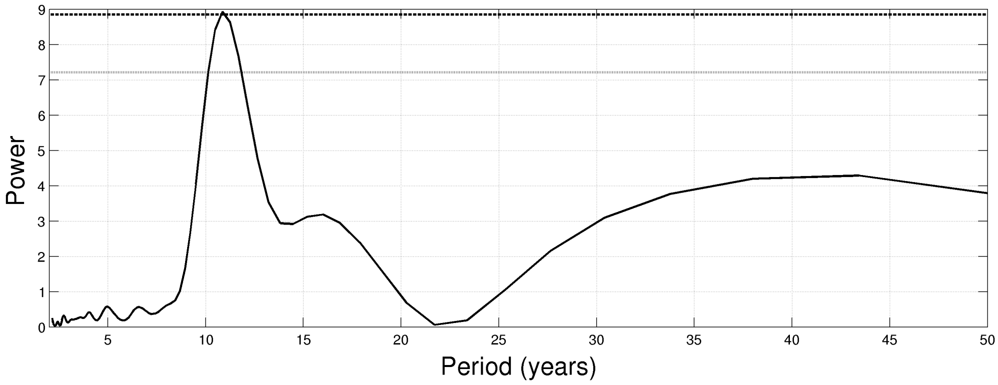

Figure 4.22: Lomb periodogram for the yearly binned dataset for the magnetic field. A peak above the 99% significance level can be seen at ∼11 years. Significance levels of 99% and 95% are shown as dashed and dotted lines respectively.

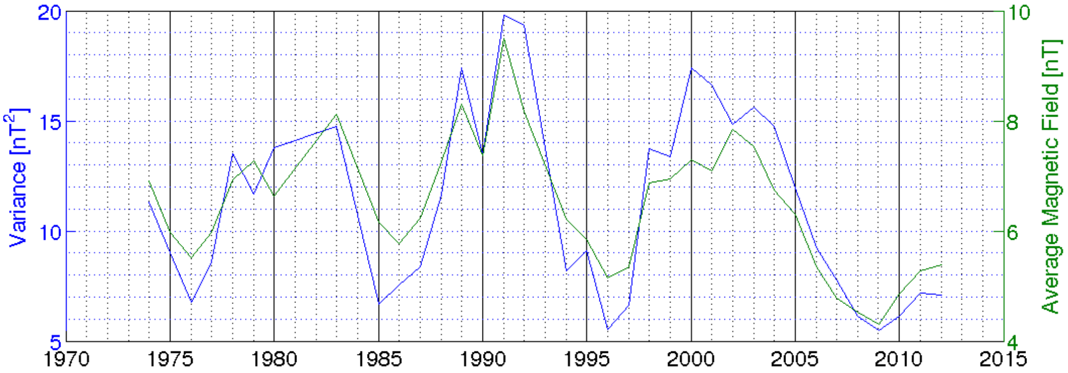

Figure 4.23: 27-day yearly binned datasets for variance and the magnetic field magnitude.

periods of maximum and minimum solar activity. Both quantities become very small during the recent unusual solar minimum, with values in 2009 considerably below that of previous solar minima.

By taking the square root of the variance σ^2 for the 27-, 54-, 189- and 378-day periods (shown in Figures 4.3, 4.5, 4.7 and 4.9) and dividing it by the corresponding solar magnetic field magnitudes B_m (shown in Figures 4.13, 4.15, 4.17 and 4.19) for the same averaging periods, Figures 4.24, 4.26, 4.28 and 4.30 were constructed. An average over the whole period for the 27-day and 54-day sets was found to be ∼0.52. For the 189-day and 378-day datasets it was found to be ∼0.53. At first glance, especially when looking at the 27-day dataset in Figure 4.24, no periodicity could be seen. This is hardly surprising, considering that this dataset was constructed using variance and magnetic field data which both showed clear periodicities of ∼11 years. In Figures 4.25, 4.27, 4.29 and 4.33 the Lomb periodograms are shown for 27-, 54-, 189- and 378-day sets respectively. In Figure 4.25 two peaks are seen under the 99% significance level and in Figures 4.27, 4.29 and 4.33 no peaks even close to the 95% significance level can be seen.

Figure 4.32 shows the 27-day σ/B_{mag} values, which were binned in yearly intervals. Note the

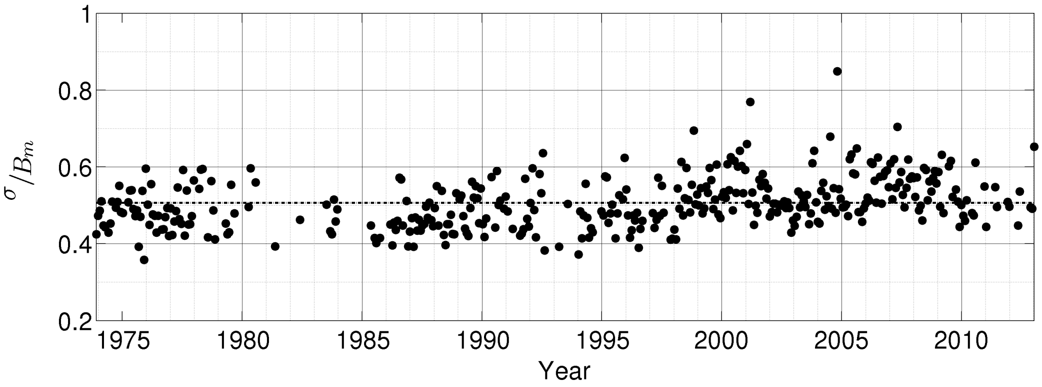

Figure 4.24: The ratio of the root of the variance to the average magnetic field (σ/B_m) calculated and averaged over 27-day periods. The dashed line represents the average taken over all points, including periods of solar maximum and minimum, with a value of 0.5.

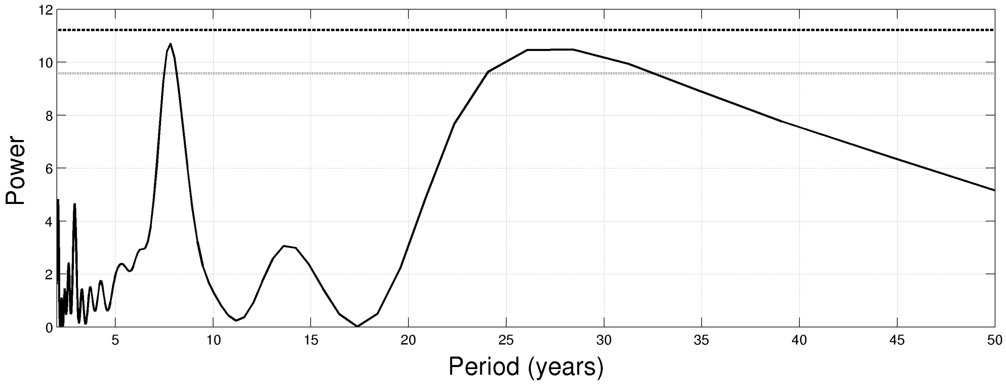

Figure 4.25: Periodicity of the square root of variance, divided by the magnetic field data, calculated over 27-day periods, taken over more than 38 years. Significant peaks are at 8 years and 25 years. Both are approximately at the 98% significance level.

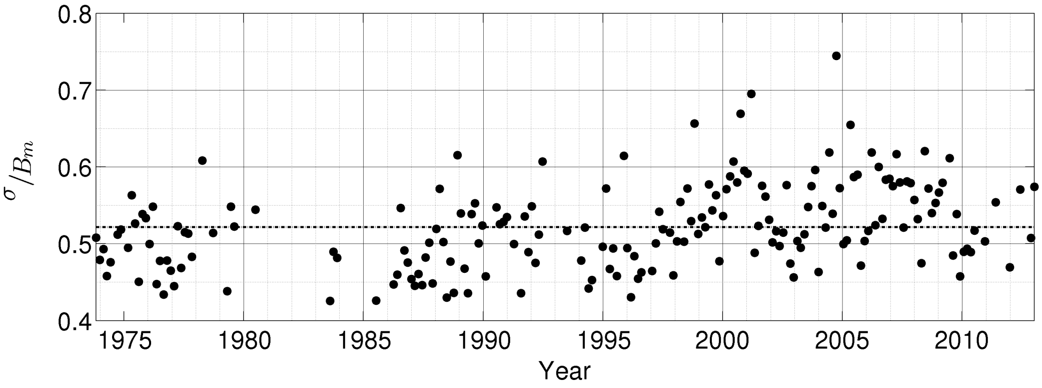

Figure 4.26: Similar to 4.24, where σ/B_m was calculated and averaged to 54-day periods. Again, as in 4.3, note the gap between 1980 and 1985 due to averaging. The average value over the whole period is 0.52 (dashed line).

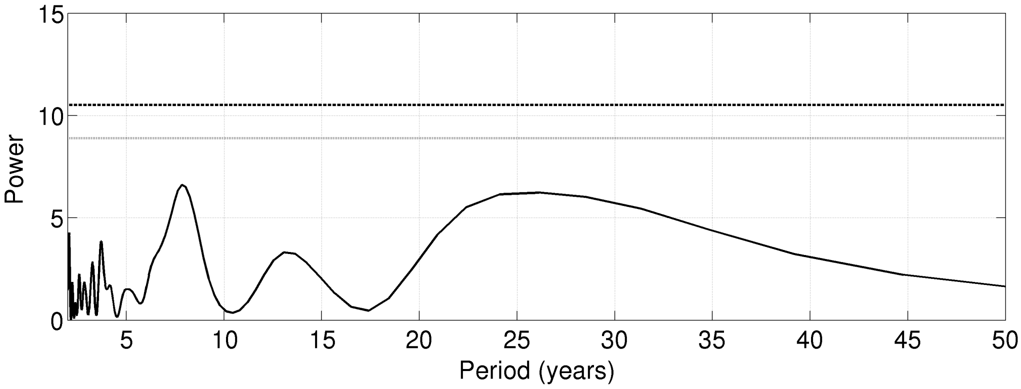

Figure 4.27: Similar to 4.25, but taken over 54-day periods. No peaks rise above the 95% significance level, and the highest value is around 64%.

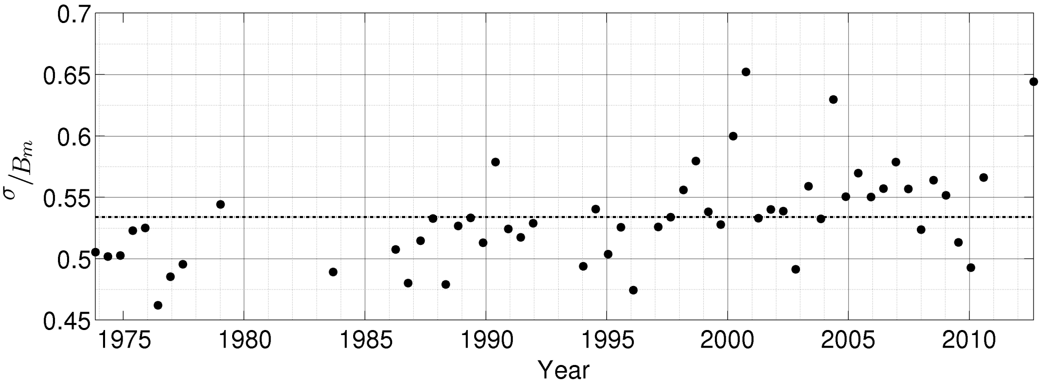

Figure 4.28: Similar to 4.24, where σ/B_m was calculated and averaged to 189-day periods. The average value over the whole period is 0.53.

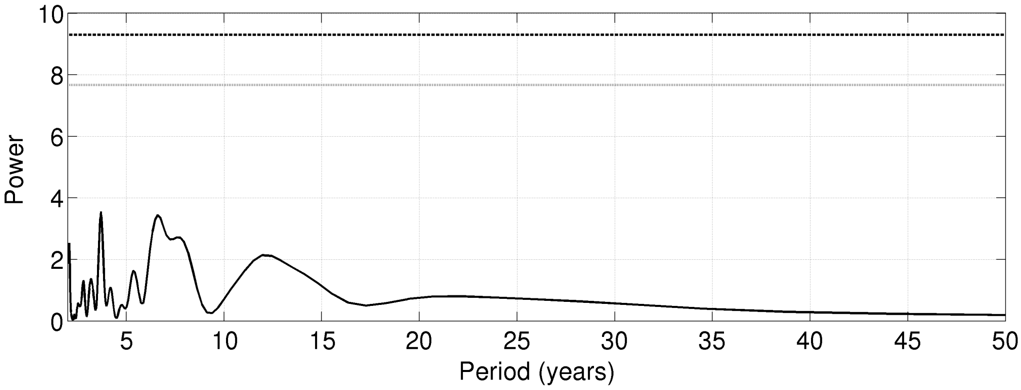

Figure 4.29: Similar to 4.25, but taken over 189-day periods. As with the 54-day period set, all peaks are below the 95% significance level. Here the highest level is at around 1% significance..

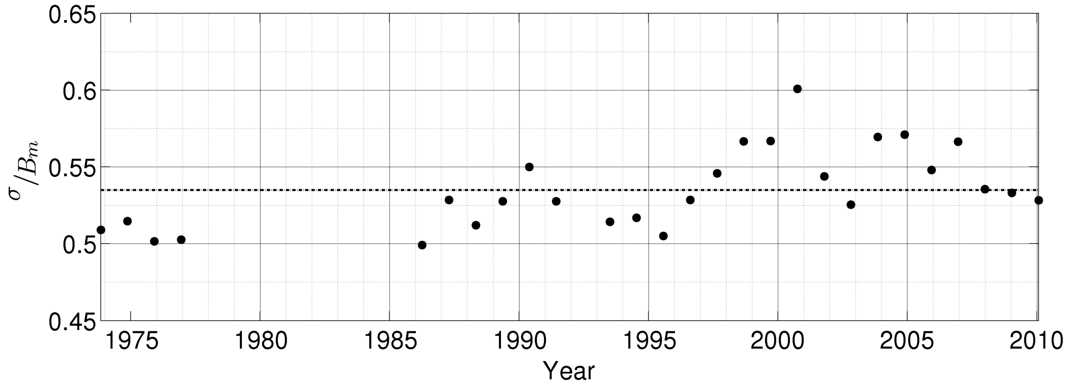

Figure 4.30: Similar to 4.24, where σ/B_m was calculated and averaged to 378-day periods. The average value is 0.53.

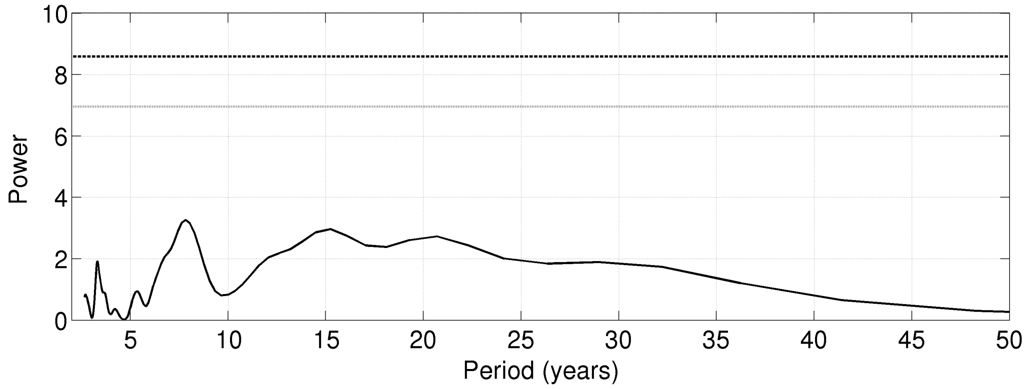

Figure 4.31: Similar to 4.25, but taken over 378-day periods. All peaks are below the 95% significance level, with the highest indicating a significance of around 10%.

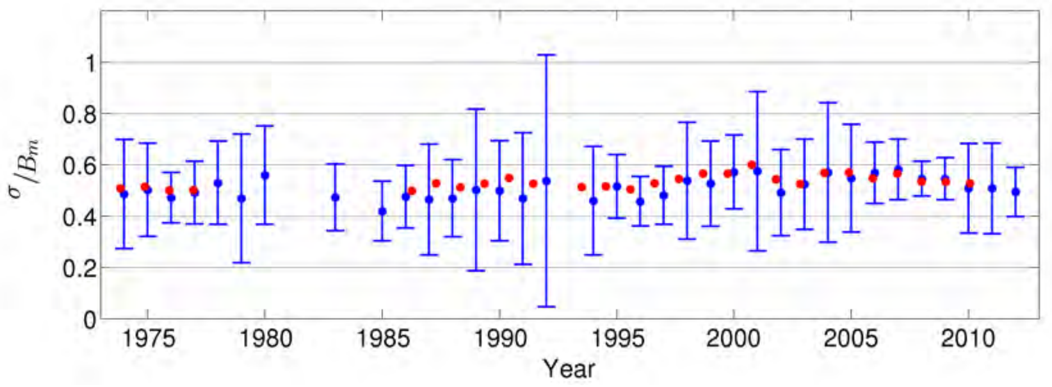

Figure 4.32: The ratio of the square root of the variance over the average magnetic field shown here as 27-day datasets averaged to a year, compared to the 378-day variance over the average magnetic field dataset.

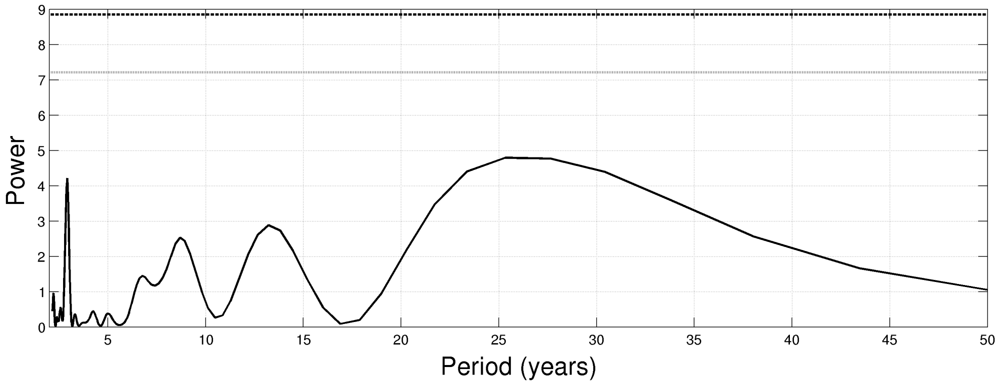

Figure 4.33: Lomb periodogram for the 27-day period square root of the variance over the average magnetic field dataset taken in yearly bins. No peaks above the 99% significance level occur, the highest probability for any periodicity is around 50%. .

gap caused by lack of data that was seen in the previous figures (for example Figure 4.33) is now filled. Figure 4.33 shows the Lomb periodogram for this set, and no peaks above the 99% significance level can be seen. Significant periodicities were seen for magnetic variance and magnetic field data respectively, but not for the σ/B_{mag} 27-, 54-, 189-, and 378-day sets. The reason for this is that strong periodicities seen in both magnetic variance and magnetic field data cancel out when divided and will, due to this, not be picked up with a Lomb periodogram.

4.4 Inertial Range Spectral Index

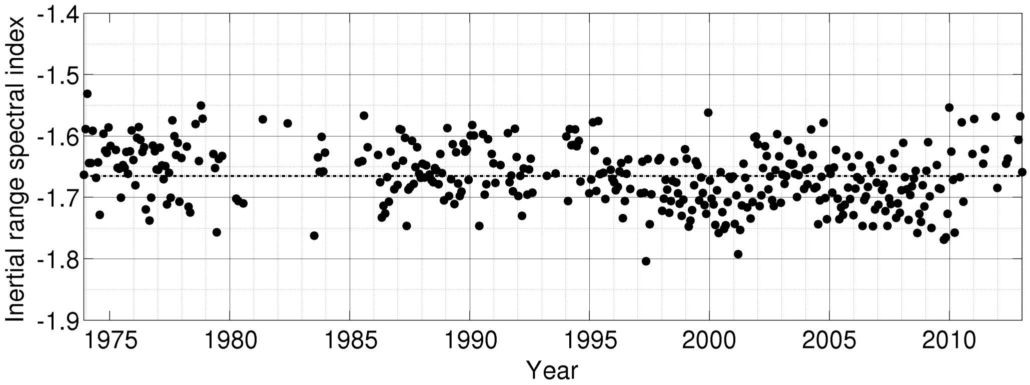

Figure 4.34: 27-day period dataset for the inertial range spectral index, from 1974 to 2013. The average value over the whole period is -1.67.

From here on we consider only 27-day and yearly binned datasets. From these two sets all necessary information can be ascertained. The 27-day data gives the best indication of any periodicity, while the yearly-binned 27-day values give a good indication of the long-term beviour of a quantity, without the scatter present in the 27-day data. Moreover, error bars can then be constructed, which give an indication how the scatter in the data changes with solar

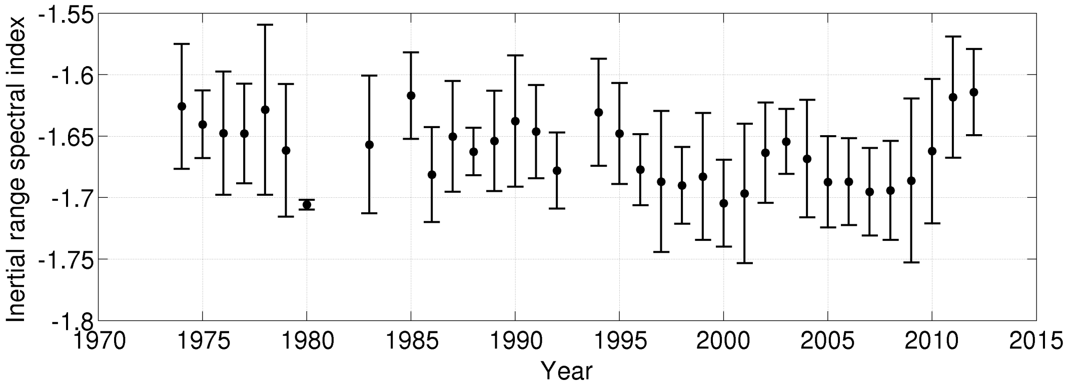

Figure 4.35: 27-day period datasets binned to a year, for the inertial range spectral index.

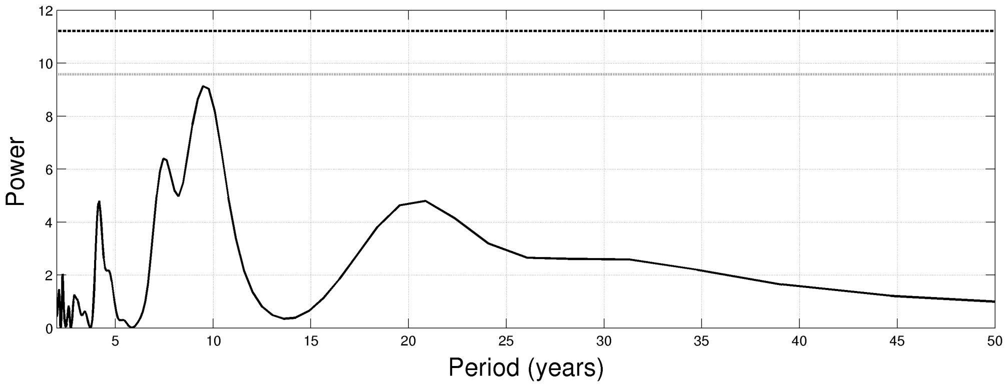

Figure 4.36: Lomb periodogram for the 27-day period inertial range spectral index dataset. The largest peak is at 90%, below the 95% significance level (dotted line), is at ~9 years.

activity.

In Figure 4.34, the 27-day period dataset is shown for the period between 1974 and 2013. Very little scatter in the data can be seen here, with values ranging mainly between -1.6 and -1.7. An average value for this set was found to be -1.67. Note also the lack of data between ~1980 and ~1985. By binning 27-day period datasets to a year, Figure 4.35 was constructed. From the Lomb periodogram for the 27-day dataset shown in Figure 4.36, no significant peaks could be seen.

4.5 Turnover Scale

Figure 4.37 shows the 27-day period dataset for the turnover scale in hours. Here the values seem more scattered, compared to the dataset for the inertial range spectral index in Figure 4.34, and an average of 0.46 hours was found for this period. As with all the previous 27-day period datasets, a data gap can be seen in the mid-80's. The Lomb periodogram for the data shown in Figure 4.38 is plotted in Figure 4.39. Here, only one peak at ~43 years, just reaches

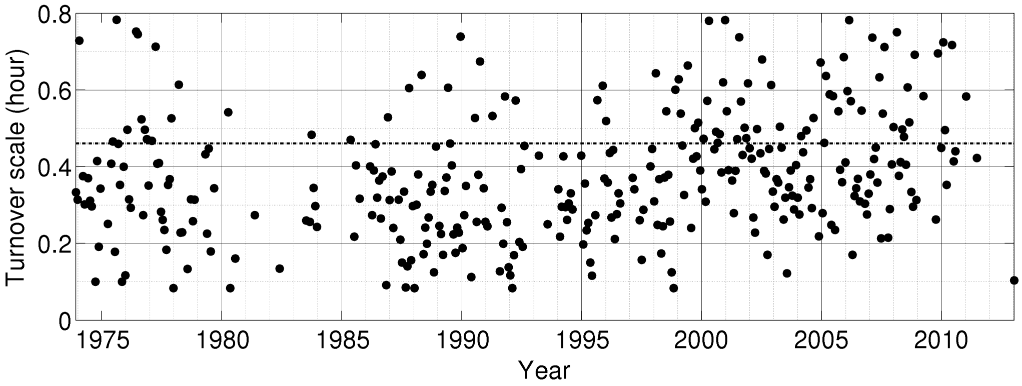

Figure 4.37: 27-day period dataset for the turnover scale (in hours). The average value over the whole period is 0.46 hours (dashed line).

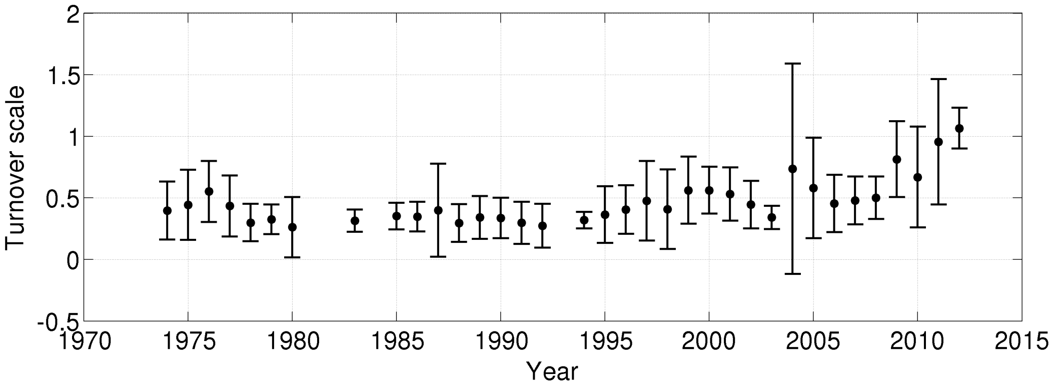

Figure 4.38: 27-day period datasets binned to a year for the turnover scale, measured in hours. Error bars shown are the standard deviation from the various points.

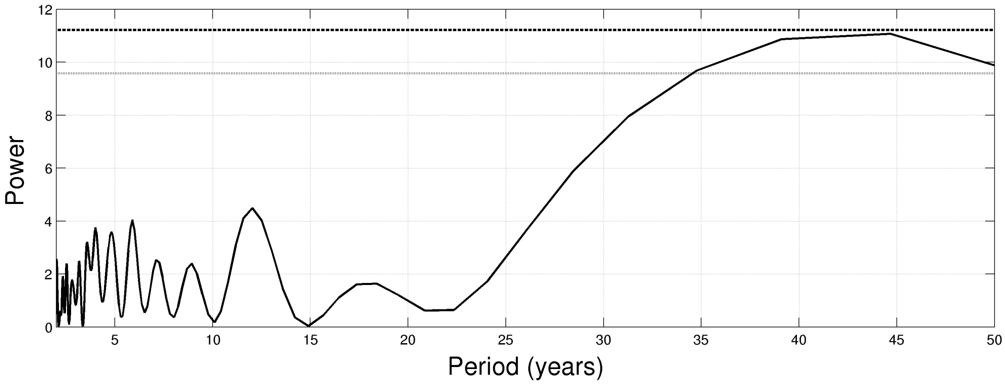

Figure 4.39: Lomb periodogram for the 27-day period turnover scale dataset.

the 99% significance line. However, given that the data set spans only 38 years, this result is disregarded. It has to be kept in mind that it has been shown in Section 3.8 that the method employed here consistently leads to a discrepancy between the turnover scale specified in a generated dataset, and that calculated using this method.

4.6 Level of energy spectrum at 14-hours

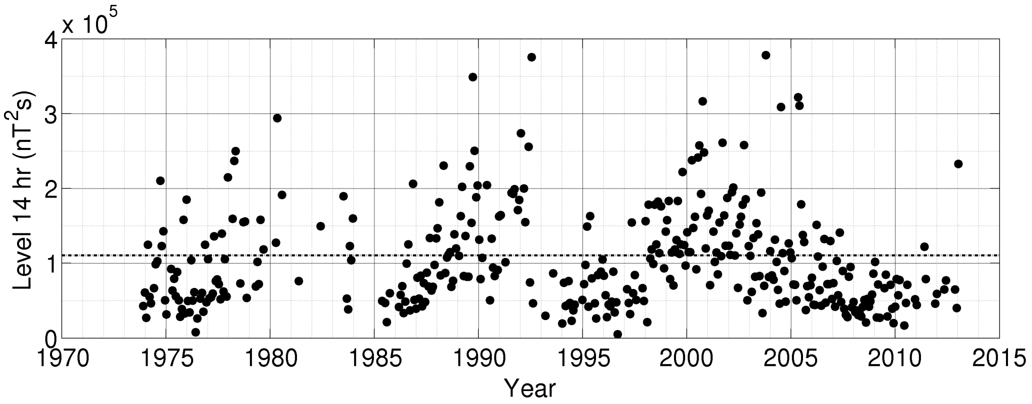

Figure 4.40: 27-day period datasets for the 14-hour spectral level. The average over the whole period is 1.1×10^5 nT^{2}s (dashed line).

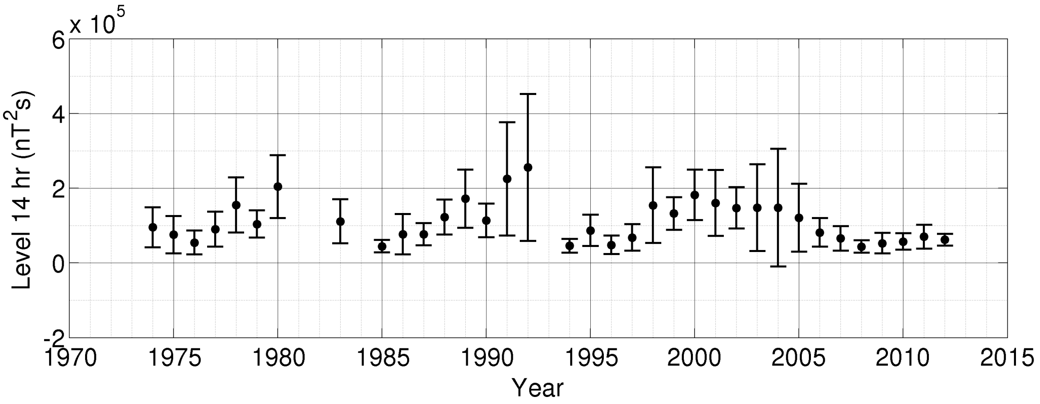

Figure 4.41: 27-day period datasets binned to a year for the 14-hour spectral level (in nT^{2}s).

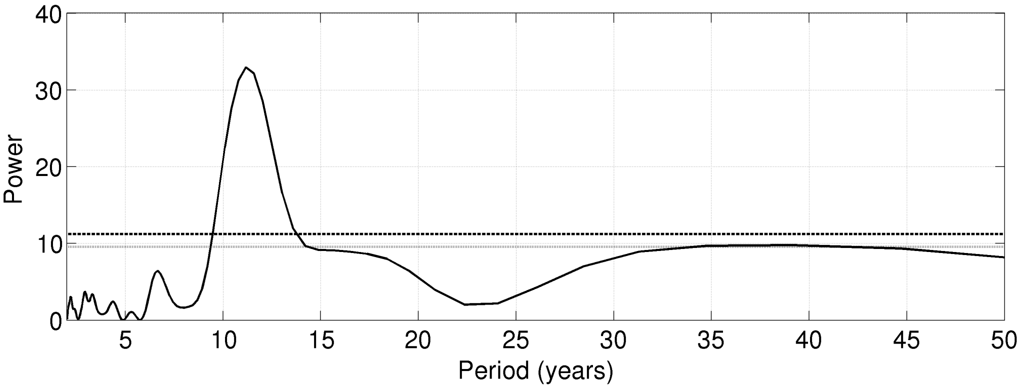

Figure 4.42: Lomb periodogram of the level of spectrum at 14 hours for the 27-day dataset. A peak at ~11.1 years is seen well above the 99% significance level (dashed line).

The energy spectrum discussed in Section 3.6 was used to calculate the level of the spectrum at 14 hours (1.98×10^{-5} Hz), assumed to be well within the energy-containing range. This value was chosen for comparison with observations reported by *Bieber et al.* [1993], which will be shown later in this chapter. This is shown in Figure 4.40 for the 27-day period dataset, where the average value over the whole period was 1.1×10^5 nT^{2}s. The 27-day period data binned to a year is shown in Figure 4.41 where the average was found to be 1.1 $\times 10^5$ nT^{2}s and a possible periodicity can be seen. The Lomb periodogram shown in Figure 4.42 confirms this, and an $\sim$11.1 year periodicity can be seen at a 100% significance level.

4.7 Energy-Containing Range Spectral index

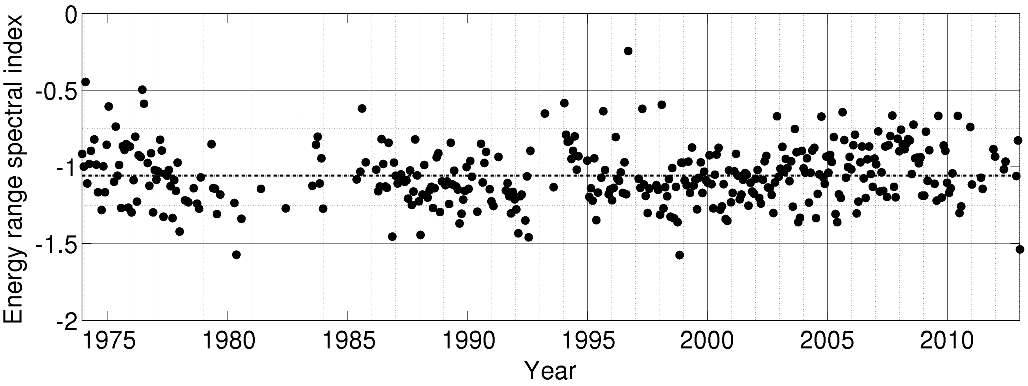

Figure 4.43: 27-day period dataset for the energy range spectral index, covering 1974 to 2013. An average value of -1.1 was found over the whole period (dashed line).

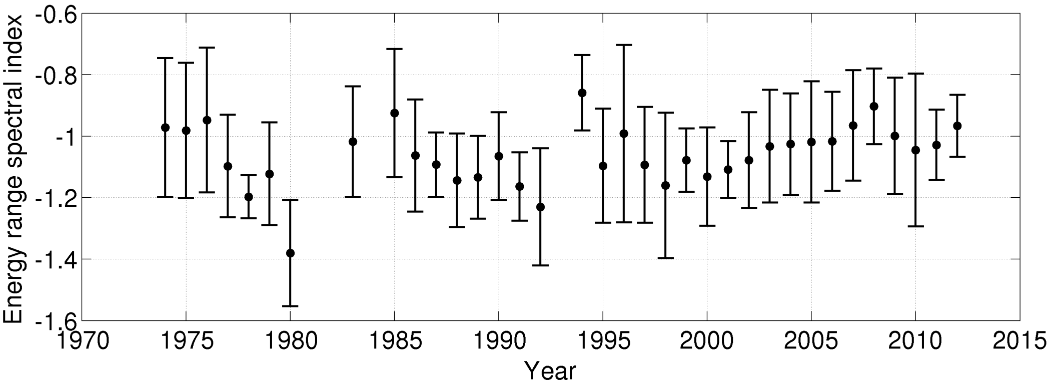

Figure 4.44: As in Figure 4.43, but for 27-day averaged values of the energy range spectral index (average -1.1).

Figure 4.43 shows the 27-day period dataset for the energy range spectral index. The data points are mainly clustered between -0.5 and -1.5, with an average value of -1.1. The 27-day data binned to a year is shown in Figure 4.44, where the average was also found to be -1.1. By looking at these two graphs, and at the Lomb periodogram for the 27-day dataset in Figure 4.45, an $\sim$11 year periodicity can be seen.

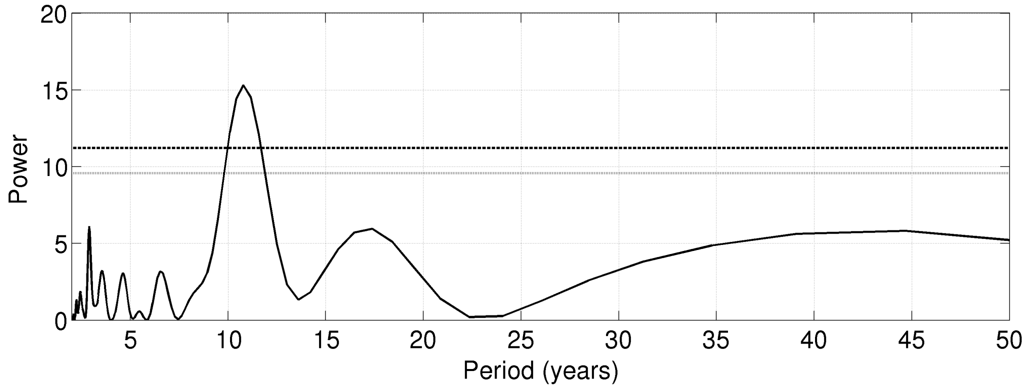

Figure 4.45: Lomb periodogram for the 27-day period datasets for the energy range spectral index. A peak with a significance level of 99.98% is seen at ~11 years.

4.8 Cutoff Scale

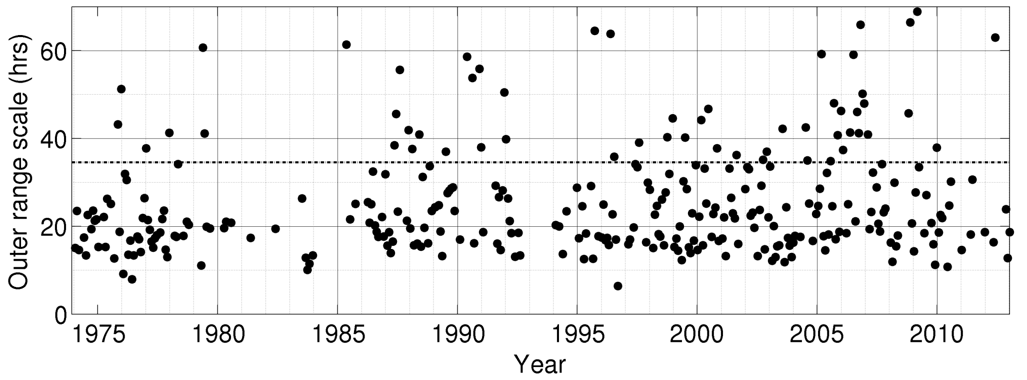

Figure 4.46: 27-day period dataset for the cutoff scale. The average over the whole period is 34.6 hours.

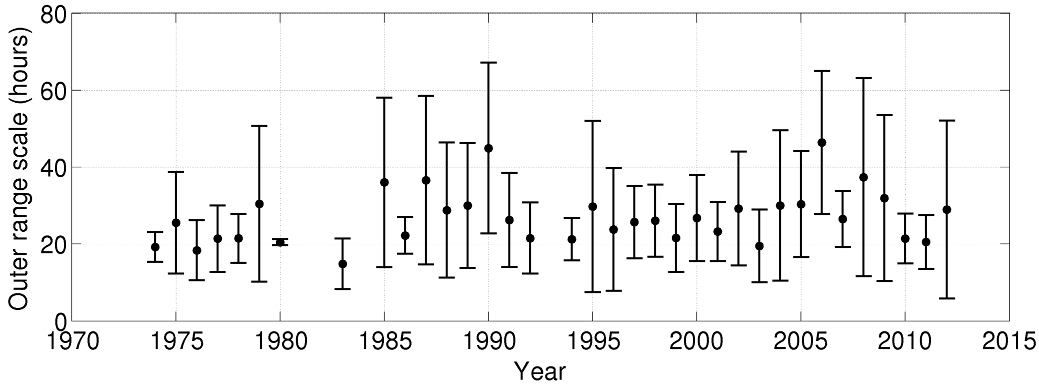

Figure 4.47: 27-day period datasets binned to a year for the cutoff scale, measured in hours. Error bars shown are the standard deviation from the various points.

In Figure 4.46, the 27-day period dataset for the cutoff scale, measured in hours, is shown.

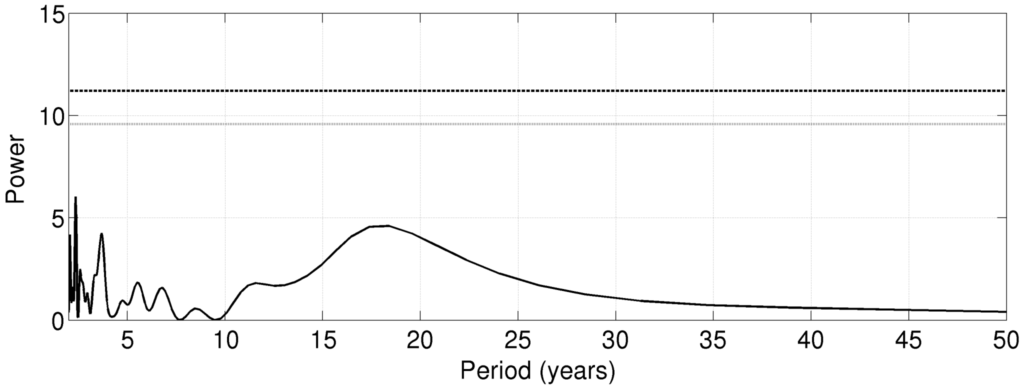

Figure 4.48: Lomb periodogram of 27-day period datasets for the cutoff scale measured in hours. No significant peak is present.

Significant scattering can be seen in the data, and values range from around 10 to over 60 hours, with an average value of 27 hours. Note that during the fit-phase where these values are determined, a default boundary value exists for the fit: the maximum lagtime for the 27-day dataset is 80 hours, so the fit-function will continue to search for the cutoff scale until it reaches this maximum value, and will then assign this as the default value if no cutoff scale could be determined for that timestep. A significant proportion of the output values over 38 years were at this default value (not shown in the figure), which is an indication of the difficulty of resolving this quantity. The 27-day period set binned to a year is shown in Figure 4.47, from which the default 80-hour values were removed beforehand. Here, as in Figure 4.46, no periodicity can be discerned. The Lomb periodogram for the 27-day dataset is shown in Figure 4.48, and shows no significant periodicity.

4.9 Outer Range Spectral Index

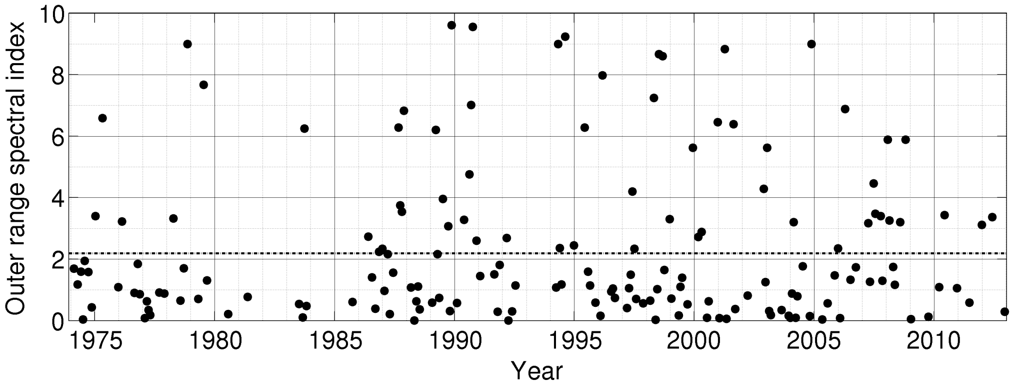

Figure 4.49: 27-day period dataset for the outer range spectral index, stretching from 1974 to 2013. The average value over the whole period is 2.19 (dashed line).

In Figure 4.49 the 27-day period dataset for the outer range spectral index is shown. Also

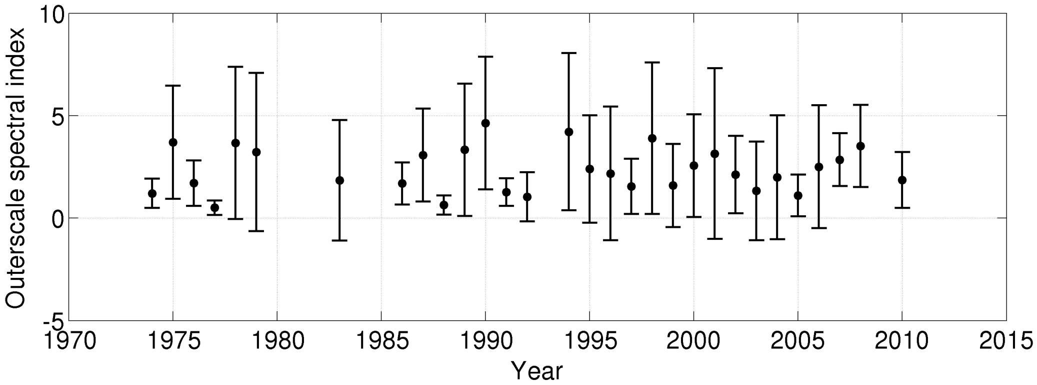

Figure 4.50: As in Figure 4.49, but for 27-day averaged values of the outer range spectral index.

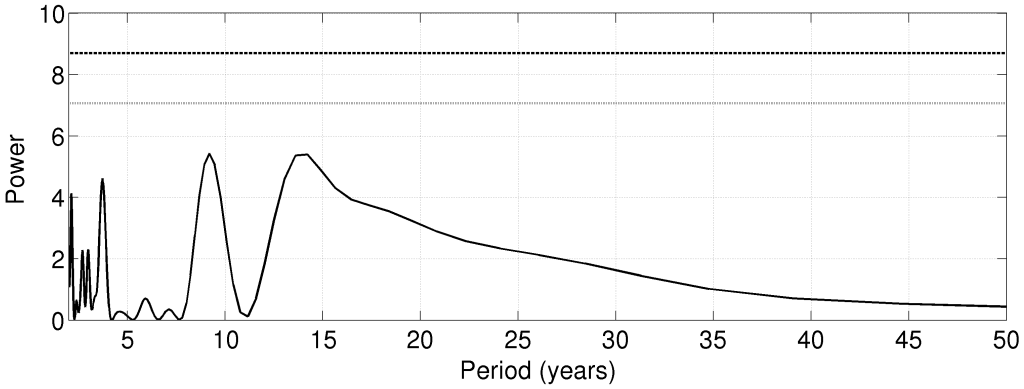

Figure 4.51: Lomb periodogram for the 27-day period datasets for the outer range spectral index. No significant peaks are visible.

shown is the 27-day period dataset binned to a year in Figure 4.47. During the fit-stage of the integrated energy spectrum, boundary values were specified for the outer range spectral index so that $0 < p < 5$, in order to ensure a finite energy density. If during this time no index could be determined, these default boundary values would be assigned for that timestep. This was true for a significant portion of the dataset, but these values were omitted from Figures 4.49 and 4.50. The Lomb periodogram for the 27-day values for this quantity, shown in Figure 4.51, shows no significant periodicity.

4.10 Comparisons with other studies

The results found in this study for the variance, inertial range spectral index, turnover scale, 14-hour level of the spectrum and energy range spectral index are now compared with the findings of previous studies, as was discussed in Section 2.10. No observations exist for the cutoff scale, and for this quantity a possible distribution of values to add to the average value is given.

4.10.1 Magnetic Variance

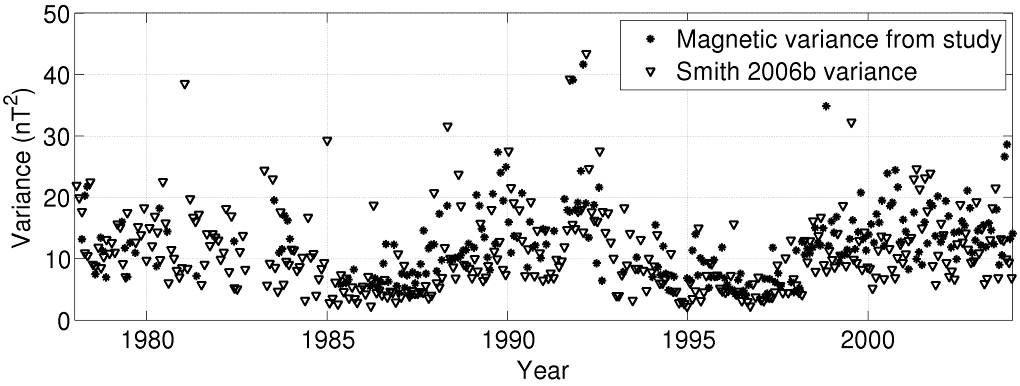

Figure 4.52: Comparison between *Smith et al.* [2006b] $\langle B_N^2 \rangle$, discussed in Section 2.11, and the magnetic variance derived in this study.

The magnetic variance determined by *Smith et al.* [2006b] (shown in Section 2.11) is now compared with the magnetic variance calculated in this study (shown in Figure 4.3). Both are shown in Figure 4.52, where the average found for the Smith dataset was 10.6 nT^2 and for this study 11.3 nT^2, about 6% smaller. There is therefore good agreement between the results presented by *Smith et al.* [2006b] and those found in this study. The total variance in one perpendicular component of the field was found to be 13.2 nT^2 by *Bieber et al.* [1994]. This also compares well with a yearly-averaged value found in this study, which at 12.3 nT^2 is about 7% smaller.

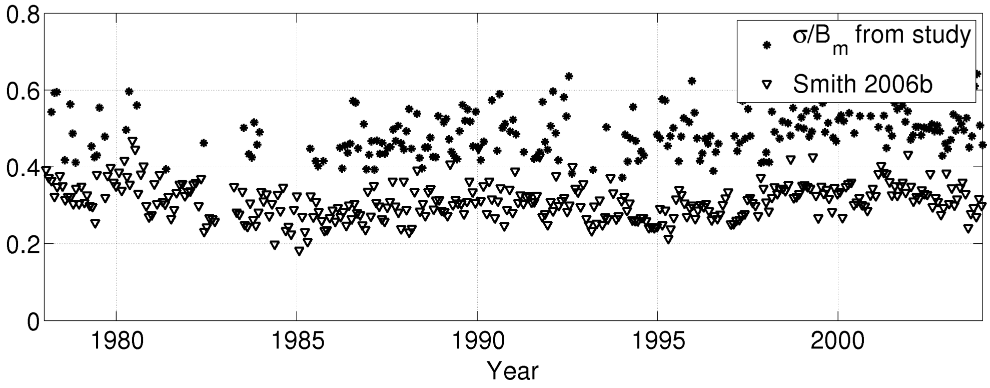

Figure 4.53: Showing comparison between *Smith et al.* [2006b] $\langle B_N/B \rangle$, that was shown in Figure 2.20, with σ/B_N derived in this study.

Similar to the previous Figure, the square root of the magnetic variance divided by the magnetic field that was shown in Figure 4.24 is now compared with $\langle B_N/B \rangle$ from *Smith et al.* [2006b]. Both are shown together in Figure 4.53. Here the agreement is not nearly as good. The average for this study was 0.51, and that of Smith was 0.31. The reason for this difference is still uncertain.

4.10.2 Inertial range spectral index

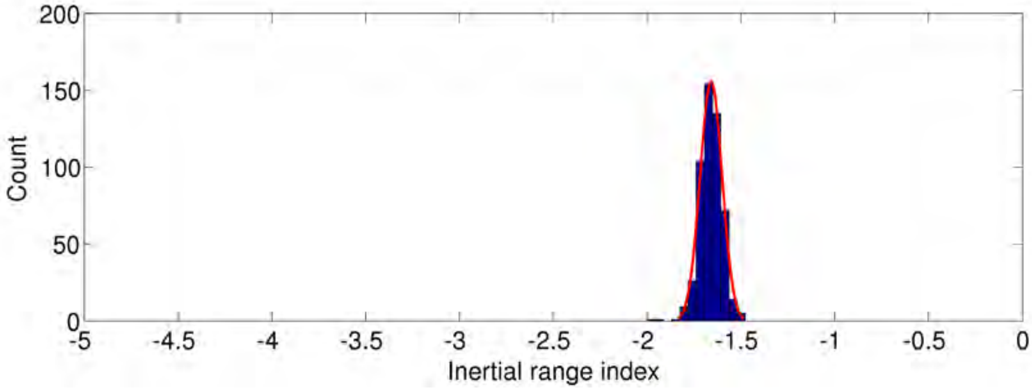

Figure 4.54: Inertial range spectral index histogram with normal (Gaussian) distribution fit, shown here on a similar index scale as in Figure 4.55.

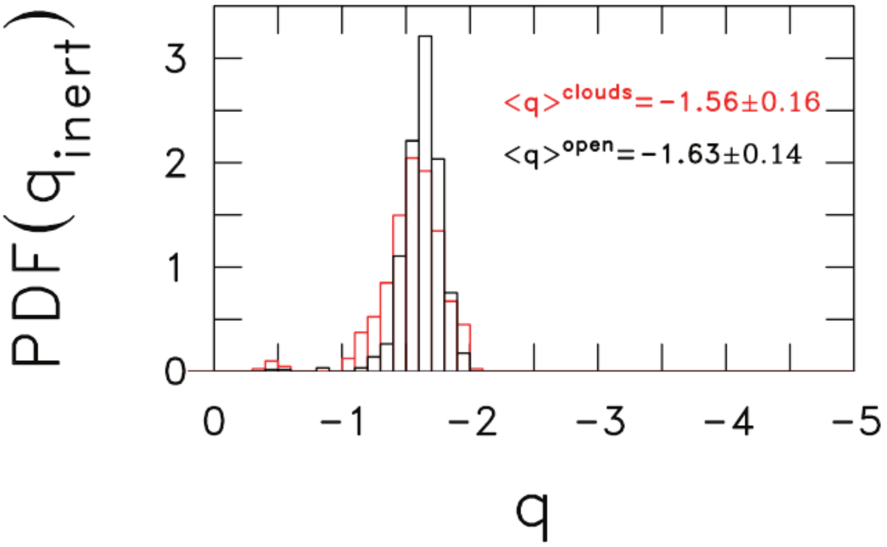

Figure 4.55: Distribution of inertial range power-law indices [*Smith et al.*, 2006a].

The 27-day period dataset shown in figure 4.34 was used to create a histogram (Figure 4.54) showing the distribution of the spectral index of the inertial range. A mean of -1.66 was found with a standard deviation of 0.06. A fit was also done, and there is evidence of a Gaussian distribution. This was then compared with the inertial range spectral index reported by *Smith et al.* [2006a], shown in Figure 4.55. The distribution to be compared with is that for open magnetic field lines. There is good agreement between the value -1.63 ± 0.14 reported by *Smith et al.* [2006a] for this case, and the value of -1.66 ± 0.06 found in this study. However, in this study, the value is somewhat closer to the Kolmogorov $-5/3$ and the range over which the values are distributed is much smaller than in *Smith et al.* [2006a].

4.10.3 Turnover Scale

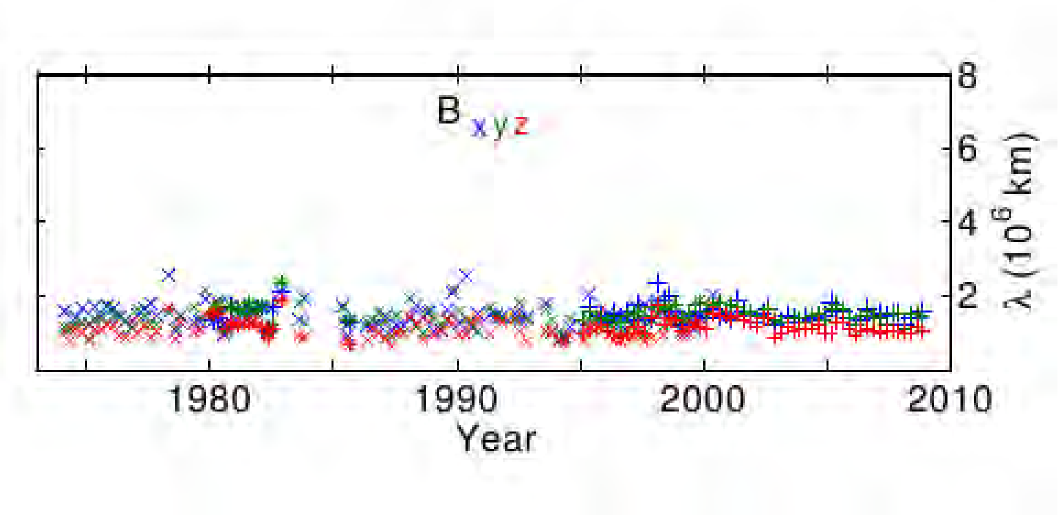

Figure 4.56: The quarterly averaged solar wind correlation length from 1974 to 2009. Figure adapted from *Wicks et al.* [2010].

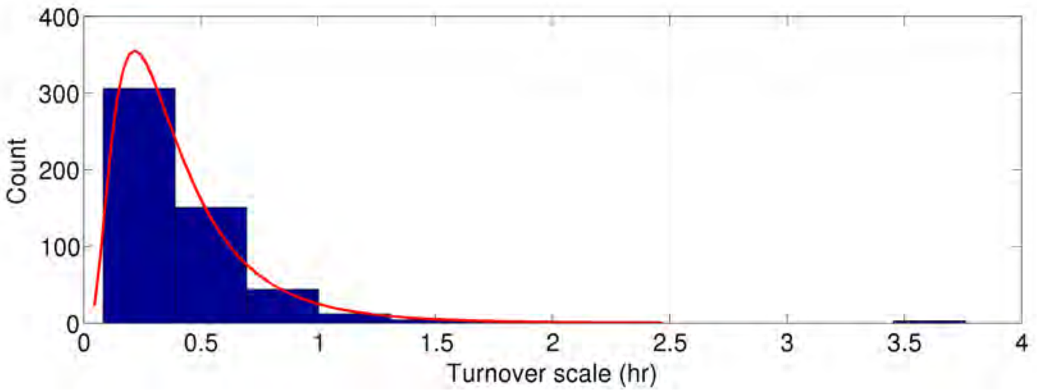

Figure 4.57: Turnover scale histogram with possible lognormal distribution (red line).

In Figure 4.56 the solar wind correlation length reported by *Wicks et al.* [2010] is shown for a period from 1974 to 2009. These authors report no significant periodicities, which is consistent with the finding in this study, as discussed in Section 4.5 and shown in Figure 4.38. The 27-day period dataset, which was shown in Figure 4.37, was used to construct a histogram shown in Figure 4.57. Here a possible log-normal distribution can be seen in agreement with the results of *Ruiz et al.* [2014] for the correlation scale, but in Section 3.8 it was shown that the method implemented in this study does not give good values for the turnover scale and may not be conclusive. Note that the correlation length used to compare with the turnover scale findings in this study is not exactly the same as the turnover scale, but the values are theoretically of the same order which makes them comparable.

4.10.4 Level of spectrum at 14 hours

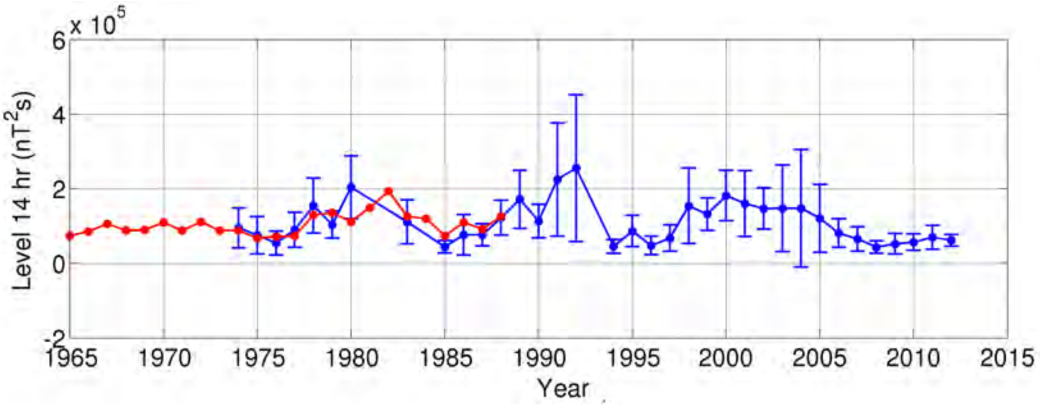

Figure 4.58: Level of spectrum at 14 hours from binned 27-day averages (blue line) compared with results reported by *Bieber et al.* [1993] (red line).

The level of the energy spectrum at 14 hours was calculated from 1973 to 2012 from 27-day period datasets, which were then binned to a year. This was then compared with the level of the energy spectrum at 14 hours calculated by *Bieber et al.* [1993] from 1965 - 1988, discussed in Section 2.11 and shown in Figure 2.19. Both datasets are shown in Figure 4.58, with blue points with error bars representing the findings of this study, and the red line indicating the values reported by *Bieber et al.* [1993]. *Bieber et al.* [1993] use a two-sided spectrum, so that when comparisons are made with results calculated with a one-sided spectrum such as that used in this study, the values for the two-sided spectrum should be doubled. The reason for this is that the total variance for both spectra should be the same, which means that the level of the two-sided spectrum would only be half that of the one-sided spectrum at a given wavenumber. Figure 4.58 shows a good agreement between the results reported by *Bieber et al.* [1993] and those of this study.

4.10.5 Energy Range Spectral Index

As discussed in Section 4.7 and shown in Figure 4.44, 27-day period datasets were binned to a year for the energy range spectral index, and are shown again in Figure 4.59, along with the observations of this quantity reported by *Bieber et al.* [1993] (discussed in Section 2.10). The red line represents the findings of *Bieber et al.* [1993], and the blue line with error bars the results of this study. As with the 14 hour level findings, here too a reasonably good agreement can be seen.

4.10.6 Cutoff scale

In Figure 4.60 the histogram for the energy range spectral index is shown for the 27-day period dataset (see Figure 4.43). A Gaussian distribution fit was made and a mean of -1.07 ± 0.20 was

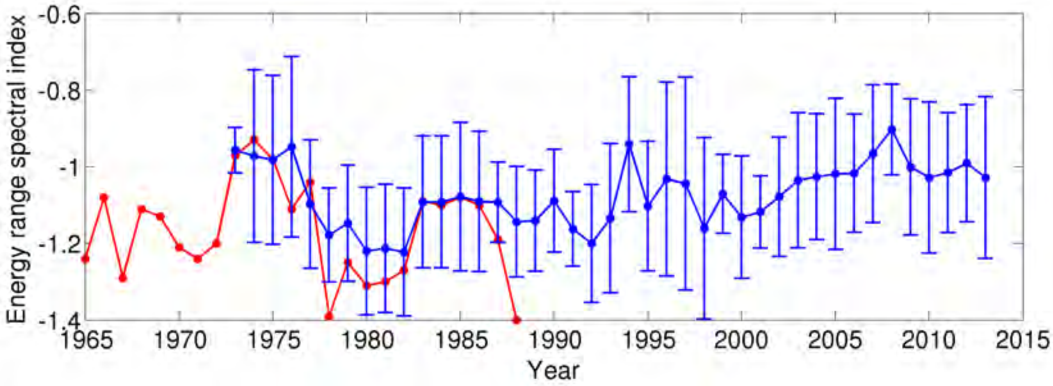

Figure 4.59: Energy range spectral index from this study (blue line) compared with results from *Bieber et al.* [1993] (red line).

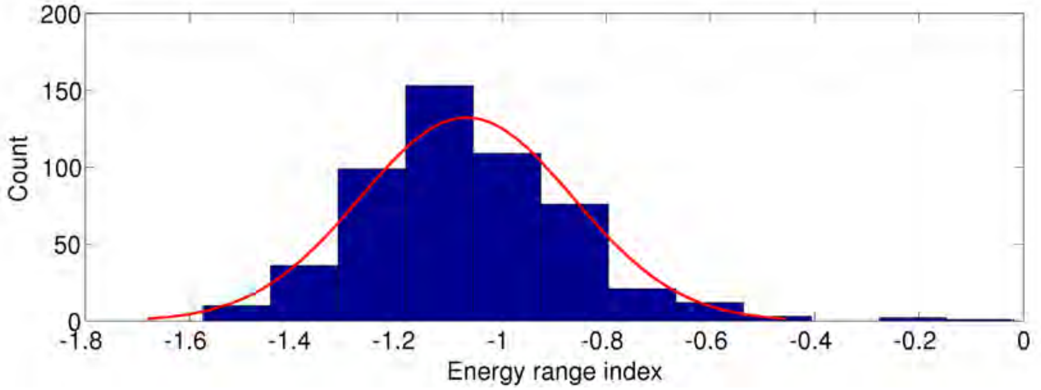

Figure 4.60: Energy range spectral index histogram with normal (Gaussian) distribution fit, Mean ± std. dev. = -1.07 ± 0.20.

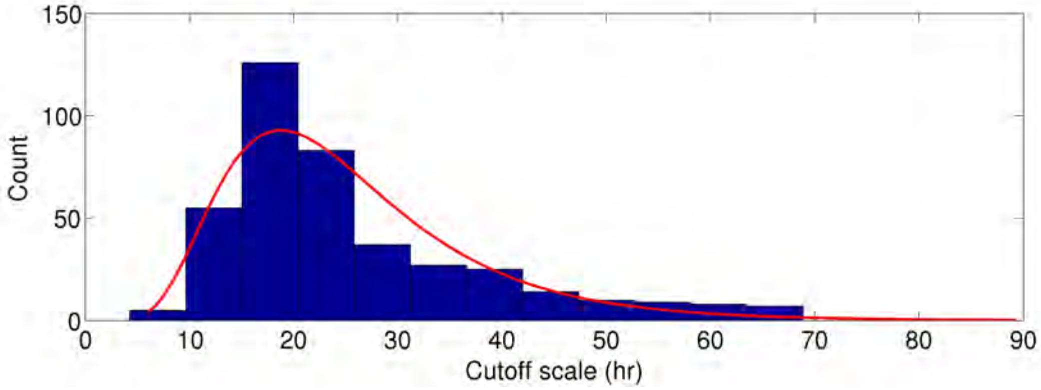

Figure 4.61: Cutoff scale histogram with lognormal distribution

found, which is in agreement with the value of -1.2 found by *Bieber et al.* [1993] for the period of 1965-1988. In Figure 4.61 the histogram is shown for the 27-day period dataset for the cutoff scale (see Figure 4.46) which was found to have no significant periodicity. Here a possible log-normal distribution can be fit, but this is inconclusive, as a Gaussian distribution could fit the observations equally well.

4.11 Summary

Various turbulence quantities spanning over several solar cycles were determined by analysing spacecraft data. To determine solar cycle dependence for these quantities, Lomb periodograms were constructed for the 27-day and yearly binned datasets of each.

The magnetic variance was found to have a clear solar-cycle dependence (11-year periodicity), which also correlated well with the HMF magnitude. An average value of 11nT^2 was found over the whole period for the magnetic variance, and 6.5 nT for the HMF magnitude. The ratio of the magnetic variance to the square of the magnetic field did not, however, show an 11-year periodicity, but ~8- and ~25-year periodicites. An average value of 0.52 was found for this value.

The inertial range spectral index showed no solar-cycle dependence, and an average value of -1.67 was found over the whole period. The same was true for the turnover scale: no solar-cycle dependence was seen, here an average value of 0.46 hours was found. Only with the 14-hour spectral level was a clear sign of solar cycle dependence seen again, with an average value of 1.1 × 105 nT^{2}s. The cutoff scale and outer range spectral index showed no signs of a solar-cycle dependence.

Comparisons were then made with observations published in the literature. The findings were favourable, with the magnetic variances agreeing well with results reported by *Smith et al.* [2006b] and *Bieber et al.* [1994]. The spectral level at 14 hours and the energy-range spectral index was compared with results reported by *Bieber et al.* [1993], and this too showed good agreement.

Chapter 5

Solar cycle dependent mean free paths and drift scales at earth

5.1 Introduction

Now that the behaviour of some basic turbulence quantities over several solar cycles has been studied, we can consider how diffusion and drift coefficients, which are functions of these quantities, will vary as function of solar cycle. In the following section, mean free paths and drift scales will be shown. These are related to diffusion and drift coefficients by $\kappa = (v/3)\lambda$, with v the particle velocity. Looking at the literature, it is clear that there are a variety of expressions for diffusion and for drift coefficients [*Shalchi*, 2009; *Burger and Visser*, 2010]. However, some are of such a form that it is not possible to determine how they depend on turbulence quantities, and obviously they must. The choice of coefficients made here is therefore not unique, but should give a fairly good idea of how the diffusion tensor would vary when the turbulence quantities that it depends on, change during the course of a solar cycle. In the previous chapter it was shown that the biggest change in turbulence quantities over a solar-activity cycle is in the variance. The factor of about three change from solar minimum to solar maximum overshadows the approximately 20% change seen in energy range spectral index. In what follows we will therefore concentrate on changes in the diffusion tensor due to the variance, and due to changes in the magnitude of the heliospheric magnetic field.

5.2 Elements of the diffusion tensor

Several theories exist that describe the parallel mean free path (*Teufel and Schlickeiser* [2003]; *Shalchi et al.* [2004b]), the perpendicular mean free path (*Shalchi* [2009]), and the turbulence-reduced drift coefficient (*Bieber and Matthaeus* [1997]; *Burger and Visser* [2010]; *Tautz and Shalchi* [2012]) [Private communication, NE Engelbrecht 2015]. For the purposes of this study, the proton parallel mean free path expression used by, e.g., *Burger et al.* [2008] and *Engelbrecht and Burger* [2013], which is based on quasilinear theory [see *Jokipii*, 1966] results derived by *Teufel* *and Schlickeiser* [2003] will be used. This expression is given by

$$\lambda_{\parallel} = \frac{3s}{\sqrt{\pi}(s-1)}\frac{R^2}{k_m}\left(\frac{B_o}{\delta B_{sl}}\right)^2\left[\frac{1}{4\sqrt{\pi}}+\frac{2R^{-s}}{\sqrt{\pi}(2-s)(4-s)}\right], \tag{5.1}$$

where $R = R_L k_m$ is a function of the maximal Larmor radius $R_L = R/B_o c$, k_m is the wavenumber corresponding to the slab turnover scale, δB_{sl}^2 the slab variance, B_o the magnitude of the HMF, and s the absolute value of the inertial range spectral index for the slab spectrum. For the perpendicular mean free path the approximate analytical expression derived by *Shalchi et al.* [2004a] from the nonlinear guiding center (NLGC) theory of *Matthaeus et al.* [2003] is used, given by

$$\lambda_{\perp} = \left[a^2\pi C(\nu)\lambda_{2D}\sqrt{3}\frac{\delta B_{2D}^2}{B_o^2}\right]^{2/3}\lambda_{\parallel}^{1/3}, \tag{5.2}$$

with $C(\nu) = (1/2\sqrt{\pi})[\Gamma(\nu)/\Gamma(\nu-1/2)]$, δB_{2D}^2 the 2D variance, λ_{2D} the 2D turnover scale, and ν half the absolute value of the spectral index in the inertial range of the 2D turbulence power spectrum. Note that the spectral index in the inertial range is not necessarily the same for the slab and for the 2D tubulence. The constant a is a numerical factor, chosen to be $1/\sqrt{3}$ *Matthaeus et al.* [2003].

Both of the above expressions have the advantages of yielding results in reasonably good agreement with observations and numerical simulations of the parallel and perpendicular mean free paths (see, e.g., *Bieber et al.* [1994], *Minnie et al.* [2007a], and *Shalchi* [2009]). However, Equation 5.2 is derived assuming a 2D spectrum that has an energy-containing range that remains at a constant level as function of wavenumber. The results of this study, as well as those of others (e.g. *Bieber et al.* [1993]), make this assumption questionable. Expressions have been derived for $\lambda_{\perp}$ which take into account more realistic energy-range wavenumber dependences by, e.g., *Shalchi et al.* [2010] and *Engelbrecht and Burger* [2015], but tend to be complicated, non-linear functions that are not readily solved for the perpendicular mean free path. The advantages of relative simplicity and tractability then make Eq. 5.2 attractive to this study. Perhaps more important is that the change in the energy range in the course of a solar cycle is only around twenty percent, as was pointed out in the introduction. We may therefore get the absolute magnitude of $\lambda_{\perp}$ slightly wrong, but still get a reasonable idea of relative changes during a solar activity cycle.

The effect of turbulence on the heliospheric drift coefficient is still not well understood (see, e.g., *Minnie et al.* [2007b] and *Engelbrecht and Burger* [2015]). The present study consider the turbulence-reduced drift coefficient proposed by *Tautz and Shalchi* [2012]. These authors fit a parametric expression that is a function of the ratio of the total magnetic variance to B_o to the results of their numerical simulations of the drift coefficient in various turbulence scenarios. The length scale corresponding to this parametrised drift coefficient for composite turbulence with 15% slab contribution and 85% 2D contribution is

$$\lambda_A = R_L\frac{1}{1+a(\delta B/B_o)^{2d}}, \tag{5.3}$$

where $a = 1.09 \pm 0.52$ and $d = 0.81 \pm 0.35$. This expression, like Eq. 5.2, has the advantage of being relatively simple. It is not clear whether this expression is a better description of the turbulence-reduced drift coefficient than the forms proposed by *Bieber and Matthaeus* [1997] or *Burger and Visser* [2010], and its use here is only to show the potential solar cycle variations this quantity could have.

To determine the results that will be shown next, several assumptions are made about the turbulence quantities that enter into Equations 5.1, 5.2, and 5.3. In what follows, the solar-cycle dependent variance values described in Section 4.3, and shown in Figure 4.3, are assumed to be the total variance δB^2. Slab and 2D variances are calculated from this total variance assuming an 85:15 proportion, after the results of *Bieber et al.* [1996]. Lastly, Equations 5.1, 5.2, and 5.3 are also functions of the uniform background HMF magnitude, and in what follows the *IMP* and *ACE* values for this quantity reported in Section 4.3 will also be used in these expressions. The 2D turnover scale is assumed to be constant as function of solar cycle, following the results presented in Section 4.5, and is assumed to be equal to the correlation scale perpendicular to the HMF in the slow solar wind reported as 0.0074 ± 0.0007 AU by *Weygand et al.* [2011]. This assumption is made because of uncertainties about the value of this quantity as evaluated using the data analysis method described in this study (see Section 3.8). The slab turnover scale is assumed to be equal to 0.0187 ± 0.0053 AU at Earth, after the correlation length measured parallel to the HMF in the slow solar wind by *Weygand et al.* [2011]. The inertial range spectral indices for both slab and 2D spectra are assumed to have a constant value of $-5/3$. This is also motivated by the solar cycle independent behaviour of this quantity reported in Section 2.8.

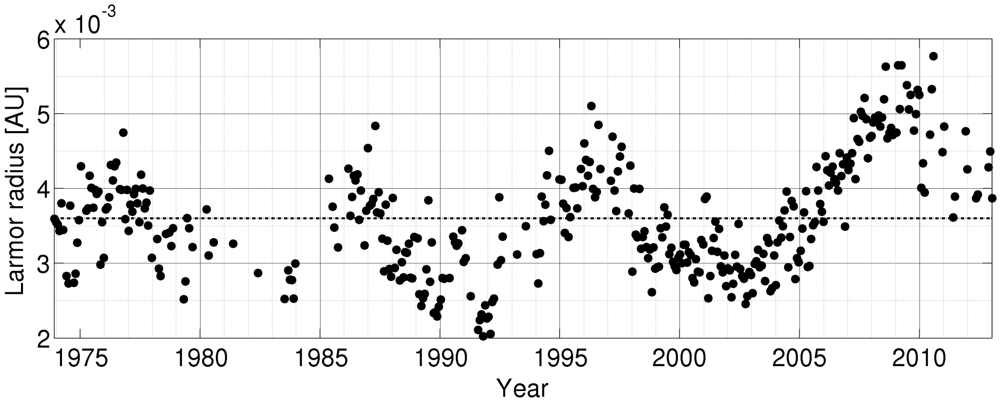

Figure 5.1: 27-day dataset for the Larmor radius of a 1 GV proton at Earth. The dashed line represents the average taken over all points, which is 0.0036 AU.

5.3 Time-dependent mean free paths and drift scale

In Figure 5.1 the 27-day period dataset for the calculated Larmor radius is shown from 1974 to 2013 (calculated at a rigidity of 1GV), with an average over the whole period of 0.0036 AU. A possible solar cycle dependency can be seen with four peaks visible, where the most recent

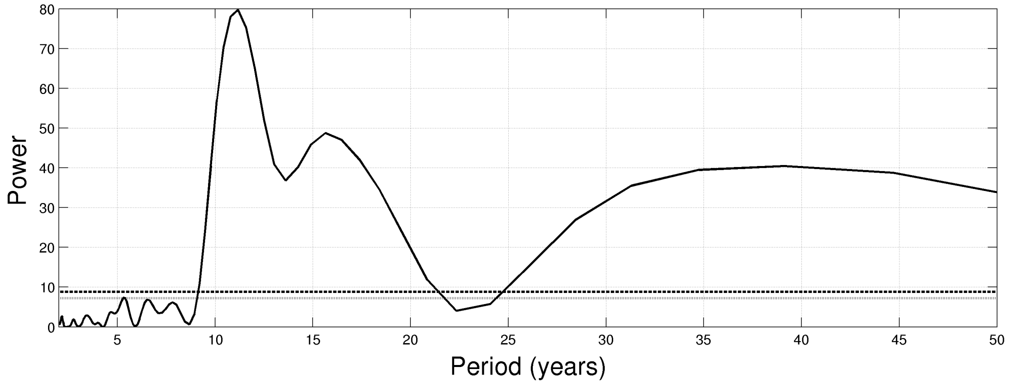

Figure 5.2: Lomb Periodogram for the 27-day period dataset for the 1 GV Larmor radius shown in Figure 5.1.

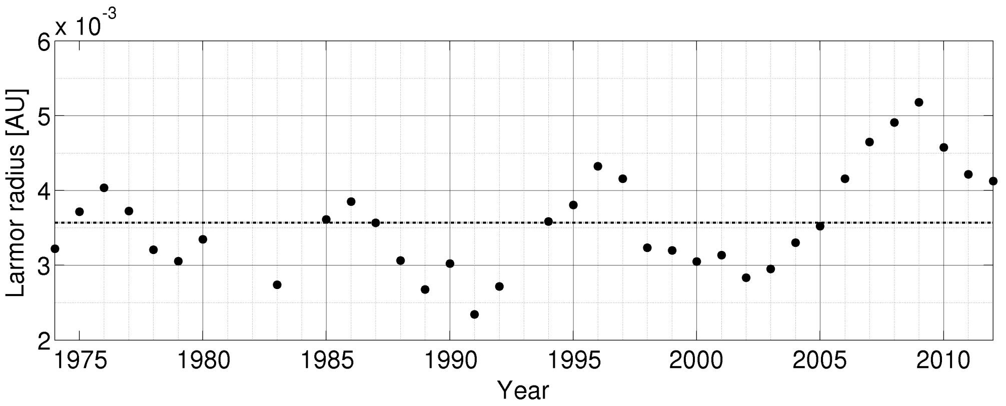

Figure 5.3: 1 GV Larmor radius calculated using 27-day data binned to a year. The dashed line represents the average taken over all points, which is 0.0036 AU.

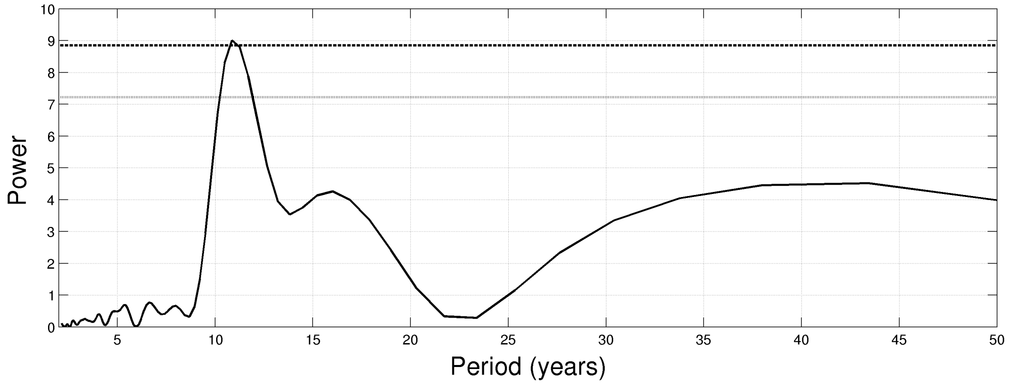

Figure 5.4: Lomb Periodogram for the yearly binned 27-day period datasets, for the 1 GV Larmor Radius.

peak is higher than the previous, reflecting the B_0^{-1} dependence of this quantitiy. From the Lomb periodogram shown in Figure 5.2 a clear solar-cycle dependence at an approximately 11 year period is present with a 100% significance. Next the yearly binned 27-day period datasets are shown in Figure 5.3, where an average of 0.0036 AU was found. Here too a possible solar cycle dependency is noted, and when looking at the Lomb Periodogram in Figure 5.4 one peak at ~11 years just slightly above the 99% significance level can be seen.

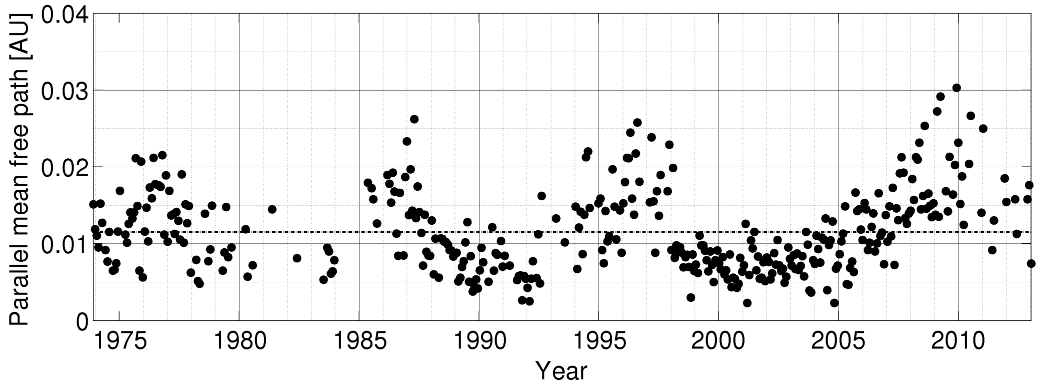

Figure 5.5: Parallel mean free path of 1 GV protons at Earth. The dashed line represents the average taken over all points, which is 0.0240 AU.

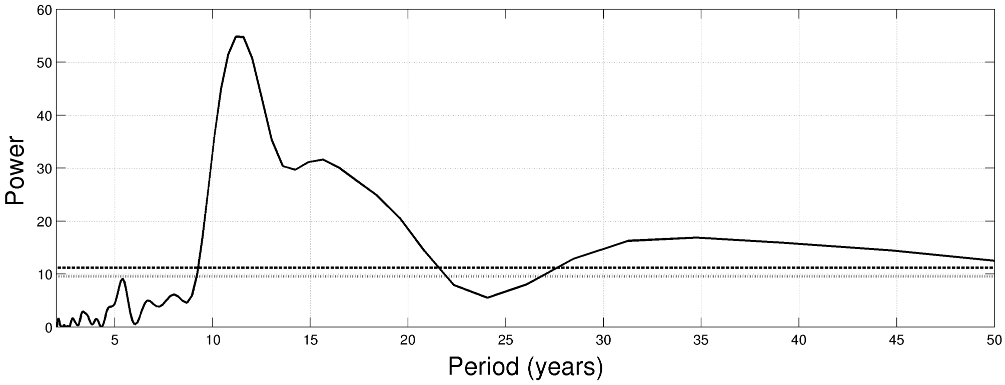

Figure 5.6: Lomb Periodogram for the 27-day period datasets, 1 GV parallel mean free path shown in Figure 5.5.

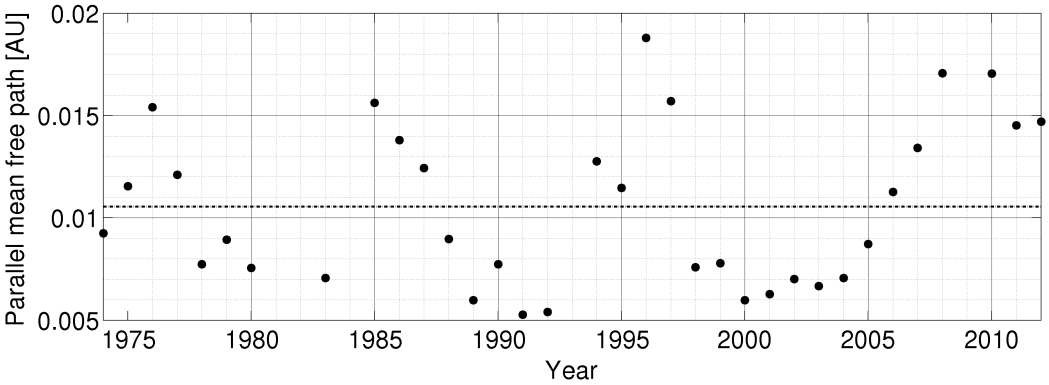

Figure 5.7: 1 GV parallel mean free path calculated using 27-data shown in Figure 5.5 binned to a year. The dashed line represents the average taken over all points, which is 0.019 AU.

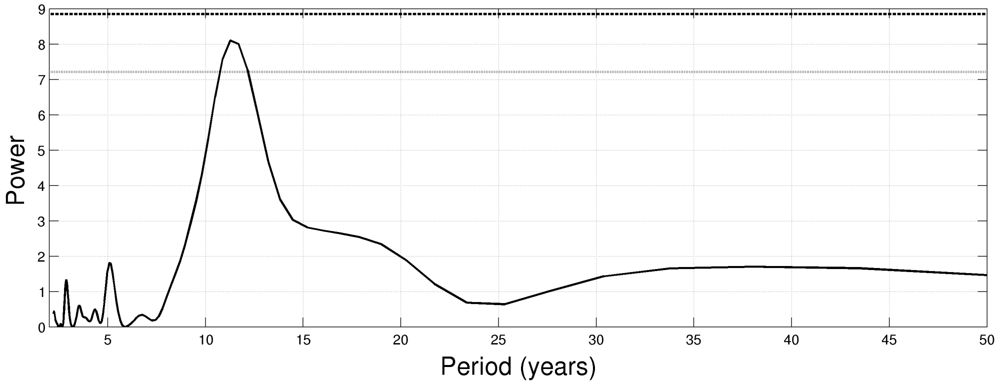

Figure 5.8: Lomb Periodogram for the parallel mean free path using yearly binned 27-day period datasets.

Figure 5.5 shows the parallel mean free path calculated from Equation 5.1 using the 27-day period dataset for the period 1974 to 2013, calculated at a rigidity of 1 GV. As with the Larmor radius, here too a possible solar cycle dependency can be seen. The Lomb periodogram for this set is shown in Figure 5.6 and a peak occurs at 11.2 years with a significance level of 100%. By taking the 27-day period dataset and binning it to a year, Figure 5.7 was created, with an average of 0.0194 AU. Its Lomb periodogram is shown in Figure 5.8. Here the most significant peak at a level of 98% is at 11.3 years. The change in the magnitude of the parallel mean free path is approximately a factor of three increase from solar maximum to solar minimum.

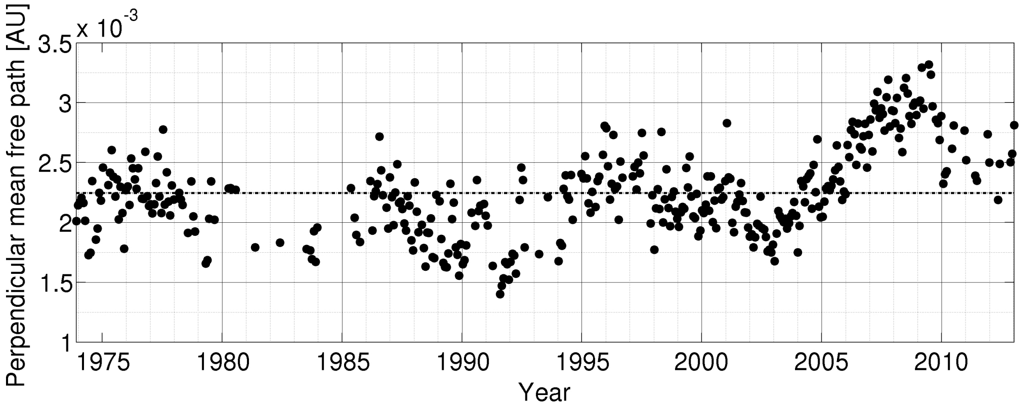

Figure 5.9: Perpendicular mean free path of 1 GV protons at Earth, calculated using 27-day period datasets. The dashed line represents the average taken over all points, which is 0.0018 AU.

The perpendicular mean free path, calculated using 27-day period dataset is shown in Figure 5.9, with an average over the whole period of 0.0018 AU. It shows a similar trend to that of the Larmor radius in Figure 5.1 where a possible solar cycle dependency can be seen, and where the last peak is slightly higher than the previous ones. This reflects the magnetic field dependence seen in Equation 5.2. A Lomb periodogram was constructed for this set, and is shown in Figure 5.10. Here a significant solar-cycle dependence above the 99% significance level is present, similar to the Larmor radius in Figure 5.2. Figure 5.11 shows the yearly averaged

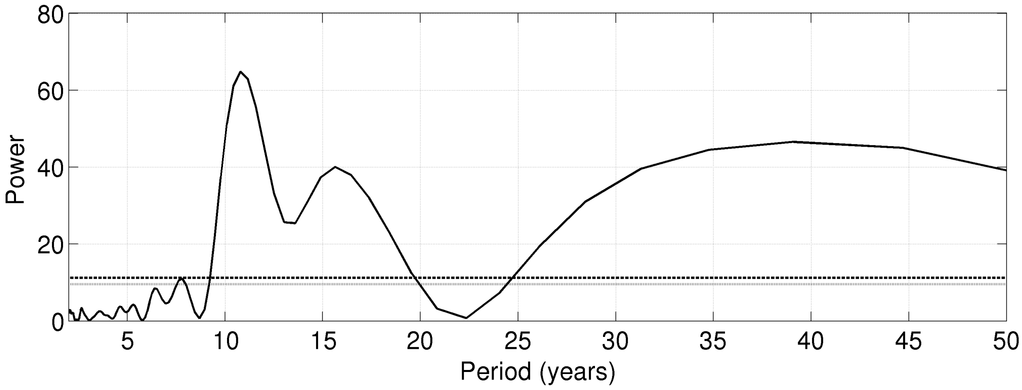

Figure 5.10: Lomb Periodogram for the 1 GV perpendicular mean free path shown in Figure 5.9, calculated using 27-day period datasets.

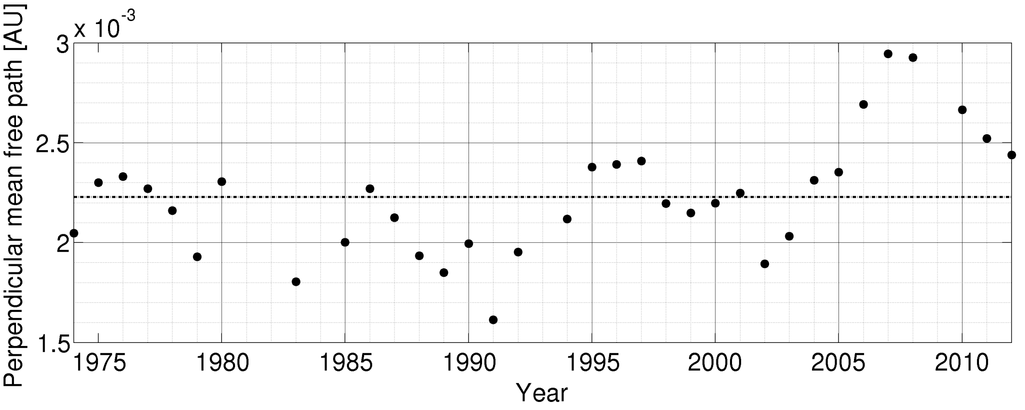

Figure 5.11: Perpendicular mean free path of 1 GV protons at Earth, calculated using 27-day data binned to a year. The dashed line represents the average taken over all points, which is 0.0020 AU.

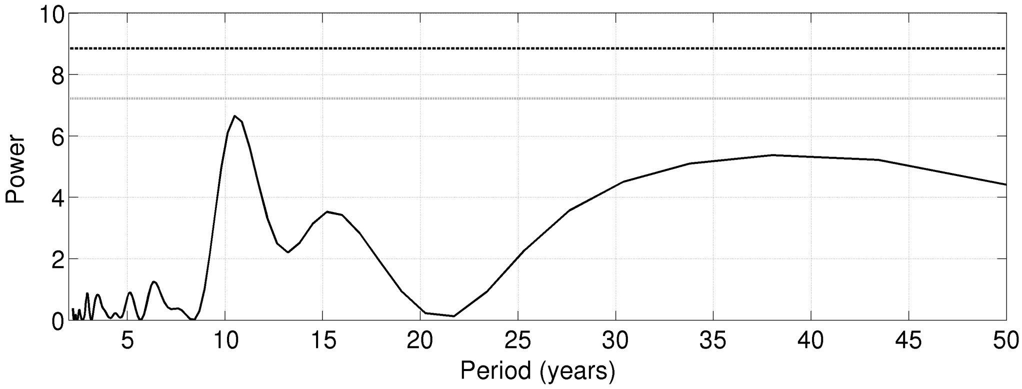

Figure 5.12: Lomb Periodogram for the yearly binned 27-day period datasets, for the 1 GV perpendicular mean free path.

27-day period dataset shown in Figure 5.9, where here too the peak around 2008 is slightly higher than the previous peaks. The average value of the perpendicular mean free path over the whole period is 0.0020 AU. Its Lomb periodogram is shown in Figure 5.12, where the most significant peak at a level of 70% occurs at 10.5 years. The change in magnitude is an ~ 30% increase from solar maximum to solar minimum conditions. The exception is during the period 2006 – 2010, where the increase relative to solar maximum conditions is around 60%. This unusual increase is not seen in the parallel mean free path (see Fig. 3.68).

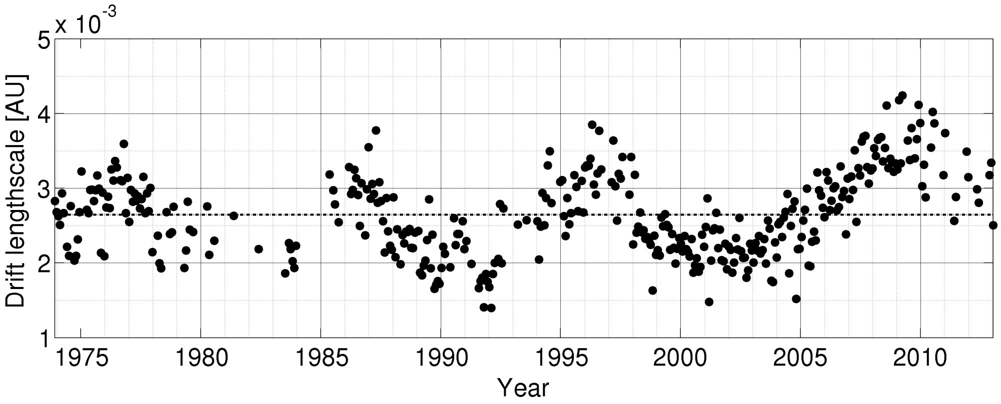

Figure 5.13: 27-day 1 GV drift lengthscale calculated from Equation 5.3. The dashed line represents the average taken over all points, which is 0.0026 AU.

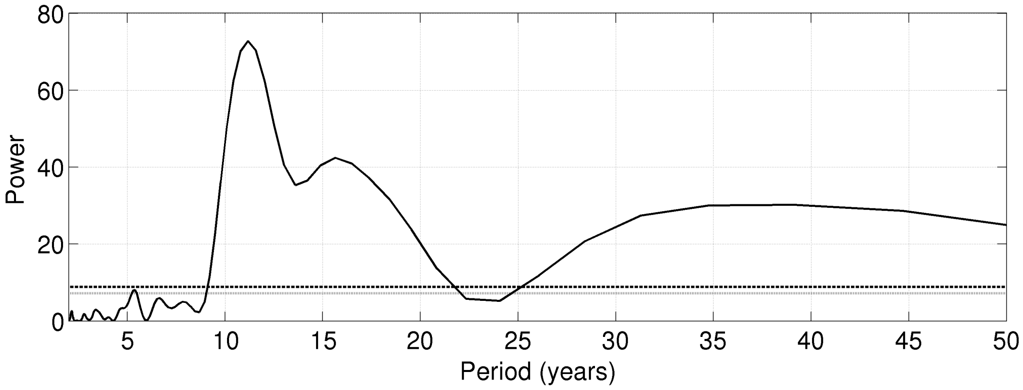

Figure 5.14: Lomb Periodogram for the 27-day period datasets, for the 1 GV drift lengthscale.

The last quantity calculated is the drift lengthscale for 1 GV protons at Earth. The drift lengthscale calculated using the 27-day period dataset is shown in Figure 5.13, with an average of 0.0026 AU. Its Lomb periodogram is shown in Figure 5.14 where a clear solar-cycle dependence at ~11 years is visible. This reflects the behaviour of $\delta B^2/B_0^2$, as expected from Equation 5.3. The yearly binned dataset is shown in Figure 5.15 where the solar minimum peak at ~2009 is higher than the previous peaks seen at ~1976, ~1986 and ~1996. Here an average of 0.0026 AU was found, the same as the 27-day period dataset. Its Lomb periodogram is shown in Figure 5.16 where the most significant periodicity is at ~11 years. The drift scale typically increases by about 50 % from solar maximum to solar minimum. Similar to the perpendicular mean free path, it is higher between 2006 and 2010 than during previous solar minima, with an increase from solar maximum to solar minimum of about 75%.

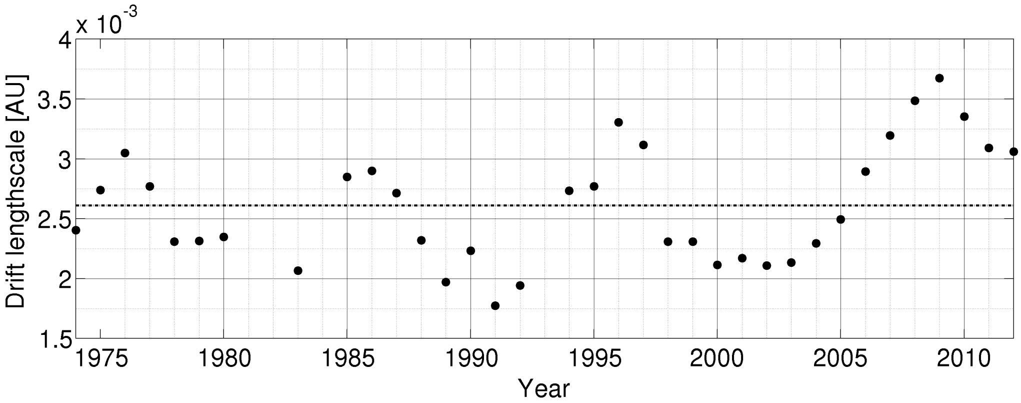

Figure 5.15: Drift lengthscale of 1 GV protons at Earth for 27-day data binned to a year. The dashed line represents the average taken over all points, which is 0.0026 AU.

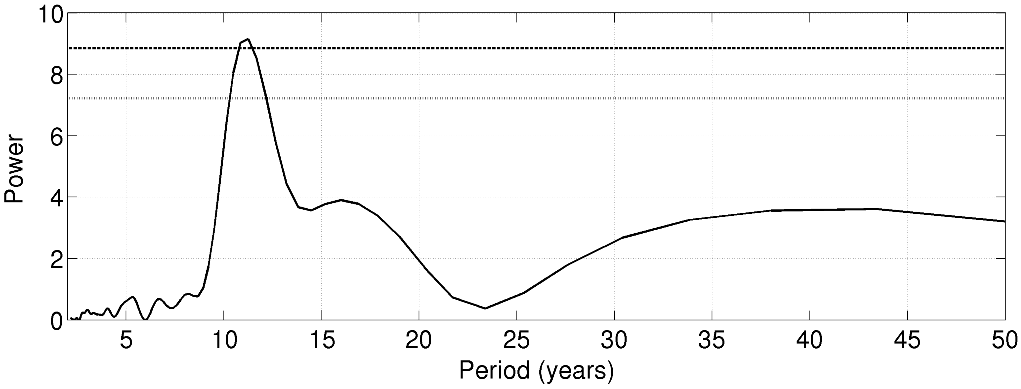

Figure 5.16: Lomb Periodogram for the yearly binned 27-day period 1 GV drift lengthscale shown in Figure 5.15.

5.4 Summary

Certain turbulence quantities were used as input for theoretical expressions for the parallel and perpendicular mean free paths, and the drift lengthscale. This was done to investigate possible solar-cycle dependence of the diffusion and drift coefficients. All three of these expressions showed clear 11-year periodicities, and showed larger values during solar minimum periods, and smaller values during solar maximum periods. The parallel mean free path showed an increase by a factor of three from solar maximum to minimum. The perpendicular mean free path increased typically by ~30% from solar maximum to solar minimum, while the drift scale typically showed a $\sim 50\%$ increase in solar maximum to solar minimum.

Chapter 6

Summary and Conclusions

This study presents an investigation into the solar-cycle dependence of basic turbulence quantities, which is indirectly used in modulation models. The turbulence quantities examined here are the inertial range spectral index, the turnover scale, the energy range spectral index, the cutoff scale, the outer range spectral index, and the total magnetic variance.

To determine this solar-cycle dependence, *ACE* and *IMP* data were analysed, as these datasets span several solar activity- and magnetic cycles. Variances were calculated from the N-component of the magnetic field data, which, assuming a Parker HMF, is expected to consist mostly of turbulent magnetic fluctuations. From these variances, second-order structure functions for data intervals of varying lengths over a period of 38 years were constructed. From theoretical and observational considerations, a spectral form was constructed and integrated, and from this fits to the observational second-order structure functions could be made. From these fits then information about basic turbulence quantities could be determined. This method was tested using simulated turbulence data with realistic omissions modelled after typical omissions in spacecraft datasets. The results yielded by this method were found to be credible for levels of data omissions less than 75%, and for the calculation of quantities related to the inertial range on the turbulence power spectrum and the total magnetic variance. Results relevant to the low wavenumber behaviour of the turbulence power spectrum, as well as the turnover scale where the inertial range of the power spectrum commences, were less accurate.

This analysis resulted in time series of turbulence quantities, which could then further be analysed using Lomb periodograms to confirm any potential periodicities. The variance was found to show a clear 11-year solar-cycle dependence with an average value of 11 nT^2. The solar-cycle dependence of the variance is well correlated with that of the HMF magnitude. This was also true for the 14-hour spectral level, which showed a clear solar-cycle dependence. Both the variance and spectral level assume larger values during solar maximum, and smaller values during solar minimum. No clear 11-year periodicity for the ratio of the variance to the square of the magnetic field magnitude could be seen, although there was evidence pointing to $\sim$8 and $\sim$25 year periodicities. An average value of 0.52 was found for this quantity. The turnover scale showed no sign of an 11-year periodicity, and neither did the inertial range spectral index, with an average value of -1.67. The energy-containing range showed a solar-cycle dependence, with an average value of -1.1. Results were inconclusive for the outer range spectral index and the cutoff scale. Comparisons of the results for the above mentioned turbulence quantities with observations published in the literature (where relevant) were favourable. Variances agreed well with results reported by *Smith et al.* [2006b] and *Bieber et al.* [1994] while the spectral level at 14 hours and the energy range spectral index compared well with results reported by *Bieber et al.* [1993]. Furthermore the inertial range spectral indices reported here compare favourably with those reported by *Smith et al.* [2006a]. When viewed as a whole, the turbulence quantities presented in this study lead one to conclude that it is only the level of the turbulence power spectrum that changes with solar cycle. This level is well correlated with the magnetic field.

To investigate possible solar-cycle dependence of the diffusion and drift coefficients, the results of the abovementioned analysis of the second-order strucutre function were used as inputs for theoretical expressions for these coefficients. Expressions for the parallel and perpendicular mean free paths, based on the quasilinear and nonlinear guiding center scattering theories and previously used in cosmic-ray modulation studies were used. For the turbulence-reduced drift coefficient, a parametised expression proposed by *Tautz and Shalchi* [2012] was used. Magnetic variances and magnetic field magnitudes found in this study were used as inputs for these expressions. The parallel and perpendicular mean free paths, as well as the drift length scale calculated in this way all showed clear 11-year periodicities, and assumed larger values during solar minimum periods than during solar maxima. On average, the parallel mean free path was found to increase by a factor of three from solar maximum to solar minimum, while the perpendicular mean free path showed a approximately 30% increase from solar maximum to solar minimum. The drift scale showed a $\sim 50\%$ increase in solar maximum to solar minimum.

Interestingly, during the recent unusual solar minimum (2009), magnetic variances were at their lowest values when compared with results from previous years. This behaviour is similar to that of the magnetic field magnitude at that time. The behaviour of the drift lengthscale and mean free paths presented here reflects this, with unusually large values for these quantities being evident during this particular solar minimum. The perpendicular mean free path during this unusual solar minimum was 60% larger than typical solar maximum values and the drift scale was 75% larger than typical solar maximum values. This behaviour was not seen for the parallel mean free path during the recent solar minimum.

To conclude, the results presented in this study provide much needed insight, not only into the solar-cycle dependence and values of basic turbulence quantities, but also into the potential solar-cycle dependence of the heliospheric diffusion tensor. This information is essential to furthering our understanding of turbulence in the heliosphere and cosmic-ray modulation.

Suggestions for future research:

- Investigating the effects of time-dependent turbulence quantities on cosmic-ray intensities calculated using *ab initio* modulation models.

- Using the second-order structure function technique to analyse *Voyager* and *Ulysses* observations, so as to get an idea of the spatial behaviour of turbulence quantities.
- Using the second-order structure function technique to investigate the solar-cycle dependence of the turbulence anisotropy reported by *Bieber et al.* [1996].

Acknowledgements

The author wishes to express her gratitude toward the following:

- Prof. R.A. Burger and Dr. N.E. Engelbrecht for their support and expert guidance.
- Friends and family, especially to Neels Nel for his encouragement.
- Personnel at the school of physics, in particular Mrs Petro Sieberhagen, for administrative support.
- The National Research Foundation and the Unit for Space Research of the NWU Potchefstroom Campus for financial support, and for the use of their computer facilities.
- The South African National Space Agency for financial support.
- Mary Vorster, for checking the language and grammar.
- Dr. Natalia Papitashvili, for the use of OMNIWeb data.
- My parents, Nellis and Celeste, for their endless love and support.

Centre for Space Research, North-West University, Potchefstroom Campus, 2520, South Africa

Bibliography

Aly, J. J., and T. Amari, Structure and evolution of the solar coronal magnetic field, *Geophysical and Astrophysical Fluid Dynamics*, *10*, 3–4, 2007.

Balogh, A., The heliospheric magnetic field, *Space Science Reviews*, 2011.

Batchelor, G., *The theory of homogenous turbulence*, Cambridge University Press, 1970.

Bieber, J. W., and W. H. Matthaeus, Perpendicular diffusion and drift at intermediate cosmic-ray energies, *Astrophys. J.*, *485*(2), 655–659, 1997.

Bieber, J. W., J. Chen, W. H. Matthaeus, C. W. Smith, and M. A. Pomerantz, Long-term variations of interplanetary magnetic field spectra with implications for cosmic ray modulation, *J. Geophys. Res.*, *98*(A3), 3585–3603, 1993.

Bieber, J. W., W. H. Matthaeus, C. W. Smith, W. Wanner, M.-B. Kallenrode, and G. Wibberenz, Proton and electron mean free paths: The Palmer consensus revisited, *Astrophys. J.*, *420*(1), 294–306, 1994.

Bieber, J. W., W. Wanner, and W. H. Matthaeus, Dominant two-dimensional solar wind turbulence with implications for cosmic ray transport, *J. Geophys. Res.*, *101*(A2), 2511–2522, 1996.

Bieber, J. W., W. H. Matthaeus, A. Shalchi, and G. Qin, Nonlinear guiding center theory of perpendicular diffusion: General properties and comparison with observation, *Geophys. Res. Lett.*, *31*, 10,805–+, doi:10.1029/2004GL020007, 2004.

Bracewell, R., *The Fourier transform and its applications*, Boston: McGraw-Hill, 2000.

Breech, B. A., Topics in solar wind turbulence, Ph.D. thesis, University of Delaware, 2008.

Bruno, R., and V. Carbone, The solar wind as a turbulence laboratory, *Living Rev. Solar Phys.*, *2*, 2005.

Burger, R. A., Cosmic-ray modulation and the heliospheric magnetic field, *Adv. Space Res.*, *35*(1), 636–642, 2005.

Burger, R. A., and D. J. Visser, Reduction of Drift Effects due to Solar Wind Turbulence, *Astrophys. J.*, *725*, 1366–1372, 2010.

Burger, R. A., T. P. J. Krüger, M. Hitge, and N. E. Engelbrecht, A Fisk-Parker hybrid heliospheric magnetic field with a solar cycle dependance, *Astrophys. J.*, *674*, 511–519, 2008.

Choudhuri, A. R., *The physics of fluids and plasmas*, 342–350 pp., Cambridge University Press, Cambridge, 1998.

Coleman, P. J., Jr., Turbulence, Viscosity, and Dissipation in the Solar-Wind Plasma, *Astrophys. J.*, *153*, 371, 1968.

Cranmer, S. R., Coronal holes, *Living Rev. Solar Phys.*, *6*, URL (cited on ¡date¿): http://www.livingreviews.org/lrsp–2009–3, 2009.

Davidson, P., *Turbulence: an introduction for scientists and engineers*, Oxford University Press, 2004.

Decker, R., The role of magnetic loops in particle acceleration at nearly perpendicular shocks, *J. Geophys. Res.*, *98*, 33–46, 1993.

Decker, R. B., and L. Vlahos, Numerical studies of particle acceleration at turbulent, oblique shocks with an application to prompt ion acceleration during solar flares, *The Astrophysical Journal*, *306*, 710–729, 1986.

Engelbrecht, N. E., On the heliospheric diffusion tensor and its effect on 26-day recurrent cosmic-ray variations, Master's thesis, North-West University (Potchefstroom Campus), 2008.

Engelbrecht, N. E., and R. A. Burger, Effects of various dissipation range onset models on the 26-day variations of low-energy galactic cosmic-ray electrons, *Adv. Space Res.*, *45*, 1015–1025, 2010.

Engelbrecht, N. E., and R. A. Burger, An ab initio model for the modulation of galactic cosmic-ray electrons, *The Astrophysical Journal*, *779*, 158, 2013.

Engelbrecht, N. E., and R. A. Burger, A comparison of turbulence-reduced drift coefficients of importance for the modulation of galactic cosmic-ray protons in the supersonic solar wind, *Advances in Space Research*, *55*, 390400, 2015.

Farris, M. H., and C. T. Russell, Determining the standoff distance of the bow shock: Mach number dependence and use of models, *J. Geophys. Res.*, *99*, 17,681–17,689, 1994.

Fisk, L. A., Motion of the footpoints of heliospheric magnetic field lines at the Sun: Implications for recurrent energetic particle events at high heliographic latitudes, *J. Geophys. Res.*, *101*, 15,547–15,553, 1996.

Forsyth, R. J., A. Balogh, E. J. Smith, G. Erdös, and D. J. McComas, The underlying Parker spiral structure in the Ulysses magnetic field observations, 1990-1994, *J. Geophys. Res.*, *101*(A1), 395–404, 1996.

Gnevyshev, M. N., Essential features of the 11-year solar cycle, *Solar*, *51*, 175–183, 1976.

Goldstein, M. L., and D. A. Roberts, Magnetohydrodynamic turbulence in the solar wind, *Physics of Plasmas*, *6*, 4154–4160, 1999.

Goldstein, M. L., D. A. Roberts, and W. H. Matthaeus, Magnetohydrodynamic Turbulence In The Solar Wind, *Annu. Rev. Astron. Astrophys.*, *33*, 283–326, doi:10.1146/annurev.aa.33.090195.001435, 1995.

Hale, G. E., On the probable existence of a magnetic field in sun-spots, *Astrophys. J.*, *28*, 315, 1908.

Hammer, O., D. A. Harper, and P. D. Ryan, Past: Paleontological statistics software package for education and data analysis, *Palaeontologica electronica*, *4*, 9, 2001.

Hathaway, D., The solar cycle, *Living Rev. Solar Phys.*, *7*, 2010.

Jokipii, J. R., Cosmic-ray propagation. I. Charged particles in a random magnetic field, *Astrophys. J.*, *146*(2), 480–487, 1966.

Kallenrode, M. B., *Space physics: an introduction to plasmas and particles in the heliosphere and magnetospheres*, Springer, 2001.

Klein, L. W., L. F. Burlaga, and N. F. Ness, Radial and latitudinal variations of the interplanetary magnetic field, *J. Geophys. Res.*, *92*, 9885–9892, 1987.

Kolmogorov, A., The Local Structure of Turbulence in Incompressible Viscous Fluid for Very Large Reynolds Numbers, *Akademiia Nauk SSSR Doklady*, *30*, 301–305, 1941.

Kraichnan, R. H., Inertial-Range Spectrum of Hydromagnetic Turbulence, *Physics of Fluids*, *8*, 1385–1387, 1965.

Krüger, T. P. J., The effect of a Fisk-Parker hybrid magnetic field on cosmic rays in the heliosphere, Master's thesis, North-West University, 2005.

Lang, K., *Sun, Earth and Sky*, Springer-Verlag, Germany, 1997.

Matthaeus, W., S. Oughton, X. H. Pontius Zhou, and X. Zhou, Evolution of energy-containing turbulent eddies in the solar wind, *Journal of Geophysical Research*, 1994.

Matthaeus, W. H., B. E. Goldstein, and J. H. King, An interplanetary magnetic field ensemble at 1 AU, *J. Geophys. Res.*, *91*, 59–69, 1986.

Matthaeus, W. H., P. C. Gray, D. H. Pontius Jr., and J. W. Bieber, Spatial structure and field-line diffusion in transverse magnetic turbulence, *Phys. Rev. Lett.*, *75*(11), 2136–2139, 1995.

Matthaeus, W. H., G. Qin, J. W. Bieber, and G. P. Zank, Nonlinear collisionless perpendicular diffusion of charged particles, *Astrophys. J. Lett.*, *590*(1), L53–L56, 2003.

Matthaeus, W. H., J. W. Bieber, D. Ruffolo, P. Chuychai, and J. Minnie, Spectral Properties and Length Scales of Two-dimensional Magnetic Field Models, *Astrophys. J.*, *667*, 956–962, doi:10.1086/520924, 2007.

Matthaeus, W. H., D. C. Montgomery, M. Wan, and S. Servidio, A review of relaxation and structure in some turbulent plasmas: magnetohydrodynamics and related models, *Journal of Turbulence*, *13*, 37, 2012.

Maunder, E. W., Spoerers law of zones, *Observatory*, *26*, 329330, 1903.

McComas, D. J., et al., Ulysses' return to the slow solar wind, *Geophys. Res. Lett.*, *25*, 1–4, 1998.

Meyer-Vernet, N., *Basics of the solar wind*, Cambridge University Press, 2007.

Miesch, M., Large-scale dynamics of the convection zone and tachocline, *Living Rev. Solar Phys.*, *2*, URL (cited on ¡23–02–2015¿): http://www.livingreviews.org/lrsp–2005, 1, 2005.

Minnie, J., J. W. Bieber, W. H. Matthaeus, and R. A. Burger, On the ability of different diffusion theories to account for directly simulated diffusion coefficients, *Astrophys. J.*, *663*, 1049–1054, doi:10.1086/518765, 2007a.

Minnie, J., J. W. Bieber, W. H. Matthaeus, and R. A. Burger, Suppression of Particle Drifts by Turbulence, *Astrophys. J.*, *670*, 1149–1158, 2007b.

Miranda, R. A., A. C. Chian, and E. L. Rempel, Universal scaling laws for fully-developed magnetic field turbulence near and far upstream of the earths bow shock, *Advances in Space Research*, *51*, 18931901, 2012.

Miroshnichenko, J. A., L. I. Perez-Peraza, Astrophysical aspects in the studies of solar cosmic rays, *International Journal of Modern Physics A*, *23*, 1–114, 2008.

Mitalas, K., R. Sills, On the photon diffusion time scale of the sun, *Astrophys. J*, *401*, 759, 1992.

Ni, R., and K. Xia, Kolmogorov constants for the second-order structure function and the energy spectrum, *Physical Review*, *87*, 2, 2013.

Nordlund, R. F. Stein, and M. Asplund, Solar surface convection, *Living Reviews in Solar Physics*, *6*, 2009.

Owens, M., The heliospheric magnetic field, *Living Rev. Solar Phys.*, *10*, 5, 2013.

Parker, E. N., Dynamics of the interplanetary gas and magnetic fields, *Astrophys. J.*, *128*, 664–676, 1958.

Parker, E. N., The passage of energetic charged particles through interplanetary space, *Planet. Space Sci.*, *13*, 9–49, 1965.

Podesta, J. J., D. A. Roberts, and M. L. Goldstein, Spectral exponents of kinetic and magnetic energy spectra, *The Astrophysical Journal*, *664*, 543–548, 2007.

Potgieter, M. S., Solar modulation of cosmic rays, *Living Rev. Solar Phys*, *10*, 3, 2013.

Press, W. H., S. A. Teukolsky, W. T. Vetterling, and B. P. Flannery, *Numerical Recipes*, Cambridge, 2007.

Ruiz, M. E., S. Dasso, W. H. Matthaeus, and J. M. Weygand, Characterization of the turbulent magnetic integral length in the solar wind: From 0.3 to 5 astronomical units, *Solar Physics*, *289*, 3917–3933, 2014.

Russell, C. T., Comments on the measurement of power spectra of the interplanetary magnetic field, *Solar Wind, NASA*, *308*, 365–374, 1972.

Scherer, K., and H. Fichtner, The return of the bow shock, *Astrophys. J.*, 2014.

Shalchi, A., *Nonlinear Cosmic Ray Diffusion Theories*, Springer, 2009.

Shalchi, A., J. W. Bieber, and W. H. Matthaeus, Analytic forms of the perpendicular diffusion coefficient in magnetostatic turbulence, *Astrophys. J.*, *604*, 675–686, doi:10.1086/382128, 2004a.

Shalchi, A., J. W. Bieber, W. H. Matthaeus, and G. Qin, Nonlinear parallel and perpendicular diffusion of charged cosmic rays in weak turbulence, *Astrophys. J.*, *616*, 617–629, doi:10.1086/424839, 2004b.

Shalchi, A., J. A. le Roux, G. M. Webb, and G. P. Zank, Nonlinear field line random walk for non-Gaussian statistics, *Journal of Physics A Mathematical General*, *42*, H5501, 2009.

Shalchi, A., G. Li, and G. P. Zank, Analytic forms of the perpendicular cosmic ray diffusion coefficient for an arbitrary turbulence spectrum and applications on transport of Galactic protons and acceleration at interplanetary shocks, *Astrophys. Space Sci.*, *325*, 99–111, 2010.

Sheeley, N. R., Y. M. Wang, and A. G. Nash, A new determination of the solar rotation rate, *The Astrophysical Journal*, *401*, 378–385, 1992.

Shue, J. H., J. K. Chao, H. C. Fu, C. T. Russel, P. Song, K. K. Khurana, and H. J. Singer, A new functional form to study the solar wind control of the magnetopause size and shape, *Journal of Geophysical Research (Space Physics)*, *102*, 94979511, 1997.

Simpson, J. A., D. Hamilton, G. Lentz, R. B. McKibben, A. Mogro-Campero, M. Perkins, K. R. Pyle, A. J. Tuzzolino, and J. J. O'Gallagher, Protons and Electrons in Jupiter's magnetic field: Results from the University of Chicago Experiment on Pioneer 10, *Science*, *183*, 306–309, 1974.

Smith, C. W., J. W. Bieber, and W. H. Matthaeus, Cosmic-ray pitch angle scattering in isotropic turbulence. II - Sensitive dependence on the dissipation range spectrum, *Astrophys. J.*, *363*, 283–291, 1990.

Smith, C. W., K. Hamilton, B. J. Vasquez, and R. J. Leamon, Dependence of the Dissipation Range Spectrum of Interplanetary Magnetic Fluctuationson the Rate of Energy Cascade, *Astrophys. J. Lett.*, *645*, L85–L88, doi:10.1086/506151, 2006a.

Smith, C. W., P. A. Isenberg, W. H. Matthaeus, and J. D. Richardson, Turbulent Heating of the Solar Wind by Newborn Interstellar Pickup Protons, *Astrophys. J.*, *638*, 508–517, 2006b.

Smith, E., The heliospheric current sheet, *J. Geophys. Res.*, *106*(A8), 15,819–15,832, 2001.

Snodgrass, H. B., Magnetic rotation of the solar photosphere, *Astrophys. J.*, *270*(1), 288–299, 1983.

Stone, E. C., A. M. Frandsen, R. A. Mewaldt, E. R. Christian, D. Margolies, J. F. Ormes, and F. Snow, The advanced composition explorer, *Space Science Reviews*, *86*, 1–22, 1998.

Strauss, R., Modeling of anomalous cosmic rays, Master's thesis, North-West University, Potchefstroom, 2010.

Tautz, R. C., and A. Shalchi, Drift Coefficients of Charged Particles in Turbulent Magnetic Fields, *Astrophys. J.*, *744*, 125, 2012.

Teufel, A., and R. Schlickeiser, Analytic calculation of the parallel mean free path of heliospheric cosmic rays. II. Dynamical magnetic slab turbulence and random sweeping slab turbulence with finite wave power at small wavenumbers, *Astron. Astrophys.*, *397*, 15–25, 2003.

Usoskin, I., A history of solar activity over millennia, *Living review solar physics*, *10*, 1, 2013.

Webb, D. F., and T. A. Howard, Coronal mass ejections: Observations, *Living Rev. Solar Phys*, *9*, 3, 2012.

Weygand, J. M., W. H. Matthaeus, D. S., and M. Kivelson, Correlation and Taylor scale variability in the interplanetary magnetic field fluctuations as a function of solar wind speed, *J. Geophys. Res.*, *116*, 2011.

Wicks, R. T., M. J. Owens, and T. S. Horbury, The variation of solar wind correlation lengths over three solar cycles, *Solar Physics*, *262*, 191–198, 2010.

Wood, B. E., Astrospheres and solar-like stellar winds, *Living Rev. Solar Phys*, *1*, 2004.

Zank, G., P. J. Heerikhuisen, B. E. Wood, N. V. Pogorelov, E. Zirnstein, and D. J. McComas, Heliospheric structure: the bow wave and the hydrogen wall, *The Astrophysical Journal*, *763*, 20, 2013.